SEARCH FOR LONG-LIVED PARTICLES WITH DISPLACED VERTICES USING THE CMS DETECTOR AT THE LHC

A Dissertation

Presented to the Faculty of the Graduate School

of Cornell University

in Partial Fulfillment of the Requirements for the Degree of

Doctor of Philosophy

by

Jennifer Yuenjane Chu

August 2018

© 2018 Jennifer Yuenjane Chu
ALL RIGHTS RESERVED

SEARCH FOR LONG-LIVED PARTICLES WITH DISPLACED VERTICES USING THE CMS DETECTOR AT THE LHC

Jennifer Yuenjane Chu, Ph.D.

Cornell University 2018

Results are reported from a search for long-lived particles in proton-proton collisions at $\sqrt{s} = 13\,\text{TeV}$ delivered by the CERN LHC and collected by the CMS experiment. The data sample, which was recorded during 2015 and 2016, corresponds to an integrated luminosity of $38.5\,\text{fb}^{-1}$. This search uses benchmark signal models in which long-lived particles are pair-produced and each decays into two or more quarks, leading to a signal with multiple jets and two displaced vertices composed of many tracks. No events with two well-separated high-track-multiplicity vertices are observed. Upper limits are placed on models of R-parity violating supersymmetry in which the long-lived particles are neutralinos or gluinos decaying solely into multijet final states or top squarks decaying solely into dijet final states. For neutralino, gluino, or top squark masses between 800 and 2600 GeV and mean proper decay lengths between 1 and 40 mm, the analysis excludes cross sections above 0.3 fb at 95% confidence level. Gluino and top squark masses are excluded below 2200 GeV and 1400 GeV, respectively, for mean proper decay lengths between 0.6 and 80 mm. A method is provided for extending the results to other models with pair-produced long-lived particles.

BIOGRAPHICAL SKETCH

Jennifer Chu graduated from Bay Shore High School in Bay Shore, NY in 2008. She was an undergraduate at Carnegie Mellon University in Pittsburgh, PA where she received a Bachelor of Science in Physics in 2012.

Jennifer is now a physics graduate student at Cornell University in Ithaca, NY. She conducts research with the Compact Muon Solenoid (CMS) experiment at the Large Hadron Collider (LHC) at the European Organization for Nuclear Research (CERN) in Geneva, Switzerland. Jennifer analyzes the data from the CMS detector to search for long-lived exotic particles. In 2015, she was based at CERN and worked on operations of the CMS pixel detector. Jennifer received a Master of Science in Physics in 2016, and expects to complete her Ph.D. in 2018.

ACKNOWLEDGEMENTS

This material is based upon work supported by the National Science Foundation Graduate Research Fellowship under Grant Nos. DGE-1144153 and DGE-1650441, and by the NSF-supported Cornell CMS projects "Particle Physics at the Energy Frontier" under Grant No. PHY-1307256 and "Particle Physics at CMS in the High Luminosity Era" under Grant No. PHY-1607126. Any opinion, findings, and conclusions or recommendations expressed in this material are those of the author and do not necessarily reflect the views of the National Science Foundation.

I would like to thank my advisor, Ritchie Patterson, for her many hours spent mentoring me both in one-on-one meetings and in group meetings several times per week for the past six years, despite being very busy as the director of the Cornell Laboratory for Accelerator-based Sciences and Education (CLASSE). Ritchie has taught me how to do research and trained me to become a scientist. I also very much appreciate her constant enthusiasm, which has made working with her a pleasure. Ritchie, thank you for choosing me to be your graduate student.

I would also like to thank my postdoc, Jordan Tucker, who has worked very closely with me on the analysis of the CMS data to search for long-lived particles. Jordan has helped me with all the details of computing at CMS, writing code, submitting jobs, making plots, working with CMS conveners, revising paper drafts, perfecting plots for publication, etc. Jordan is very skilled and knowledgeable, and I am fortunate to have learned from him as well as become good friends with him.

I would like to thank my committee: Ritchie Patterson, Peter Wittich, Yuval Grossman, and Maxim Perelstein.

Thank you to my fellow authors of the "RPV" analysis, in both Run 1 and Run 2: Jorge Chaves, Kevin McDermott, Ritchie Patterson, Dan Quach, Werner Sun, Jordan Tucker, Peter Wittich, and Margaret Zientek.

I have very much enjoyed being a part of the Cornell CMS group, and would like to thank my friends and colleagues: faculty Jim Alexander, Ritchie Patterson, Anders Ryd, Julia Thom-Levy, and Peter Wittich; postdocs Jordan Tucker, Louise Skinnari, Livia Soffi, Aurelijus Rinkevicius, and Yangyang Cheng; and fellow graduate students Nathan Mirman, Jorge Chaves, Susan Dittmer, Shao Min Tan, Kevin McDermott, Margaret Zientek, Zhengcheng Tao, Dan Quach, Andre Frankenthal, Abhisek Datta, Derek Cranshaw, and Shaun Hogan.

I would like to thank my parents, Amy and Joseph, whose unconditional love and support throughout my life have enabled me to pursue my Ph.D. in Physics. I would also like to thank my sisters, Josephine and Theresa, with whom I have had lots of fun times over the years.

Finally, I would like to thank my best grad school friends, Robin Bjorkquist and Jordan Moxon. Your friendship and support over the last six years have made graduate school a much better experience than it would have been otherwise, and I couldn't have finished it without you.

TABLE OF CONTENTS

LIST OF TABLES

LIST OF FIGURES

CHAPTER 1

INTRODUCTION

The Large Hadron Collider (LHC) at the European Organization for Nuclear Research (CERN) in Geneva, Switzerland collides protons together to study the interactions and properties of the fundamental particles. The unprecedented high energy and luminosity of the proton-proton (pp) collisions at the LHC allowed for the exciting discovery of a particle with properties consistent with those of the Higgs boson. The TeV-scale pp collisions also open the door for new physics, which could explain phenomena beyond the standard model (SM) such as dark matter. The primary goal of the experiments at the LHC is searching for new physics.

Supersymmetry (SUSY) [12, 13] is one of the proposed theories for physics beyond the SM that would explain some of the phenomena that we do not yet understand. For example, the lightest supersymmetric particle (LSP) could be a dark matter candidate, or SUSY could explain the mass of the Higgs boson. In the SM, the terms in the Feynman diagrams that are used to compute the mass of the Higgs boson diverge, but SUSY particles would cancel this effect and allow for a finite mass. In SUSY models, every SM particle has a supersymmetric partner with identical properties except for the mass and the spin. The SUSY particles are expected to be heavier than their SM partners, since they have not been observed at colliders with lower energies. The supersymmetric partners of SM fermions are bosons; the supersymmetric partners of SM bosons are fermions.

In spite of extensive efforts by the ATLAS and CMS Collaborations at the LHC, the superpartners of SM particles predicted by SUSY have not yet been observed. Figure 1.1 summarizes the results from searches for SUSY performed by the ATLAS and CMS Collaborations. Most of the searches for SUSY and other physics beyond the SM assume immediate, or "prompt", decays of the new

particles. However, in other regions of the parameter space for new physics models, the new particles could be long-lived. Searches for long-lived particles significantly expand the parameter space of physics beyond the SM probed by the experiments at the LHC.

Although a heavy particle will tend to decay promptly into lighter particles, the particle will be long-lived if all of the possible decay channels are suppressed. This could be due to a variety of reasons, including conservation laws, small phase space for the final state, small couplings of the decay vertex, and massive mediators. For examples of these effects, we consider particles in the SM. Table 1.1 lists a selection of particles in the SM in decreasing order of mean lifetime, along with the mass, and for a subset of these particles, the dominant decay modes and branching fractions. The photon is stable because it is massless, so due to conservation of momentum it cannot decay; the proton is known to have a very long lifetime because it is the lightest baryon; the electron has a very long lifetime because it is the lightest particle with its electromagnetic charge. Neutrons are long-lived because they decay to protons, electrons, and neutrinos, and the mass of the proton and the electron together is very close to the mass of the neutron, so the phase space for the final state is small. Muons are long-lived because they decay via the weak interaction, with the W boson as the mediator. The W boson is very massive as compared to the muon, which makes the decay of the muon less likely to occur.

Long-lived exotic particles can decay into a variety of final states, including quarks, leptons, photons, or particles that are invisible to detectors. Searches for long-lived particles are driven by the experimental signatures, which include displaced vertices, displaced jets, displaced leptons, displaced photons, heavy stable charged particles, disappearing tracks, and stopped particles. Figure 1.2 shows examples of possible final states of long-lived exotic particles and the resulting ex-

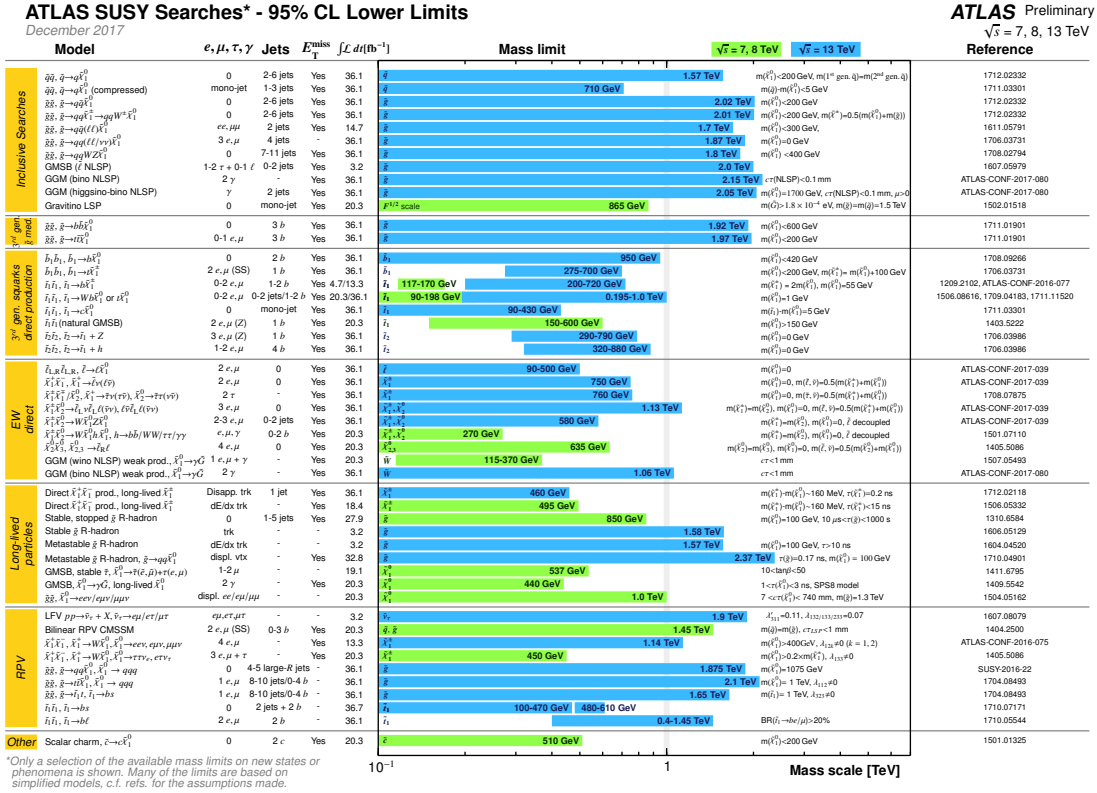

https://atlas.web.cern.ch/Atlas/GROUPS/PHYSICS/CombinedSummaryPlots/SUSY

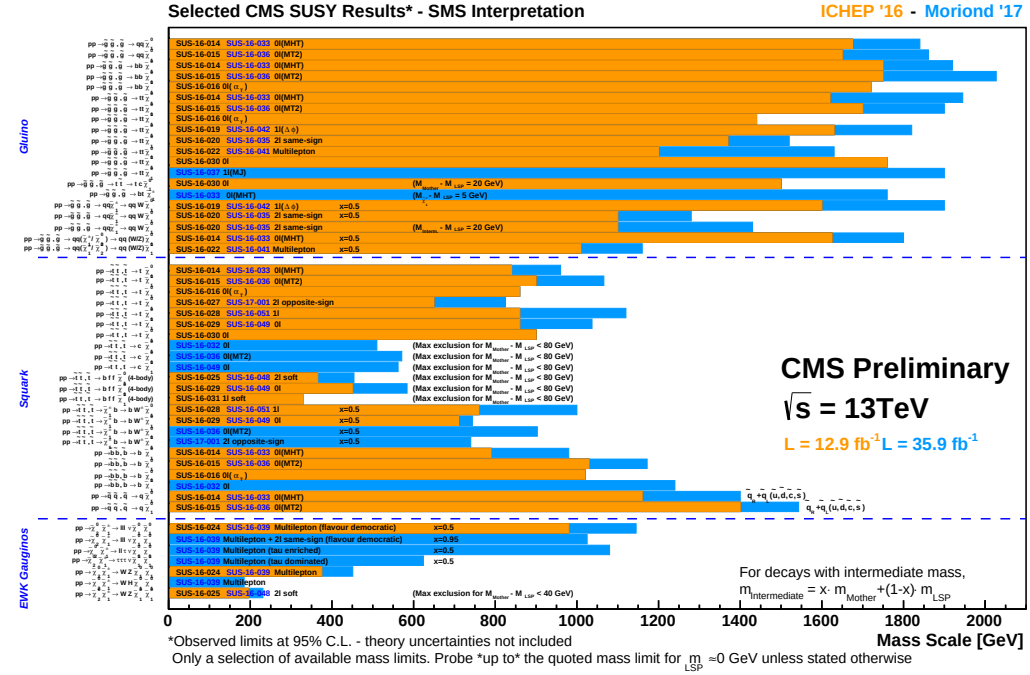

https://twiki.cern.ch/twiki/bin/view/CMSPublic/PhysicsResultsSUS

Figure 1.1: Summary of results from ATLAS and CMS searches for supersymmetry.

Table 1.1: A list of particles in the standard model in decreasing order of mean lifetime, along with the mass, and for a subset of the particles, the dominant decay modes and branching fractions [1].

Particle	Mean lifetime	Mass	Decay mode	Branching fraction
photon	stable	$m < 1 \times 10^{-18}\,\mathrm{GeV}$		
proton	$\tau > 2.1 \times 10^{29}\,\mathrm{yr}$	$m = 938.3\,\mathrm{MeV}$		
electron	$\tau > 6.6 \times 10^{28}\,\mathrm{yr}$	$m = 0.511\,\mathrm{MeV}$		
neutron	$c\tau = 2.6387 \times 10^{8}\,\mathrm{km}$	$m = 939.6\,\mathrm{MeV}$	$n \to pe^-\bar{\nu}_e$	100%
muon	$c\tau = 658.6384\,\mathrm{m}$	$m = 105.7\,\mathrm{MeV}$	$\mu^- \to e^-\bar{\nu}_e\nu_\mu$	≈100%
K_L^0	$c\tau = 15.34\,\mathrm{m}$	$m = 497.6\,\mathrm{MeV}$	$K_L^0 \to \pi^\pm e^\mp \nu_e$	40.55%
			$K_L^0 \to \pi^\pm \mu^\mp \nu_\mu$	27.04%
			$K_L^0 \to 3\pi^0$	19.52%
			$K_L^0 \to \pi^+\pi^-\pi^0$	12.54%
$\pi^\pm$	$c\tau = 7.8045\,\mathrm{m}$	$m = 139.6\,\mathrm{MeV}$	$\pi^+ \to \mu^+\nu_\mu$	99.98770%
$K^\pm$	$c\tau = 3.711\,\mathrm{m}$	$m = 493.7\,\mathrm{MeV}$	$K^+ \to \mu^+\nu_\mu$	63.56%
			$K^+ \to \pi^0 e^+ \nu_e$	5.07%
			$K^+ \to \pi^0 \mu^+ \nu_\mu$	3.352%
			$K^+ \to \pi^+\pi^0$	20.67%
			$K^+ \to \pi^+\pi^0\pi^0$	1.760%
			$K^+ \to \pi^+\pi^+\pi^-$	5.583%
K_S^0	$c\tau = 2.6844\,\mathrm{cm}$	$m = 497.6\,\mathrm{MeV}$	$K_S^0 \to \pi^0\pi^0$	30.69%
			$K_S^0 \to \pi^+\pi^-$	69.20%
$B^\pm$	$c\tau = 491.1\,\mu\mathrm{m}$	$m = 5279\,\mathrm{MeV}$		
B^0	$c\tau = 455.7\,\mu\mathrm{m}$	$m = 5280\,\mathrm{MeV}$		
B_s^0	$c\tau = 451.2\,\mu\mathrm{m}$	$m = 5367\,\mathrm{MeV}$		
$D^\pm$	$c\tau = 311.8\,\mu\mathrm{m}$	$m = 1870\,\mathrm{MeV}$		
$D_s^\pm$	$c\tau = 149.9\,\mu\mathrm{m}$	$m = 1968\,\mathrm{MeV}$		
D^0	$c\tau = 122.9\,\mu\mathrm{m}$	$m = 1865\,\mathrm{MeV}$		
tau	$c\tau = 87.03\,\mu\mathrm{m}$	$m = 1777\,\mathrm{MeV}$		
π^0	$c\tau = 25.5\,\mathrm{nm}$	$m = 135.0\,\mathrm{MeV}$	$\pi^0 \to 2\gamma$	98.823%
			$\pi^0 \to e^+e^-\gamma$	1.174%

perimental signatures. This dissertation focuses on a search for displaced vertices in a final state with many jets.

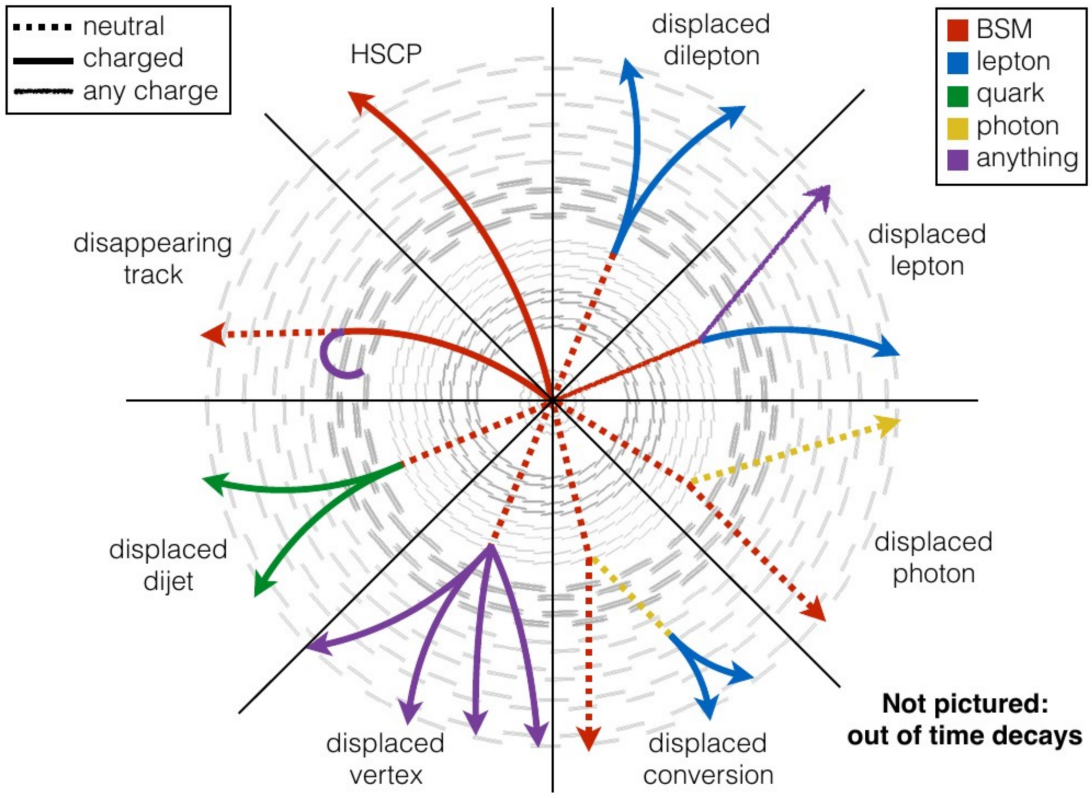

Figure 1.2: Examples of possible final states of long-lived exotic particles and the resulting experimental signatures. Figure credit: Jamie Antonelli.

Many theories for physics beyond the SM predict the pair production of long-lived particles decaying to final states with two or more jets. Some examples include R-parity violating supersymmetry [8], split supersymmetry [6], hidden valley models [7], and weakly interacting massive particle baryogenesis [14]. Figure 1.3 shows example diagrams for some of these models.

The analysis described in this dissertation is sensitive to models of new physics in which pairs of long-lived particles decay to final states with multiple charged particles. We present results for two benchmark signal models, as well as a method for applying the results more generally. The "multijet" benchmark signal is mo-

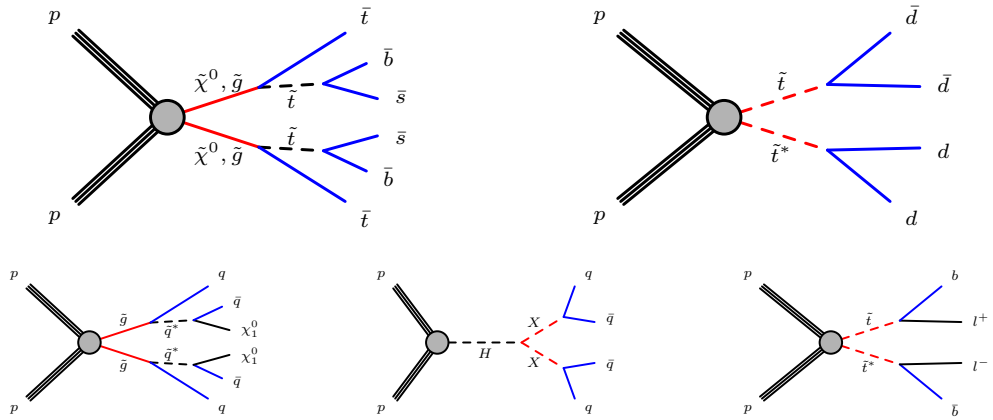

Figure 1.3: Example diagrams for some theoretical models with long-lived particles decaying to final states with jets: minimal flavor violating RPV SUSY [4] (upper left), standard or dynamical RPV SUSY [5] (upper right), split SUSY [6] (lower left), hidden valley models [7] (lower middle), and RPV SUSY [8] (lower right). The upper left diagram shows the "multijet" benchmark signal model, in which long-lived neutralinos ($\tilde{\chi}^0$) or gluinos ($\tilde{g}$) decay into top, bottom, and strange antiquarks, via a virtual top squark ($\tilde{t}$). The upper right diagram shows the "dijet" benchmark signal model, in which long-lived top squarks decay into two down antiquarks. The charge conjugate processes are also considered.

tivated by a minimal flavor violating model of RPV SUSY [4] in which the LSP is a neutralino or gluino, either of which is produced in pairs. The neutralino or gluino is long-lived and decays into a top antiquark and a virtual top squark, and the virtual top squark decays into strange and bottom antiquarks, resulting in a final state with many jets. The "dijet" benchmark signal corresponds to an RPV phenomenological model in which pair-produced long-lived top squarks each decay into two down antiquarks [5]. The diagrams for the multijet and dijet signal models are shown in the upper left and upper right of Fig. 1.3, respectively.

The experimental signature of long-lived exotic particle pairs is two displaced vertices, each consisting of multiple charged-particle trajectories intersecting at a single point. In the analysis presented in this dissertation, a custom vertex reconstruction algorithm identifies displaced vertices in the CMS detector. This algorithm differs from standard methods used to identify b quark jets [15], which

assume a single jet whose momentum is aligned with the vertex displacement from the primary vertex. Our custom algorithm is optimized for the decay of the LSP, which results in multiple jets emerging from a displaced vertex, often with wide opening angles. We focus on particles with intermediate lifetimes, corresponding to mean proper decay lengths $c\tau$ from 0.1 to 100 mm, by identifying vertices that are displaced from the beam axis but within the radius of the beam pipe. The signal is distinguished from the SM background based on the separation between the vertices: signal events have two well-separated vertices, while background events are dominated by events with only one displaced vertex, usually close to the beam axis.

My CMS analysis group at Cornell performed a similar search for displaced vertices in pp collisions at a center-of-mass energy of $\sqrt{s} = 8\,\text{TeV}$ in 2012 [16]. The analysis described in this dissertation is an updated version of that analysis, using pp collisions collected at $\sqrt{s} = 13\,\text{TeV}$, and is an improved version due to better background suppression along with a refined procedure for estimating the background and the associated systematic uncertainties. A similar analysis was performed by the ATLAS Collaboration [11]. The CMS and ATLAS Collaborations have also searched for displaced jets [17, 18, 19, 20], displaced leptons [21, 22], displaced photons [23], and displaced lepton jets [24]. The analysis reported here is sensitive to shorter lifetimes than those probed by previous analyses.

This focus of this dissertation is a search for long-lived particles, the details of which are described in Chapter 4. The theoretical motivation for R-parity violating supersymmetry, which is an example of a model for physics beyond the SM in which long-lived particles decay to multiple jets, is discussed in Chapter 2. Chapter 3 describes the LHC and the CMS detector. Chapter 5 describes related searches at the LHC. The results of the analysis are summarized in Chapter 6.

CHAPTER 2

R-PARITY VIOLATING SUPERSYMMETRY

This chapter focuses on the theoretical motivation for R-parity violating supersymmetry, which is an example of a model for physics beyond the SM in which long-lived particles decay to multiple jets.

2.1 R-parity in the minimal supersymmetric standard model

The minimal supersymmetric standard model (MSSM) [25] is the minimal phenomenologically viable extension of the SM. The superpotential, which determines the possible interactions, is given by

$$W = \mu H_u H_d + Y_e L H_d \bar{e} + Y_u Q H_u \bar{u} + Y_d Q H_d \bar{d} \tag{2.1}$$

where Q, $\bar{u}$, $\bar{d}$, L, and $\bar{e}$ are the matter fields, H_u and H_d are the Higgs fields, Y_u, Y_d, and Y_e are the Yukawa couplings, and the μ term is the supersymmetric version of the Higgs boson mass. The MSSM is "minimal" because the superpotential includes only the terms necessary to make the model phenomenologically viable, but does not include other terms that are gauge-invariant and renormalizable. The other terms that would be allowed in a more general superpotential are

$$W' = \lambda L L \bar{e} + \lambda' Q L \bar{d} + \lambda'' \bar{u} \bar{d} \bar{d} + \bar{\mu} L H_u \tag{2.2}$$

These terms are not in the MSSM because they violate conservation of baryon number (B) or lepton number (L): λ, λ', and $\bar{\mu}$ are the L-violating couplings, and λ'' is the B-violating coupling. In the SM, B and L are accidental symmetries because there are no possible renormalizable Lagrangian terms that violate them, but this is not true in the MSSM. However, a new symmetry can be imposed that eliminates the possibility of B and L violating terms in the superpotential, while

allowing the terms needed for the MSSM. This symmetry is called R-parity [26]. While B and L cannot be imposed separately, because they are known to be violated by non-perturbative electroweak effects, R-parity includes a combination of B and L and can in principle be an exact and fundamental symmetry. R-parity is defined as

$$R = (-1)^{3(B-L)+2S} \tag{2.3}$$

where S is the spin of the particle. With this definition of R-parity, all of the SM particles have even R-parity ($R = +1$), and all of the supersymmetric partners have odd R-parity ($R = -1$). The MSSM is defined to conserve R-parity.

2.2 R-parity conservation

If R-parity is conserved, then there can be no mixing between particles and supersymmetric particles, and every interaction vertex in the theory must contain an even number of supersymmetric particles. Here are some important phenomenological consequences:

- The lightest supersymmetric particle (LSP) must be stable. If the LSP is neutral and uncolored, then it interacts only weakly with ordinary matter and can be a dark matter candidate. If the LSP is charged or colored, then it could combine with other particles to form superheavy isotopes of hydrogen, but searches for heavy isotopes have placed stringent limits on charged or colored LSP candidates.
- All supersymmetric particles other than the LSP must eventually decay into a state that contains an odd number of LSPs. This is because supersymmetric particles have odd R-parity, and if R-parity is conserved the final state must also have odd R-parity.

- In collider experiments, supersymmetric particles can only be produced in even numbers. This is because SM particles have even R-parity, and if R-parity is conserved the final state must also have even R-parity.

These phenomenological consequences lead to distinct experimental signatures that can be used to distinguish between a SUSY signal and the SM background. If superpartners are produced and R-parity is conserved, the LSP passes through the detector unobserved, except for a potentially large amount of missing transverse energy. The decays of heavier supersymmetric particles to the LSP can produce many jets with high transverse momentum, resulting in higher total transverse jet energies than events from SM background processes. SUSY events can also have isolated leptons or photons in the final states. Many of the searches for R-parity conserving SUSY shown in Figure 1.1 search in specific final state topologies and design kinematic variables related to the missing transverse energy, jets, leptons, and photons to discriminate between signal and background.

The assumption of R-parity conservation is motivated by experimental observations such as limits on the proton lifetime [27]. However, physicists at the LHC have ruled out many SUSY models that conserve R-parity.

2.3 R-parity violation

The assumption of R-parity conservation is not strictly required as long as either lepton or baryon number is conserved, or the associated R-parity violating (RPV) [8] terms in the Lagrangian are extremely small.

Here are some phenomenological consequences of R-parity violation:

- The LSP may decay into exclusively SM particles. If its lifetime is sufficiently long, the LSP can be a dark matter candidate, as in the R-parity conserving

case. However, if the LSP is short-lived, it must be short-lived enough to not affect the predictions of the Big Bang nucleosynthesis.

- If B or L can be violated, there is a possible explanation for baryogenesis, which is the fact that there is no significant amount of antibaryons observed in the universe. This is because baryon-number violation is needed to generate a baryon-antibaryon asymmetry.
- If L is violated, neutrino masses and mixings are automatically generated. This is because the SM only has left-handed neutrino fields, so it needs additional particles to have nonzero neutrino masses and mixing, since the neutrino mass terms in the Lagrangian would need to involve two fields. R-parity violating couplings between neutrinos and supersymmetric particles would allow for the tree-level and loop contributions needed for the mixing.
- If B and L violations are simultaneously allowed, protons would decay with a very short lifetime. This is because R-parity violating couplings to supersymmetric particles would allow the three quarks in the proton to transition into two quarks and a lepton, so the proton would decay into a meson and a lepton or neutrino.
- A single supersymmetric particle can be produced from interactions of only SM particles.

If R-parity is violated, then the experimental signatures will include the decay products of the LSP via R-parity violating couplings. If L-violation dominates, the decay of the LSP produces additional leptons. If B-violation dominates, the decay of the LSP produces additional jets.

2.4 Minimal flavor violating RPV SUSY

The MSSM is made phenomenologically viable by two assumptions. One is the imposition of R-parity, which removes baryon and lepton number violating processes. The other is flavor universality, which suppresses the flavor-changing neutral currents that are induced when supersymmetry is broken to give masses to the superparticles. The single assumption of minimal flavor violation (MFV) can replace both of these assumptions. In MFV models of RPV SUSY [4, 28], the Yukawa couplings between superpartners and SM particles are the sole source of flavor symmetry violation, and the amplitudes for lepton- and baryon-number changing interactions are correspondingly small. The Yukawa couplings in the superpotential are taken to be superfields, similar to all of the other components in the superpotential, rather than just 3×3 matrices of numbers that describe the couplings of the quarks and leptons. The superpotential then has a flavor symmetry that is broken by only the Yukawa couplings, which are different for the different families. The smallness of the R-parity violating terms is then explained in terms of the smallness of the flavor parameters.

Without neutrino masses, there is no lepton number violation, so only the $\bar{u}\bar{d}\bar{d}$ term in the R-parity violating superpotential exists. The production processes of the superpartners are similar to those in the MSSM in that superpartners are produced in pairs, but the phenomenology depends on the identity of the LSP. The LSP can be a squark, a slepton, a neutralino, a chargino, or the gluino. If it is a squark, it will decay directly via the $\bar{u}\bar{d}\bar{d}$ vertex with prompt decays, but otherwise, there will be more final state particles and the lifetime will increase. If the LSP decays within the detector volume, there will be no large missing transverse energy. The long-lived particles can lead to signals with displaced vertices.

For the "multijet signals" used in the analysis described in this dissertation, the

LSP is assumed to be a neutralino or gluino, either of which is produced in pairs. The neutralino or gluino is sufficiently heavy to decay into a top antiquark and a virtual top squark, and the virtual top squark decays via a baryon-number violating process to strange and bottom antiquarks, as shown in Figure 2.1. Although this decay is heavily suppressed by the Yukawa coupling, it still dominates the top squark rate, with other partial widths being suppressed by a factor of 100 or more. As a consequence, the LSP is long-lived, with a lifetime that depends on the model parameters.

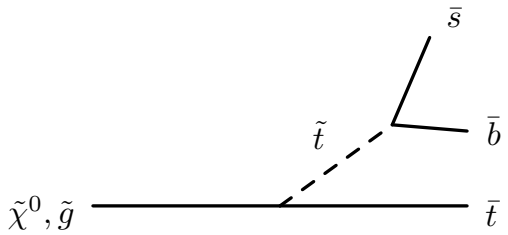

Figure 2.1: Decay diagram for the pair-produced neutralino ($\tilde{\chi}^0$) or gluino ($\tilde{g}$) LSP in the assumed signal model. In both cases, the LSP decays into a top antiquark plus a virtual top squark ($\tilde{t}$); the top squark then decays via a baryon-number violating process into strange and bottom antiquarks.

2.5 Previous exclusions

My CMS analysis group at Cornell searched for long-lived particles with displaced vertices in pp collisions at $\sqrt{s} = 8\,\text{TeV}$ [16], using as a benchmark the "multijet" signal model of MFV RPV SUSY described in the previous section. No excess yield above the expectation from SM processes was observed, and limits were placed on the pair production cross section as a function of mass and lifetime of the neutralino or gluino, as shown in Fig. 2.2. At 95% confidence level, the analysis excludes cross sections above approximately 1 fb for neutralinos or gluinos with mass between 400 and 1500 GeV and mean proper decay length between 1 and 30 mm. Gluino masses

are excluded below 1400 GeV for mean proper decay lengths in the range 2–30 mm.

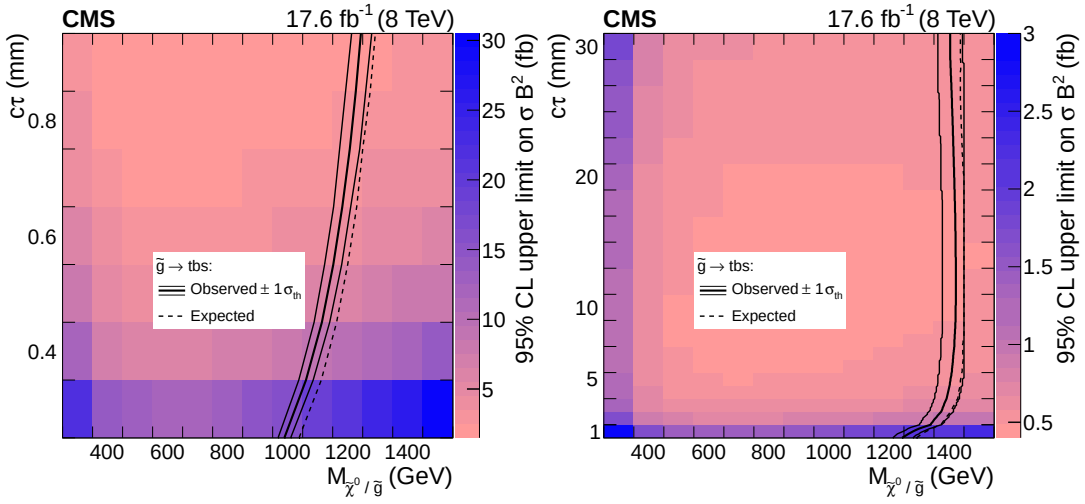

Figure 2.2: Observed 95% CL upper limits on cross section times branching fraction squared, with overlaid curves assuming gluino pair production cross section, for both observed (solid), with ±1 standard deviation theoretical uncertainties, and expected (dashed) limits. The search excludes masses to the left of the curve. The left plot spans $c\tau$ from 300 through 900 μm, while the right plot ranges from 1 to 30 mm.

In addition to the "multijet" signal model used in the 8 TeV analysis [16], the analysis described in this dissertation uses a "dijet" signal model in which pair-produced long-lived top squarks each decay into two down antiquarks. Figure 2.3 shows 95% CL exclusion curves for this signal model. These exclusion curves result from a recast of CMS and ATLAS searches for long-lived particles [5]. Top squark masses are excluded below 800 GeV for mean proper decay lengths above 1 mm.

Long-lived particles are an important prediction of these models of RPV SUSY as well as other models for physics beyond the SM. The high-energy pp collisions at the LHC can probe the existence of the massive particles predicted by new physics models. The precision of the measurements of charged-particle trajectories provided by the CMS detector allows for the reconstruction of displaced vertices produced by long-lived exotic particles. The next chapter describes the LHC and

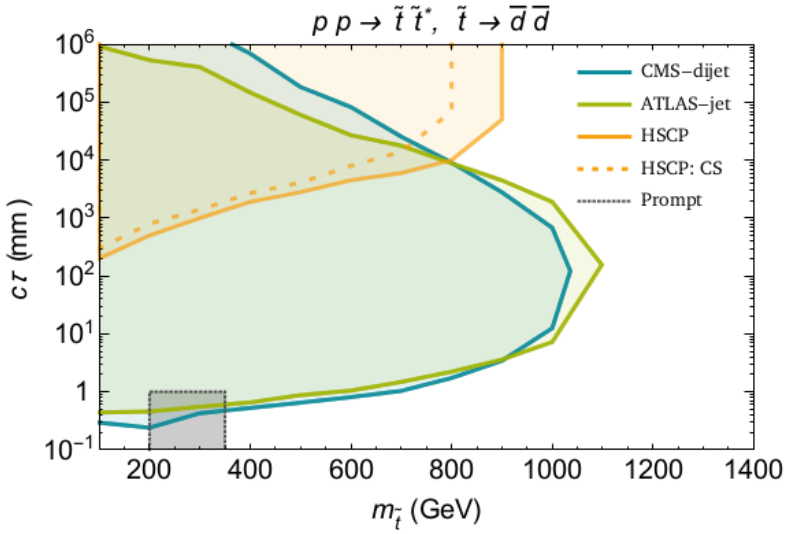

Figure 2.3: Prior 95% CL exclusion curves for a signal model in which pair-produced long-lived top squarks each decay into two down antiquarks. Figure taken from Ref. [5].

the CMS detector.

CHAPTER 3

THE LHC AND THE CMS DETECTOR

3.1 The Large Hadron Collider

The Large Hadron Collider (LHC) is the world's largest particle accelerator, with a circumference of approximately 27 km. The size of the accelerator, together with the high field strength of the superconducting magnets, enables particle beams to be accelerated to unprecedented high energies. It is located on the border between Switzerland and France, in a tunnel that is approximately 100 m underground. The LHC delivers proton-proton (pp) and heavy ion collisions to four experiments: ATLAS (Point 1), CMS (Point 5), ALICE (Point 2), and LHCb (Point 8). The "Points" refer to eight equidistant locations around the LHC ring, with Point 1 near the main CERN site in Meyrin, Switzerland, and the index increasing clockwise around the ring. During Run 1 of the LHC, the pp collisions were at center-of-mass energies of $\sqrt{s} = 7\,\text{TeV}$ in 2010 and 2011, and $\sqrt{s} = 8\,\text{TeV}$ in 2012. For Run 2 of the LHC, which is from 2015 to 2018, the pp collisions are at a center-of-mass energy of $\sqrt{s} = 13\,\text{TeV}$.

The proton beams are delivered in bunches of approximately 100 billion protons, with a bunch spacing of 25 ns. Each bunch crossing corresponds to a pp collision event.

3.2 The Compact Muon Solenoid detector

The Compact Muon Solenoid (CMS) [29] is a multipurpose detector designed to measure the results of pp collisions at the LHC. Figure 3.1 shows a diagram of the CMS detector. It consists of many layers optimized to measure different features of the particles. The innermost layer is the tracking detector, which is made of

pixels and strips that measure the trajectories of charged particles. The electromagnetic calorimeter surrounds the tracker and measures the energy of electrons and photons, while the hadron calorimeter measures the energy of hadrons. The muon chambers are used to identify muons. Neutrinos do not leave any energy in the detectors, so their signature is a momentum imbalance in the plane transverse to the beam, which is referred to as missing transverse energy.

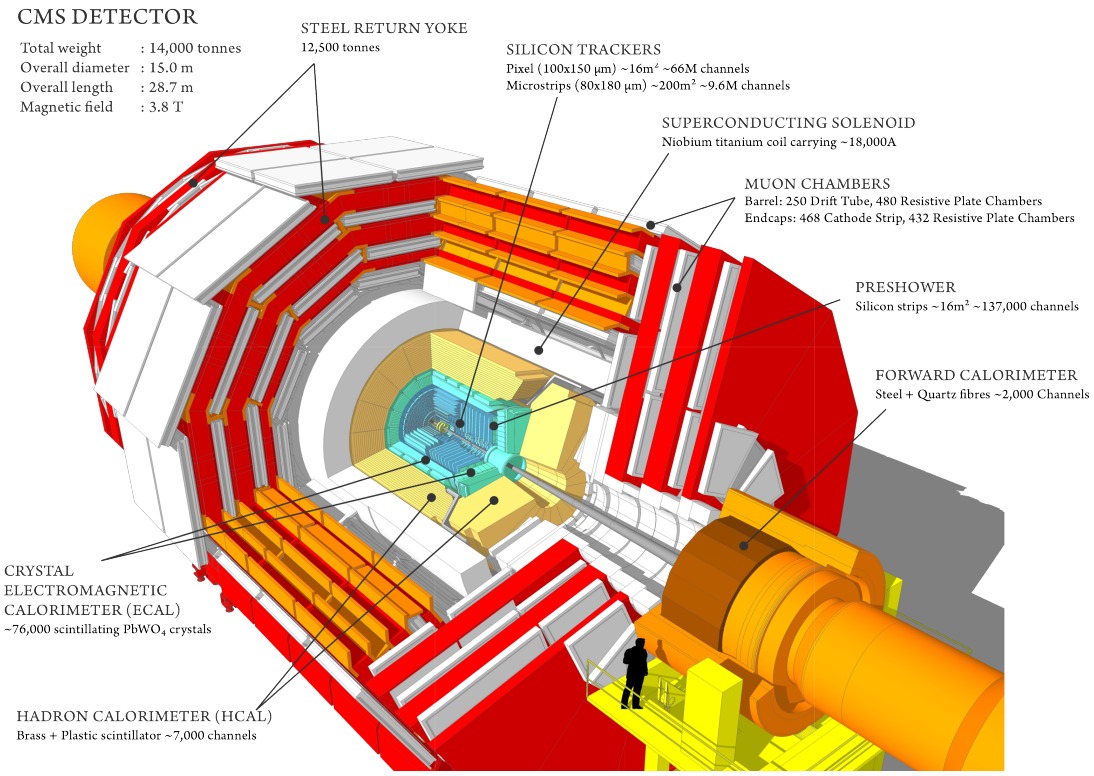

Figure 3.1: Diagram of the CMS detector.

CMS is located at LHC Point 5, which is near Cessy, France. The coordinate system has the origin at the center of the detector, with the x-axis pointing toward the center of the LHC, the y-axis pointing vertically upward, and the z-axis pointing along the beam direction that makes the coordinate system right-handed, which is toward the Jura mountains. The x-y plane is then transverse to the beam direction. The momentum in this transverse plane is denoted by p_{T}. The variable

used to characterize angles in the forward direction is pseudorapidity, denoted by η, which is defined as $\eta = -\ln(\tan(\theta/2))$ where θ is the polar angle measured from the z-axis. The azimuthal angle, denoted by ϕ, is measured from the x-axis in the x-y plane.

The central feature of the CMS detector is a superconducting solenoid providing a magnetic field of 3.8 T aligned with the proton beam direction. Contained within the field volume of the solenoid are the pixel and strip tracker, the electromagnetic calorimeter, and the hadron calorimeter. The muon tracking chambers are embedded in the steel flux-return yoke that surrounds the solenoid.

3.2.1 Pixel and strip tracker

The tracker, which is particularly relevant to the analysis described in this dissertation, measures the trajectories of charged particles in the range $|\eta| < 2.5$. The tracker is composed of silicon pixels and strips. Figure 3.2 shows a schematic drawing of the CMS tracker.

The pixel detector is composed of approximately 66 million pixels in three barrel layers and two forward disks. The barrel layers are located at mean radii of 4.4, 7.3, and 10.2 cm, and the forward disks are located at z positions of $\pm$34.5 and $\pm$46.5 cm. The dimensions of each pixel are 100 μm $\times$ 150 μm. When the CMS detector is taking data, a bias voltage is applied to the silicon pixel sensors such that when a charged particle passes through, electrons are collected, and the signal is the corresponding amount of charge. The pixel sensors are bump bonded to readout chips (ROCs) which each contain 52 columns $\times$ 80 rows = 4160 pixels. The ROCs are controlled by Token Bit Manager (TBM) chips, which each correspond to 8 or 16 ROCs in the barrel layers and 21 or 24 ROCs in the forward disks. The data from a TBM and its group of ROCs are sent over an optical link to a front

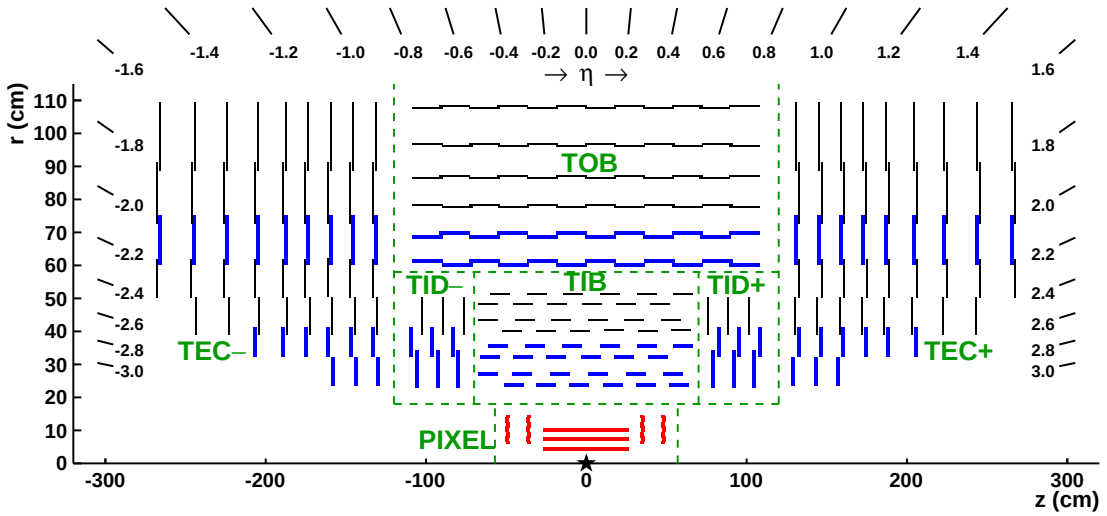

Figure 3.2: Schematic cross section through the CMS tracker; the tracker has cylindrical symmetry about $r = 0$. The red lines indicate modules of the pixel detector which provide 3D hits, the black lines indicate modules of the strip detector which provide 2D hits, and the blue lines indicate back-to-back modules of the strip detector which have one module rotated to allow the reconstruction of 3D hits. Figure taken from Ref. [9].

end driver (FED). The FEDs are located in the underground service cavern, with 40 total FEDs for the pixel detector (32 for the barrel pixels and 8 for the forward pixels). The Pixel Front End Controller configures the TBM and ROCs, and sends the clock and trigger signals through a fiber optic connection. The pixel detector is the most important part of the tracker for determining vertex positions.

The strip tracker is composed of approximately 9.6 million strips in ten barrel layers and twelve forward disks, which are separated into three subsystems: the Tracker Inner Barrel and Disks (TIB/TID), the Tracker Outer Barrel (TOB), and the Tracker EndCaps (TEC+ and TEC−). The TIB/TID has four barrel layers and three forward disks, extending to a radius of 55 cm. The TOB surrounds the TIB/TID and consists of six barrel layers, extending to a radius of 116 cm and z positions of ± 118 cm. TEC+ and TEC− are each composed of nine forward disks, extending to z positions of ± 282 cm.

3.2.2 Electromagnetic calorimeter

The electromagnetic calorimeter (ECAL) is composed of lead tungstate crystals, with 61200 crystals in the barrel and 7324 crystals in each of the two endcaps. When electrons or photons interact with the ECAL, the crystals scintillate. The scintillation light is measured by photodetectors, which are avalanche photodiodes in the barrel and vacuum phototriodes in the endcaps. The amount of light collected by the photodetectors is proportional to the energy of the electrons or photons.

3.2.3 Hadron calorimeter

The hadron calorimeter (HCAL) comprises the hadron barrel, hadron endcap, hadron outer, and hadron forward calorimeters. The HCAL is constructed out of brass absorber plates and plastic scintillator tiles. The scintillation light is converted by wavelength-shifting fibers and then measured by photodetectors, which are hybrid photodiodes. The amount of light gives a measure of the energy of the hadrons.

3.2.4 Muon chambers

The muon chambers are composed of four muon stations, each of which consists of drift tubes (DT), cathode strip chambers (CSC), and resistive plate chambers (RPC). The DTs are in the barrel region, the CSCs are in the endcap region, and the RPCs are in the barrel and in the endcap. The muon system identifies muons, measures the momentum of muons, and triggers on muons.

3.2.5 Trigger system

The bunch spacing of the proton beams at the LHC is 25 ns, corresponding to a pp collision event rate of 40 MHz. Due to the limited rate of the detector readout electronics and the limited amount of space for data storage, a trigger system is needed to select the most interesting events for data analysis.

At CMS, events of interest are selected using a two-tiered trigger system [30]. The first level (L1), which is composed of custom hardware processors, uses information from the calorimeters and muon detectors to select events at a rate of around 100 kHz within a time interval of less than 4 μs. The second level, known as the high-level trigger (HLT), consists of a farm of processors running a version of the full event reconstruction software optimized for fast processing, and further reduces the event rate to around 1 kHz before data storage.

3.3 Object reconstruction

This section describes how the information in the CMS detector is combined to reconstruct physics objects.

3.3.1 Tracks

At each bunch crossing, approximately 1000 charged particles emerge from the interaction region. The trajectories of charged particles, or "tracks", are reconstructed from measurements in the silicon pixel and strip trackers [9].

Hit reconstruction

Tracks are reconstructed from "hits" in the pixel and strip layers, which are reconstructed by clustering signals in the pixel and strip sensors, and then estimating

the cluster positions and their uncertainties. In the data acquisition, the signals are only read out if the charge in the corresponding pixel or strip channel is above a specified threshold (for the pixel detector, the threshold is approximately 3200 electrons for a single pixel; for the strip detector, the threshold is five times the expected channel noise for one strip, or two times the expected channel noise for each of two neighboring strips).

Pixel clusters are formed from adjacent pixels. The positions of the corresponding pixel hits are determined first using a fast algorithm, then using a more precise algorithm. The "first-pass" hit reconstruction algorithm projects the charge onto the transverse or longitudinal direction and uses the relative charge of the two pixels at each end of the resulting projected cluster. The second, slower "template-based" hit reconstruction algorithm compares the observed distribution of the cluster charge to expected projected distributions, or templates, generated from simulation, with different sets of templates for several ranges of the angle between the particle trajectory and the sensor. The true hit position in simulation is used to determine the bias and the uncertainty in the position of a reconstructed hit.

Strip clusters are seeded by channels with a charge at least three times the noise, with neighboring strips added if their charge is at least two times the noise, and clusters kept if the total charge is at least five times the noise. The positions of the corresponding strip hits are determined from the charge-weighted averages of the strip positions, and the uncertainty is usually parameterized as a function of the expected width of the cluster.

Track reconstruction

Tracks are reconstructed in a process known as "iterative tracking", which uses multiple iterations to produce a set of tracks corresponding to the pixel and strip

hits. The track reconstruction algorithm searches for the tracks that are easiest to find, removes the hits that are associated with those tracks, and then repeats. Each iteration consists of seed generation, track finding, track fitting, and track selection. These steps are described as follows:

- In the seed generation step, seeds are formed from pairs or triplets of hits in specified detector layers that satisfy requirements on the p_{T} and the transverse and longitudinal impact parameters.
- In the track finding step, the track parameters are estimated from the seed, and then hits from successive detector layers are added and the track parameters are updated. The hits are found by extrapolating the trajectory to determine which adjacent detector layers can be intersected, searching for compatible detector modules in those layers, checking which hits in those modules are compatible with the extrapolated trajectory, and updating the trajectory by adding one compatible hit from each group of modules. Only a limited number of candidates is kept at each layer. The search for hits is performed outwards, and then possibly also inwards depending on the track candidate. Track candidates with too many shared hits are removed, at each iteration and after all the iterations.
- In the track fitting step, the trajectory is refitted to optimize the values of the track parameters using the full track information, and outlier hits are removed.
- In the track selection step, more requirements are applied to reduce the rate of fake tracks, which are tracks that are not associated with charged particles.

There are six iterations in the iterative tracking, with the seed generation and track selection steps optimized to reconstruct prompt tracks with three pixel hits

(Iteration 0), prompt tracks with two pixel hits (Iteration 1), prompt tracks with low p_{T} (Iteration 2), and displaced or other tracks (Iterations 3–5).

Track resolution

For nonisolated particles with p_{T} of 1 to 10 GeV and $|\eta| < 1.4$, the track resolutions are typically 1.5% in p_{T}, 25–90 μm in the impact parameter in the transverse plane, and 45–150 μm in the impact parameter in the longitudinal direction [9].

3.3.2 Primary vertices

At each bunch crossing, there are approximately 20 pp collisions. Primary vertices, or pp interaction vertices, are reconstructed from tracks [9].

Primary vertex reconstruction

Tracks that are consistent with being produced in the pp interaction region are clustered based on the z positions of their points of closest approach to the beam spot. This is done using a deterministic annealing algorithm which simultaneously optimizes the number of vertices, the z positions of the vertices, and the assignment of tracks to vertices. The candidate vertices identified from this process are fitted using an adaptive vertex fitter to obtain the three-dimensional position and other parameters for each of the primary vertices.

Primary vertex resolution

In events with at least one reconstructed jet with $p_{\mathrm{T}} > 20$ GeV, the primary vertex resolution is approximately 10 μm in the x position and approximately 12 μm in the z position, for primary vertices with at least 50 tracks [9].

Primary vertex selection

Primary vertices are required to have at least four degrees of freedom in the fit, and z distance to the beam spot less than 24 cm. The reconstructed vertex with the largest value of summed physics-object p_{T}^2 is taken to be the primary pp interaction vertex, and the rest are considered to be from pileup interactions. The physics objects are the objects returned by a jet finding algorithm [31, 32] applied to all charged tracks associated with the vertex, plus the corresponding associated missing transverse momentum.

3.3.3 Beam spot

The beam spot represents a profile of where the LHC beams collide in the CMS detector [9]. The position and size of the beam spot are determined from an average over the events in each luminosity section, which correspond to the data collected every 23 seconds. The position of the beam spot is determined from the distribution of impact parameter in the transverse plane of the tracks in the events. The size of the beam spot is determined from the distribution of primary vertices in the events.

3.3.4 Particle-flow reconstruction

The particle-flow (PF) reconstruction algorithm [10] combines information from the CMS subdetectors to identify individual particles. The particles that can be observed in the CMS detector are muons, electrons, photons, charged hadrons, and neutral hadrons.

The interactions of each type of particle with the CMS detector are shown in Fig. 3.3. Muons produce tracks in the silicon tracker and in the muon cham-

bers. Electrons and photons produce clusters of energy in the ECAL, and are distinguished because electrons additionally produce tracks in the silicon tracker. Similarly, charged and neutral hadrons produce clusters of energy in the HCAL, with charged hadrons additionally producing tracks in the silicon tracker.

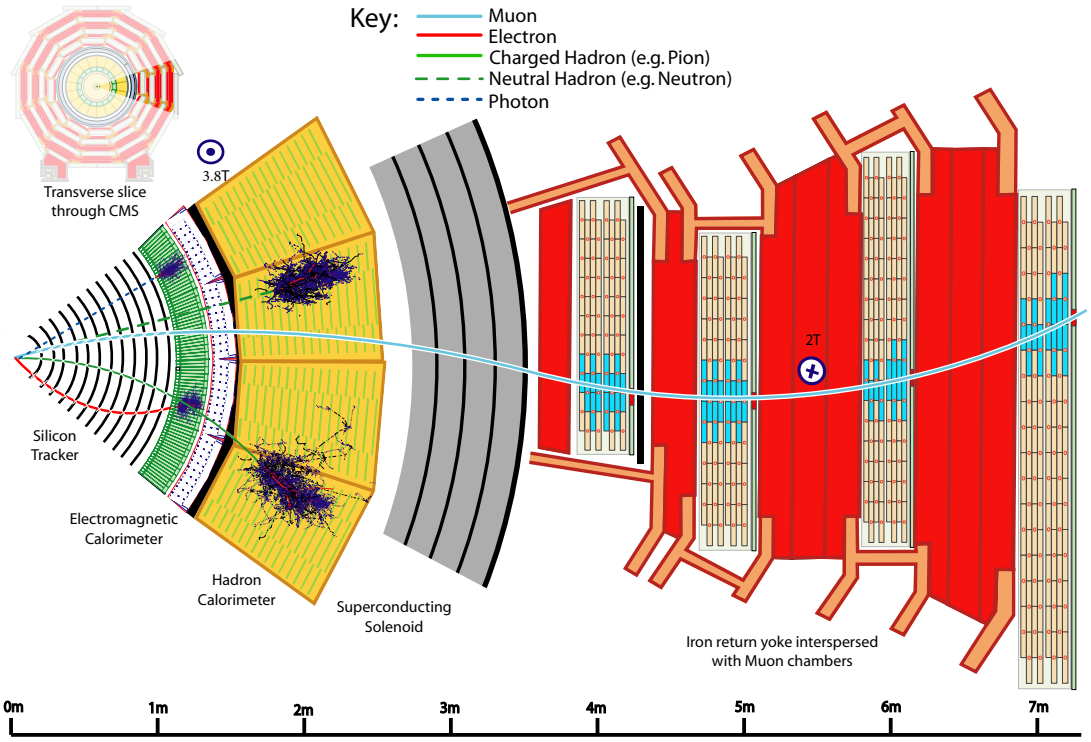

Figure 3.3: Interactions of the particles identified with the particle-flow reconstruction algorithm. Figure taken from Ref. [10].

Particle-flow elements

The particles are identified and reconstructed from PF elements, which include charged-particle tracks, electron tracks, muon tracks, and calorimeter clusters. The charged-particle tracks are reconstructed as described in Section 3.3.1. For electrons and muons, information from the electromagnetic calorimeter and the muon chambers is also used to reconstruct tracks.

Energetic and well-isolated electrons are seeded from ECAL clusters, and the energy and position of the ECAL clusters are used to infer the position of the hits expected in the innermost tracker layers. Electrons in jets, electrons with small p_{T}, and electrons from conversions in the tracker material are seeded from tracks reconstructed in the iterative tracking with $p_{\mathrm{T}} > 2\,\mathrm{GeV}$. Electron tracks are then reconstructed using seeds obtained from both the ECAL-based and the tracker-based electron seeding procedures.

There are three types of muons reconstructed using the CMS detector: standalone muons, global muons, and tracker muons. Standalone-muon tracks are reconstructed by clustering and fitting hits from the muon detectors. Global-muon tracks are reconstructed by matching standalone-muon tracks to inner tracks. Tracker-muon tracks are reconstructed by matching inner tracks to muon segments. Global muons and tracker muons that share the same inner track are then merged into a single candidate.

Calorimeter clusters are seeded by cells with an energy larger than a given seed threshold, and larger than the energy of the neighboring cells. Topological clusters are then formed from the seed cell by adding neighboring cells that have an energy larger than twice the noise level. An expectation-maximization algorithm based on a Gaussian-mixture model is used to reconstruct the clusters within a topological cluster. Calibration of the calorimeter clusters is necessary to distinguish charged particles from neutral particles. For the ECAL, the calibration is determined from simulated single photons; for the HCAL, the calibration is determined from simulated single neutral hadrons, specifically K_L^0.

Particle identification and reconstruction

PF elements from different subdetectors are connected using a link algorithm, which finds links and defines the distance between the two PF elements in the

link. Links from the tracker to the calorimeter are found by extrapolating the track position to the cluster position. Links from electron bremsstrahlung to photons are found by extrapolating tangents of the tracks to the cluster position, and from photon conversions to electron-positron pairs by comparing the converted photon direction to the track tangents. Links between the ECAL and the HCAL are found by extrapolating the cluster positions. For tracks in the tracker, links are found through a common secondary vertex. From the tracker to the muon detector, links are used to form global and tracker muons.

The link algorithm produces PF blocks of elements. For each PF block, particles are identified and reconstructed in a specific order, with the corresponding PF elements removed from the PF block before identifying and reconstructing the next particle. The order for the identification starts with muons, then proceeds to electrons and isolated photons, and finishes with hadrons and nonisolated photons.

The different interactions of each type of particle with the CMS detector allows the particles to be distinguished. In this way, the PF reconstruction produces a global event description with individually-identified muons, electrons, photons, charged hadrons, and neutral hadrons.

3.3.5 Jets

Jets are reconstructed from PF candidates using the anti-k_{T} algorithm [31, 32] with a distance parameter of 0.4. Before clustering the PF candidates into jets, charged PF candidates thought to be from pileup interactions are removed by checking whether the associated tracks are used in a pileup primary vertex. Jet energy corrections are derived from simulation to bring the measured response of jets to that of particle level jets on average.

To reject noise, jets are required to have number of constituents > 1, neutral

hadron energy fraction < 0.9, neutral EM energy fraction < 0.9, and muon energy fraction < 0.8. Jets with $|\eta| < 2.4$ are additionally required to have charged hadron energy fraction > 0, charged multiplicity > 0, and charged EM energy fraction < 0.90.

The jet energy resolution amounts typically to 15–20% at 30 GeV, 10% at 100 GeV, and 5% at 1 TeV [33].

The analysis described in this dissertation uses pp collision events delivered by the LHC and collected by the CMS experiment. The most important objects used in the analysis are displaced vertices reconstructed using a custom algorithm from tracks measured in the pixel and strip tracker. The analysis also uses jets for event selection. The next chapter describes the details of the analysis.

CHAPTER 4

SEARCH FOR DISPLACED VERTICES IN MULTIJET EVENTS

This chapter describes the details of the search for long-lived particles with displaced vertices in the 2015 and 2016 CMS data. To search for these long-lived exotic particles, displaced vertices are reconstructed from tracks in multijet events. We distinguish signal in events with two vertices using the distance between vertices. The SM background consists of mostly prompt vertices in events with multiple jets, and is dominated by events with only one vertex. The analysis is an improved version of a similar search in the 2012 CMS data [16].

The chapter is organized as follows. Section 4.1 discusses the event samples used, which include data samples and simulated samples. Section 4.2 describes the event preselection requirements. Section 4.3 describes the vertex reconstruction and vertex selection requirements. Section 4.4 describes the search strategy. Section 4.5 explains the estimation of the background using data. Section 4.6 discusses the systematic uncertainties in the signal efficiency and background estimate. Section 4.7 explains the signal extraction and statistical interpretation. Section 4.8 presents a method for reinterpretation of the analysis.

4.1 Event samples

4.1.1 Data samples

The data sample used in this analysis corresponds to a total integrated luminosity of $38.5\,\text{fb}^{-1}$, collected in pp collisions at $\sqrt{s} = 13\,\text{TeV}$ in 2015 and 2016.

Figure 4.1 shows the total integrated luminosity as a function of time, delivered by the LHC and recorded by CMS in 2015 and 2016. The difference between the amounts delivered by the LHC and recorded by CMS are due to data-taking

inefficiencies, which can include downtime if a subsystem is not ready for data acquisition, or deadtime if the instantaneous trigger rate is too high.

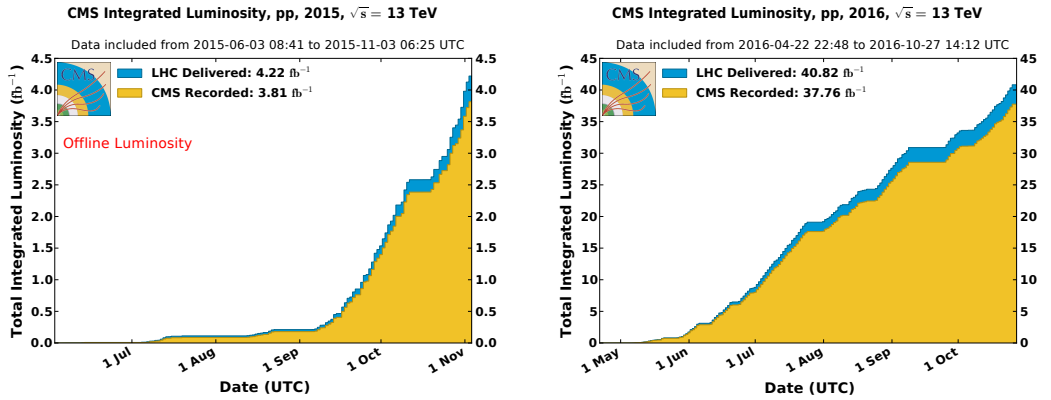

https://twiki.cern.ch/twiki/bin/view/CMSPublic/LumiPublicResults

Figure 4.1: Cumulative integrated luminosity delivered by the LHC and recorded by CMS, as a function of the calendar day in 2015 (left) and 2016 (right).

Additionally, the data recorded by CMS is validated by the CMS data certification group, and the data used in this analysis are only those declared as good for physics, corresponding to integrated luminosities of $2.6\,\text{fb}^{-1}$ in 2015 and $35.9\,\text{fb}^{-1}$ in 2016. The data can be flagged as bad for various reasons, such as a problem with the data quality from a subdetector.

Table 4.1 lists the data-taking eras used in this analysis. We use versions of the samples that are reconstructed with the best available tracker alignment and other relevant conditions, as well as with patches and fixes to the software. These versions are referred to as the "re-reco".

A particular feature present in the data from 2015 and 2016 eras B–F is a dynamic inefficiency in the strip tracker where, depending on the instantaneous luminosity and thus occupancy of the strip modules, signal-to-noise is reduced in strip hit clusters, hits are lost, and tracks are shorter or lost. This inefficiency is known as the "HIP" effect. It is particularly noticeable in the data from eras E+F of 2016, when the instantaneous luminosity was at its highest before the problem

Table 4.1: Data-taking eras used in this analysis. The uncertainty in the integrated luminosity is 2.3% for 2015 [2] and 2.5% for 2016 [3].

Era	Run range	Integrated luminosity (fb^{-1})
2015C	254227–255031	0.02
2015D	256630–260727	2.60
2016B	272007–275376	5.75
2016C	275657–276283	2.57
2016D	276315–276811	4.24
2016E	276831–277420	4.03
2016F	277772–278808	3.11
2016G	278820–280385	7.58
2016H	281207–284068	8.65

was fixed in the last runs of era F. The "re-reco" for 2016 eras B–F includes a change to the hit-trajectory association in glued modules, especially in the first layer of the tracker outer barrel, increasing the hit association efficiency and the track length and quality. This leads to a larger fake rate, but our analysis is not sensitive to this; instead it is sensitive to the loss in tracking efficiency.

4.1.2 Simulated samples

Monte Carlo (MC) simulation is used to model both the signal and background processes. The simulated events are described in the following subsections.

Signal

In the multijet and dijet signal models, long-lived particles are produced in pairs; the "multijet" and "dijet" refer to the decay of each long-lived particle. For the multijet signals, the long-lived particle is a neutralino that undergoes a three-body decay into top, bottom, and strange quarks. In this analysis, the final results are the same if the neutralinos are replaced with gluinos. For the dijet signals, the long-lived particle is a top squark that decays into two down antiquarks. Signal samples with various neutralino or top squark masses M ($300 \leq M \leq 2600\,\mathrm{GeV}$)

and lifetimes τ ($0.1 \leq c\tau \leq 100\,\text{mm}$) are produced using PYTHIA 8.212 [34] with the NNPDF2.3QED parton distribution functions [35].

The multijet signal samples with neutralino masses 300, 400, 800, 1200, and 1600 GeV and lifetimes 100 μm, 300 μm, 1 mm, and 10 mm were produced centrally. Each sample consists of ~100000 events.

Figure 4.2 shows the distributions of mass and proper decay length for some example multijet signal samples.

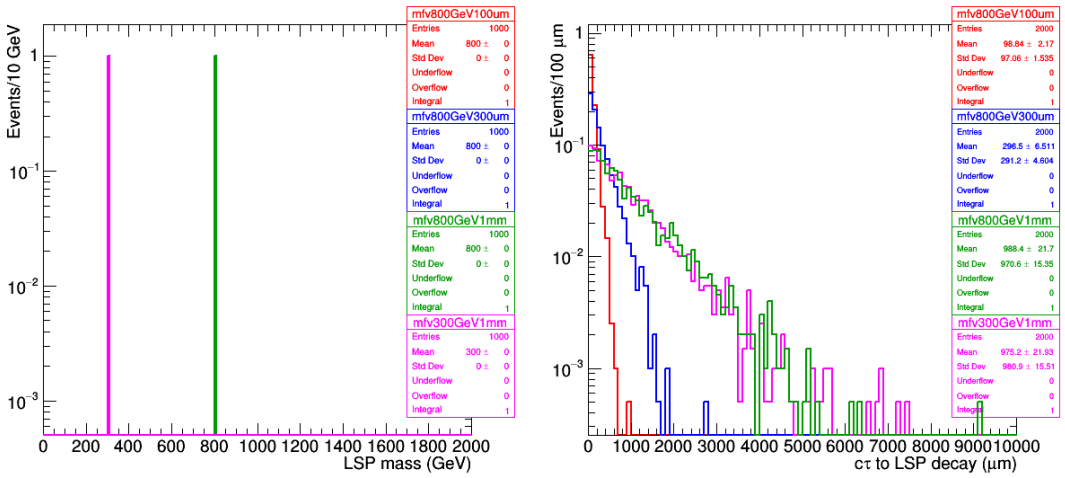

Figure 4.2: Distributions of LSP mass (left) and proper decay length (right) for multijet signal samples with $M = 800\,\text{GeV}$, $c\tau = 100\,\mu$m (red), 300 μm (blue), 1 mm (green), and $M = 300\,\text{GeV}$, $c\tau = 1\,\text{mm}$ (magenta).

In order to extend the signal scan range to more masses and lifetimes, private samples with ~10000 events were generated, simulated, and reconstructed, with the same configuration of simulation and reconstruction as the official samples. To ensure that the private generation was done correctly, a couple of points were duplicated with the official samples. The distributions of relevant variables (jet multiplicity, jet energy, vertex multiplicity, vertex decay position, etc.) are statistically the same.

To study models with smaller vertex track multiplicity, dijet samples in which

pair-produced, long-lived top squarks decay into two down antiquarks were privately produced, with the same configuration of simulation and reconstruction as the multijet samples. (The "dijet" refers to what the top squark decay produces; there are four quarks produced in the events: two down antiquarks from the top squark decay and two down quarks from the top antisquark decay.)

To check the effect of the different configurations for simulation and reconstruction between the 2015 and 2016 eras, additional multijet signal samples were produced with the 2015 configurations.

Background

Backgrounds arising from SM processes are dominated by multijet (QCD) and top quark pair production ($\mathrm{t\bar{t}}$) events. The multijet processes include b quark pair production events. The multijet and $\mathrm{t\bar{t}}$ events are simulated using MadGraph 5.2.2.2 [36] with the NNPDF3.0 parton distribution functions [37], at leading order for the multijet events and at next-to-leading order for the $\mathrm{t\bar{t}}$ events.

Tables 4.2 and 4.3 list the MC background samples for 2015 and 2016, respectively. The MC simulation representing the QCD background processes is split into several samples by H_{T}, which is the scalar sum of the p_{T} of jets in the event. Weights are applied to the simulated events such that the total event yield is representative of the data. For each background process, the weight is calculated by multiplying the integrated luminosity of the data by the cross section for the process, then dividing by the number of events generated. The 2015 and 2016 background datasets are mostly the same simulated events, with a small fraction of events dropped in one but not the other, except for $\mathrm{t\bar{t}}$, for which there are more events in the different 2016 sample. Therefore, differences in yields and distributions are mainly due to the different pileup and reconstruction configurations between the two eras.

Table 4.2: MC samples representing the SM background in the 2015 data. For each sample: the physics process, its cross section, the number of events generated, and the weight applied to each event such that the total event yield is representative of the data. The weight is calculated from the total integrated luminosity multiplied by the cross section for the process, divided by the number of events generated.

Process	Cross section (pb)	Number of events	Weight for $2.6\,\text{fb}^{-1}$
QCD, $500 < H_\text{T} < 700\,\text{GeV}$	3.2×10^4	19701790 + 43242884 = 62944674	1.31
QCD, $700 < H_\text{T} < 1000\,\text{GeV}$	6.8×10^3	15547962 + 29569683 = 45117645	0.39
QCD, $1000 < H_\text{T} < 1500\,\text{GeV}$	1.2×10^3	5085104 + 10246203 = 15331307	0.21
QCD, $1500 < H_\text{T} < 2000\,\text{GeV}$	120	3952170 + 7815090 = 11767260	0.03
QCD, $H_\text{T} > 2000\,\text{GeV}$	25	1981228 + 4016332 = 5997560	0.01
$\text{t}\bar{\text{t}}$	832	38493485	0.06

Table 4.3: MC samples representing the SM background in the 2016 data. For each sample: the physics process, its cross section, the number of events generated, and the weight applied to each event such that the total event yield is representative of the data. The weight is calculated from the total integrated luminosity multiplied by the cross section for the process, divided by the number of events generated.

Process	Cross section (pb)	Number of events	Weight for $35.9\,\text{fb}^{-1}$
QCD, $500 < H_\text{T} < 700\,\text{GeV}$	3.2×10^4	18929951 + 44061488 = 62991439	18.0
QCD, $700 < H_\text{T} < 1000\,\text{GeV}$	6.8×10^3	15629253 + 29808140 = 45437393	5.4
QCD, $1000 < H_\text{T} < 1500\,\text{GeV}$	1.2×10^3	4850746 + 10360193 = 15210939	2.8
QCD, $1500 < H_\text{T} < 2000\,\text{GeV}$	120	3970819 + 7868538 = 11839357	0.4
QCD, $H_\text{T} > 2000\,\text{GeV}$	25	1991645 + 4047360 = 6039005	0.2
$\text{t}\bar{\text{t}}$	832	43662343	0.7

HIP-effect samples

The HIP effect and mitigation are not included in the standard MC simulation samples, and so to measure their effects on the signal and background reconstruction, we privately produce small signal and QCD samples with the HIP simulation developed by the tracker DPG turned on, as well as with the HIP mitigation as in the data re-reco turned on.

Event simulation

For all samples, hadronization, showering, and R-hadron physics are simulated using PYTHIA 8.212. The underlying event tunes used are CUETP8M1 [38] for the signal samples and the multijet background samples, and CUETP8M2T4 [39] for the $\mathrm{t\bar{t}}$ samples. The detector response for all simulated samples is modeled using a GEANT4-based simulation [40] of the CMS detector. The effects of additional pp interactions within the same or nearby bunch crossings ("pileup") are included by overlaying additional simulated minimum-bias events, such that the resulting distribution of the number of interactions per bunch crossing matches that observed in the experiment.

Where applicable, simulated events enter histograms with a per-event weight calculated to sculpt the pileup distribution to resemble the data. The pileup weights are calculated separately for the MC samples representing the 2015 and 2016 datasets. The inefficiency in track and primary vertex reconstruction due to the HIP effect leads to disagreements in the related distributions (Figure 4.3), particularly visible in 2016 when the instantaneous luminosity was highest. This analysis is largely insensitive, however, to the presence of additional pileup tracks.

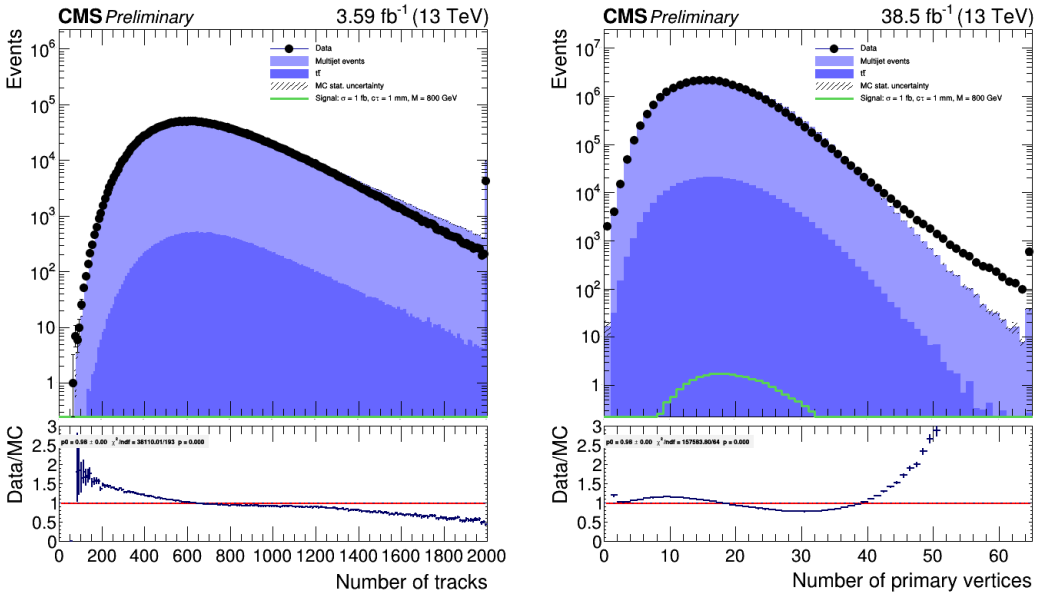

Figure 4.3: Distribution of number of tracks (left) and number of primary vertices (right), for data, simulated background normalized to data, and a simulated signal with LSP $c\tau = 1\,\text{mm}$, $M = 800\,\text{GeV}$, and production cross section 1 fb. Event preselection criteria have been applied.

4.2 Event preselection

4.2.1 Trigger requirements

Since we expect our signal to have many jets in the final state, we use triggers that impose requirements on jets. Events are selected using a trigger initially requiring $H_\text{T} > 800\,\text{GeV}$, where H_T is the scalar sum of the p_T of jets in the event with $p_\text{T} > 40\,\text{GeV}$. In the last data-taking period of 2016 (era H), corresponding to 22% of the total integrated luminosity, the higher instantaneous luminosity required the H_T threshold to be raised to 900 GeV. These triggers are referred to as `HLT_PFHT800` and `HLT_PFHT900`, respectively.

Additionally in 2016 era H, a bug in the H_T calculation at the L1 trigger in the consideration of saturated jets was introduced, resulting in a ∼20% inefficiency with respect to events with offline $H_\text{T} > 1000\,\text{GeV}$. A jet is "saturated" when

it leaves more energy in a calorimeter crystal than the maximum possible for the readout. The bug in this consideration is referred to as the "H_{T} saturation bug". It is seen in our data-driven trigger efficiency measurement described below (Fig. 4.7). The suggested cure to recover events with saturated jets is to take the logical-or of `HLT_PFHT900` with the two triggers `HLT_PFJet450` and `HLT_AK8PFJet450`; we refer to this as the "H path combination" in the following. These two triggers require a jet with $p_{\mathrm{T}} > 450\,\mathrm{GeV}$; for the second trigger, the jet is reconstructed using the anti-k_{T} algorithm with a distance parameter of 0.8, rather than the standard value of 0.4.

The `HLT_PFHT800` and `HLT_PFHT900` triggers were seeded by the logical-or of L1 paths with different thresholds in the 2015 and 2016 datasets, with at least one unprescaled: 100–175 GeV in 2015 and 160–320 GeV in 2016, with 200 GeV being the lowest enabled for any data taking. In the signal and background simulation, the seeds have the same logical-or structure, but all are unprescaled so that 100 and 160 GeV are the effective thresholds. For signal events passing the HLT H_{T} threshold and our offline jet requirements, however, the L1 H_{T} threshold does not affect the selection efficiency, and so we safely ignore these potential differences.

Figure 4.4 shows the efficiency of the triggers used as measured in the simulation as a function of signal topology, mass, and lifetime. For masses above 800 GeV, the overall trigger efficiency is above 95%. Samples with higher lifetimes (starting at ∼10 mm) lose efficiency (∼10–15%), as more displaced tracks are not found at HLT.

4.2.2 Offline jet requirements

For an event to be selected for further analysis, it must have at least four jets, each with $p_{\mathrm{T}} > 20\,\mathrm{GeV}$ and $|\eta| < 2.5$. Since the final states for the signal models

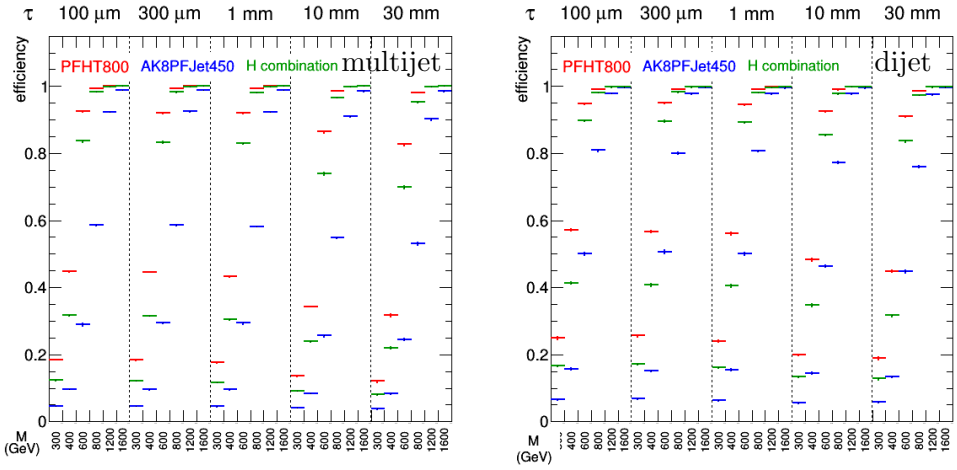

Figure 4.4: Trigger efficiency as a function of mass and lifetime, for multijet (left) and dijet (right) signal samples. `HLT_PFHT800` is the trigger path used for 2015 and 2016 eras B–G. The curve labeled "H combination" represents the combination of triggers used for 2016 era H, and is dominated almost entirely by `HLT_PFHT900`. The efficiency of the additional components in the H combination, `HLT_PFJet450 || HLT_AK8PFJet450`, is shown as a reference.

considered all have at least four quarks, this requirement has little impact on signal events but is beneficial in suppressing background.

To ensure that the efficiency of the H_{T} trigger is well understood, a stricter requirement of $H_{\mathrm{T}} > 1000\,\mathrm{GeV}$ is applied offline, where H_{T} is the scalar sum of the p_{T} of jets with $p_{\mathrm{T}} > 40\,\mathrm{GeV}$, to match the trigger jet definition. For events with at least four jets and $H_{\mathrm{T}} > 1000\,\mathrm{GeV}$, the trigger efficiency, determined using events satisfying a trigger requiring the presence of at least one muon, is $(99 \pm 1)\%$. The data-driven trigger efficiency measurement is described in the following subsection.

Figure 4.5 shows the distributions of the variables used for event preselection.

4.2.3 Data-driven trigger efficiency measurement

To measure the efficiency of the jet trigger paths used, we use muon-triggered events in which there are an isolated muon and four or more jets reconstructed

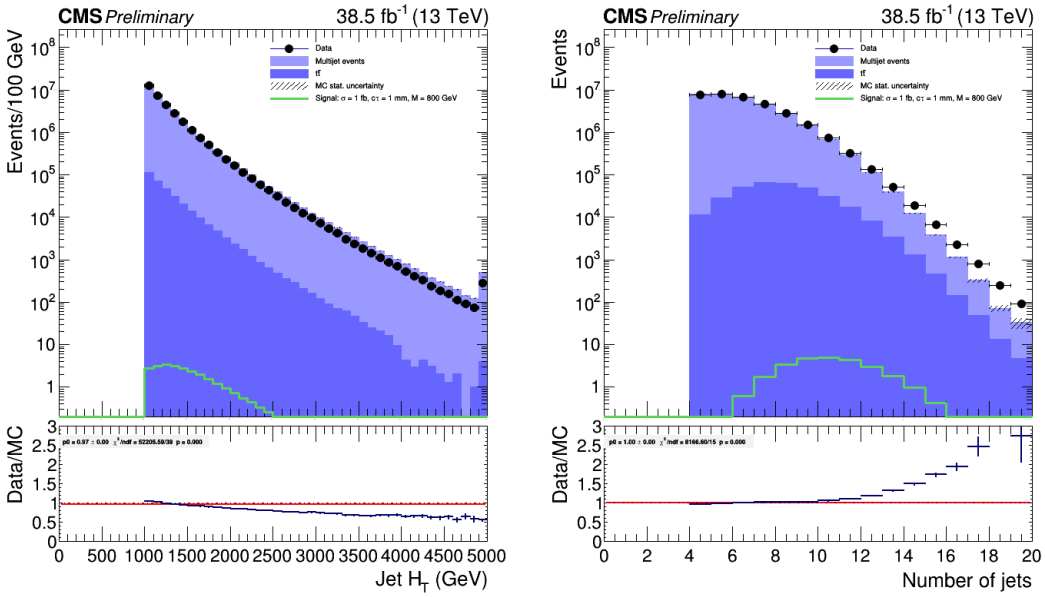

Figure 4.5: Distributions of variables used for event preselection, for data, simulated background normalized to data, and a simulated signal with LSP $c\tau = 1\,\text{mm}$, $M = 800\,\text{GeV}$, and production cross section 1 fb. Event preselection criteria have been applied. (Left) H_T, the scalar sum of the p_T of jets in the event with $p_\text{T} > 40\,\text{GeV}$, is required to be at least 1000 GeV. (Right) The number of jets in the event is required to be at least four.

offline, and calculate the trigger efficiency as a function of offline jet H_{T}.

Single-muon triggered events are found in the datasets corresponding to the different data-taking eras (Table 4.1), with subpercent differences in the luminosity sections available. To derive a scale factor representing the difference in the data and simulation for the signal sample normalization, muon-enriched simulated samples representing the most relevant, largest cross-section physics processes are used. These samples are listed in Table 4.4.

Table 4.4: Simulated samples used in the trigger efficiency study.

Process
W+jets, $W \to \ell\nu$
Z/γ^*+jets, $Z/\gamma^* \to \ell\ell$, generated $10 < M_{\ell\ell} < 50\,\mathrm{GeV}$
Z/γ^*+jets, $Z/\gamma^* \to \ell\ell$, generated $M_{\ell\ell} > 50\,\mathrm{GeV}$
$\mathrm{t\bar{t}}$
QCD, generated $\hat{p_{\mathrm{T}}} > 20\,\mathrm{GeV}$ & μ $p_{\mathrm{T}} > 15\,\mathrm{GeV}$

The sample of events that enter the denominator in the efficiency calculation is produced as follows. We select events firing the `HLT_IsoMu20` or `HLT_IsoMu24` trigger in 2015 or 2016, respectively, which requires the presence of an isolated muon with $p_{\mathrm{T}} > 20\,\mathrm{GeV}$ or $p_{\mathrm{T}} > 24\,\mathrm{GeV}$. We then require an offline-reconstructed muon to pass these cuts:

- $p_{\mathrm{T}} > 23\,\mathrm{GeV}$ (2015) or $p_{\mathrm{T}} > 27\,\mathrm{GeV}$ (2016)
- $|\eta| < 2.4$
- Global muon and PF muon
- Normalized global track $\chi^2 < 10$
- Number of inner tracker layers with hits > 5
- Number of pixel hits > 0
- Number of muon hits > 0 and number of matched muon stations > 1

We plot the L1*HLT trigger efficiency as a function of the offline jet H_{T}, and fit these curves with a function of the form

$$A + 0.5B\left(1 + \mathrm{erf}\frac{H_{\mathrm{T}} - \mu_{\mathrm{on}}}{\sigma_{\mathrm{on}}}\right) \tag{4.1}$$

where the weighted average of the efficiencies in the highest H_{T} bins, the plateau efficiency, is $A + B$, and μ_{on} and σ_{on} are the location and width of the turn-on, respectively. The turn-on curves for the different data eras and the overall weighted sum of the simulated samples are shown in Fig. 4.6 (`HLT_PFHT800`), Fig. 4.7 (`HLT_PFHT900`), and Fig. 4.8 (H path combination). The efficiencies, given as the total efficiency for events with offline $H_{\mathrm{T}} > 1000\,\mathrm{GeV}$, are given in Table 4.5 for data and simulation, along with the respective data/simulation ratios.

Table 4.5: Trigger efficiency for events with offline $H_{\mathrm{T}} > 1000\,\mathrm{GeV}$ in data and simulation, and the ratio, for different eras and trigger paths.

Trigger path	Efficiency	Eff. in sim.	Data/sim.
2015 `PFHT800`	0.998 ± 0.001	0.999 ± 0.001	0.998 ± 0.001
2016 B–G `PFHT800`	0.999 ± 0.001	0.999 ± 0.001	1.000 ± 0.001
2016 B–G `PFHT900`	0.993 ± 0.001	0.998 ± 0.002	0.995 ± 0.002
2016 H `PFHT900`	0.812 ± 0.004	0.998 ± 0.002	0.814 ± 0.004
2016 H combination	0.995 ± 0.001	0.999 ± 0.001	0.996 ± 0.001
2016 H combination, 6th jet $p_{\mathrm{T}} > 75\,\mathrm{GeV}$	0.98 ± 0.01	1 (lower limit 0.99)	0.98 ± 0.01

The recipe intended to emulate the 2016 H H_{T} saturation bug results in a turn-on curve not qualitatively like what is seen in the data: the emulated efficiency at offline $H_{\mathrm{T}} = 1000\,\mathrm{GeV}$ is close to one and falls off after that, while the efficiency measured in the H data is only $\sim$80% already at 1000 GeV. Events with energy spread among many jets, however, such as our multijet signals, may not suffer the bug in the first place. Instead of figuring out what is wrong with the emulation, we proceed as follows.

To gauge the applicability of these measurements to signal events, Figs. 4.9 and 4.10 compare the jet multiplicity and p_{T} in the samples used for the trigger

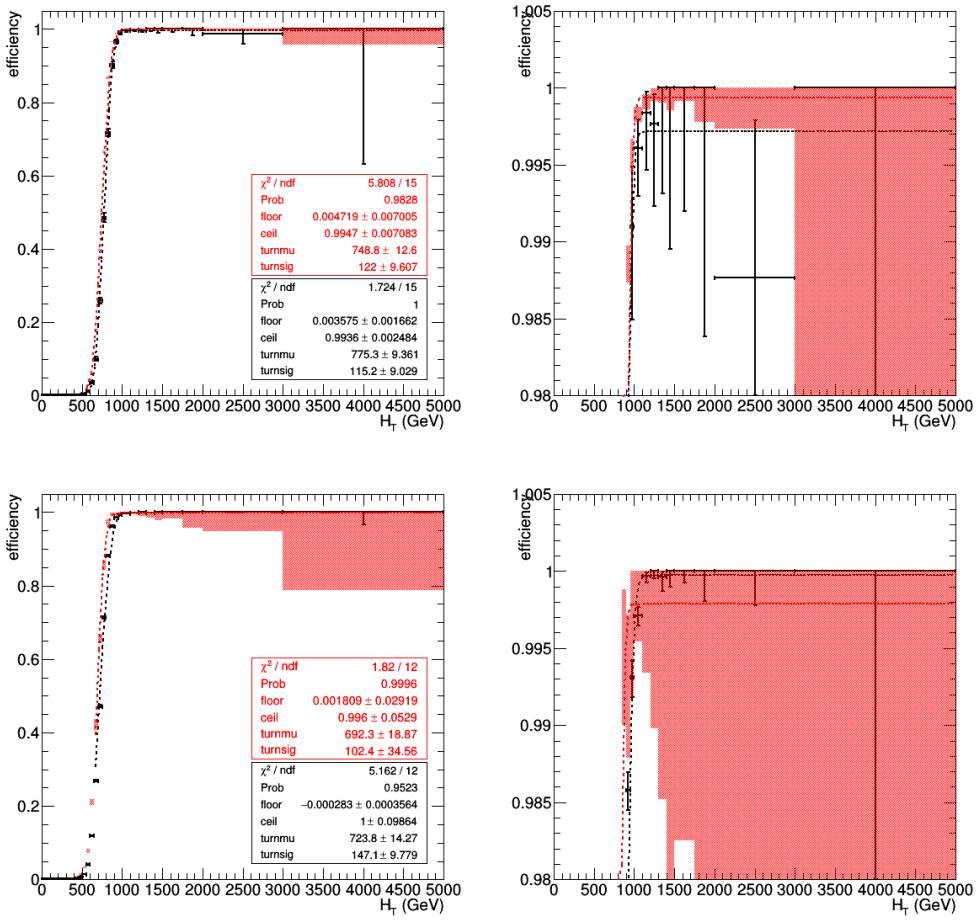

Figure 4.6: `HLT_PFHT800` efficiency as a function of offline jet H_{T} in muon-triggered events in the data (black crosses) and simulation (red shaded bands), for 2015 (top) and 2016 B–F eras (bottom). The right plots are zoomed-in versions of the left plots.

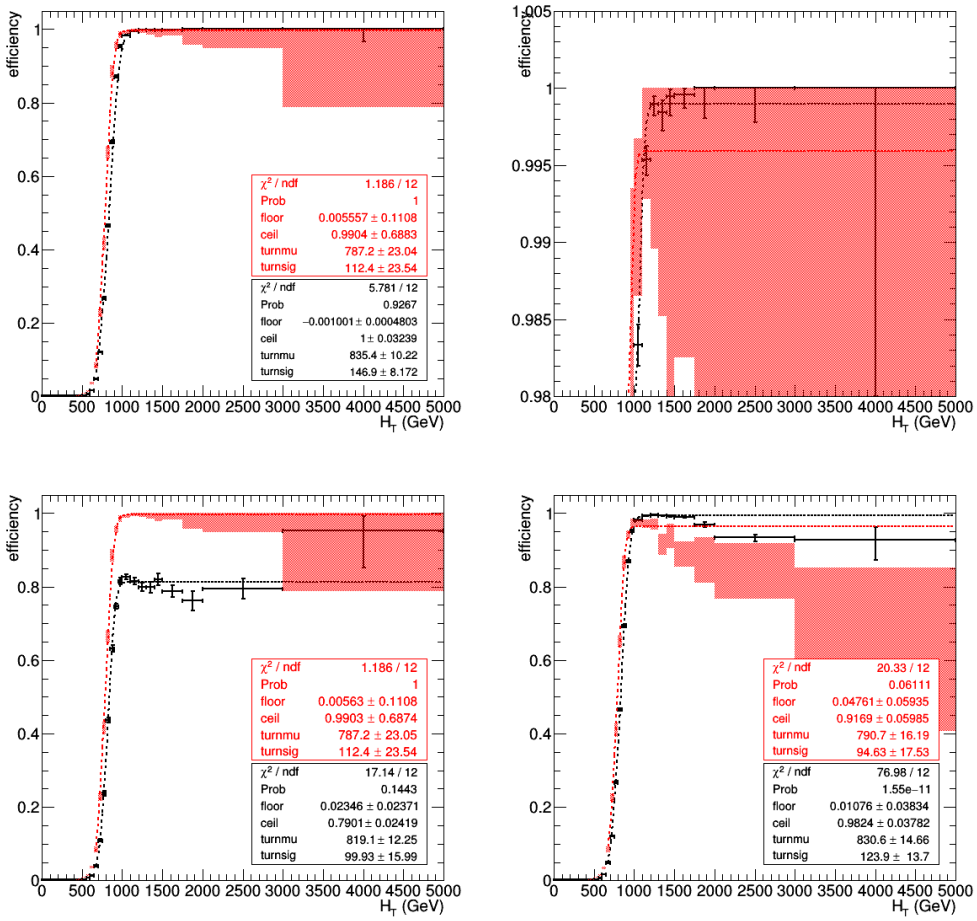

Figure 4.7: `HLT_PFHT900` efficiency as a function of offline jet H_{T} in muon-triggered events in the data (black crosses) and simulation (red shaded bands), for the 2016 B–G eras (top left and right, zoomed-in) and 2016 H era (bottom left). The bottom right plot shows the result of the simple emulation of the H_{T} saturation bug in the 2016 B–G data and simulation.

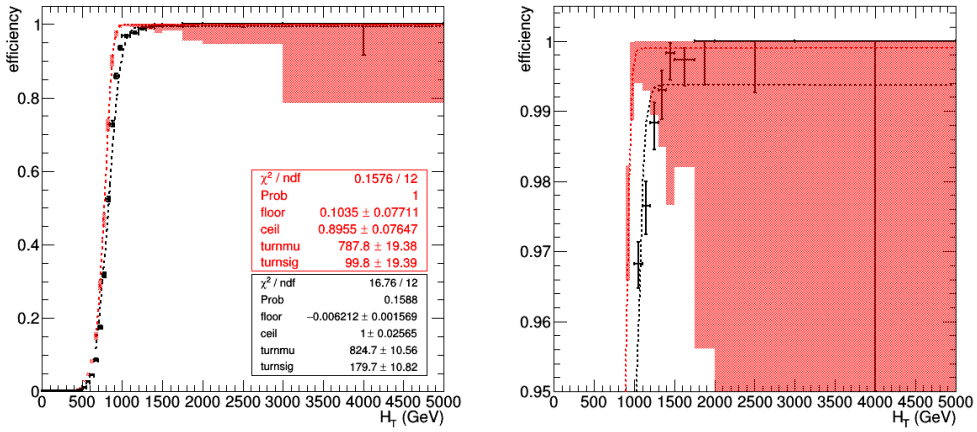

Figure 4.8: `HLT_PFHT900 || HLT_PFJet450 || HLT_AK8PFJet450` efficiency as a function of offline jet H_{T} in muon-triggered events in the data (black crosses) and simulation (red shaded bands), for the 2016 H era. The right plot is a zoomed-in version of the left plot.

measurements with simulated multijet and dijet signal samples. Multijet signal events have more jets (∼10) than the trigger measurement samples (∼6). The energy in signal events, for a given mass, is spread among more jets, so the saturation bug present in 2016 H is less likely to be hit. Furthermore, the events may be aided less by the inclusion of `HLT_(AK8)PFJet450`. Low-mass dijet signal events are closer to being fairly represented by the trigger measurement samples, but still the energy is more spread among more jets (∼7).

To obtain a more representative measurement, we use events with at least six jets and where the sixth jet has $p_{\mathrm{T}} > 75\,\mathrm{GeV}$ to obtain a sample closer in kinematics to the signal samples, and examine the turn-on curve of the H path combination shown in Fig. 4.11. The resulting efficiency for offline $H_{\mathrm{T}} > 1000\,\mathrm{GeV}$ is 0.98±0.01. The related data/simulation scale factor is the same number since the measured efficiency in the simulation is 1. We take the magnitude of the difference from one, 0.02, as the related systematic uncertainty.

Since the small differences in offline H_{T} due to the different trigger turn-on

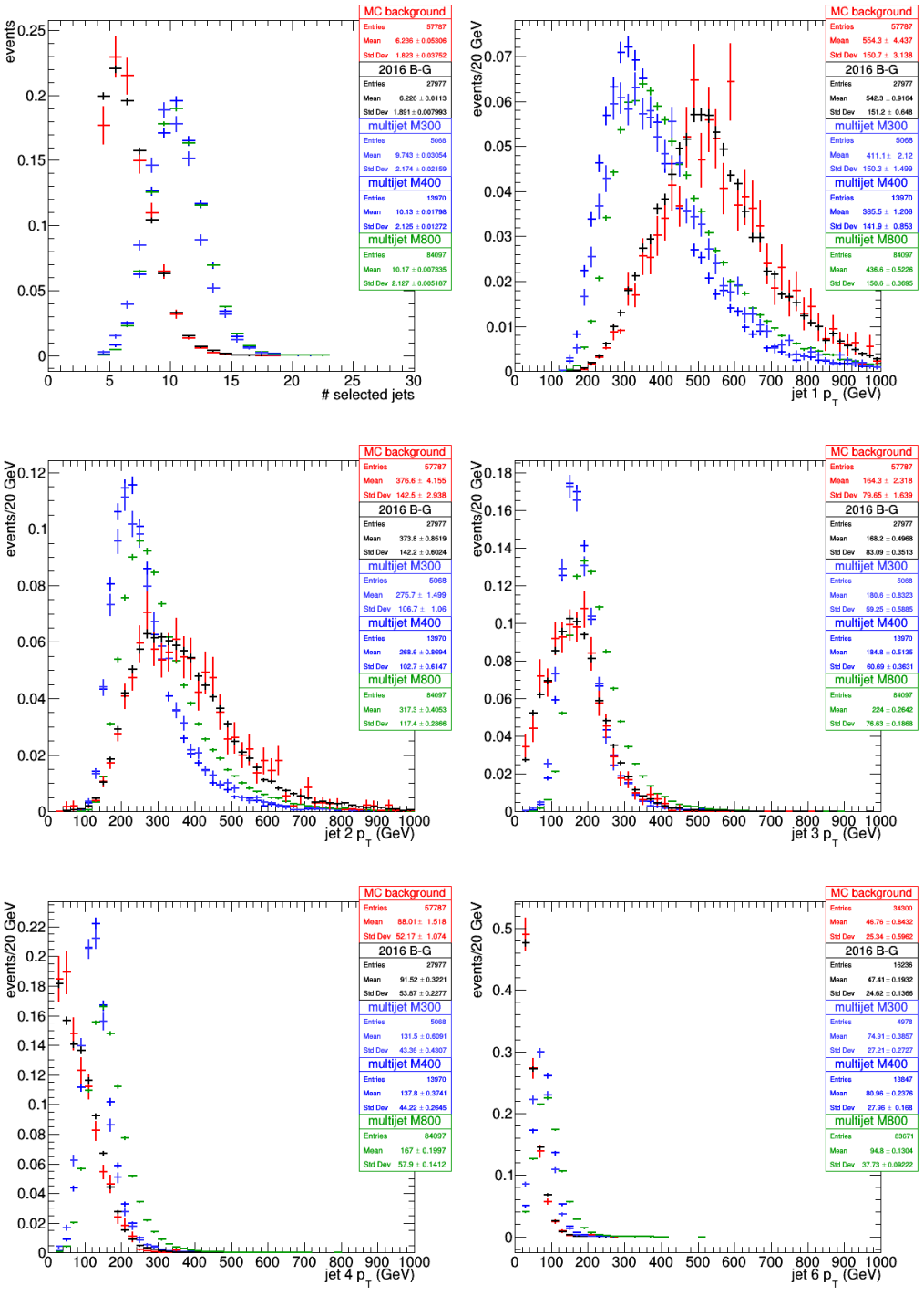

Figure 4.9: Jet multiplicity (upper left) and p_{T} for the first through fourth and sixth jets (upper right through bottom right) in 2016 B–G data, MC simulation, and simulated multijet signal samples with mean proper decay length 1 mm and masses 300, 400, and 800 GeV. Each distribution is normalized to 1.

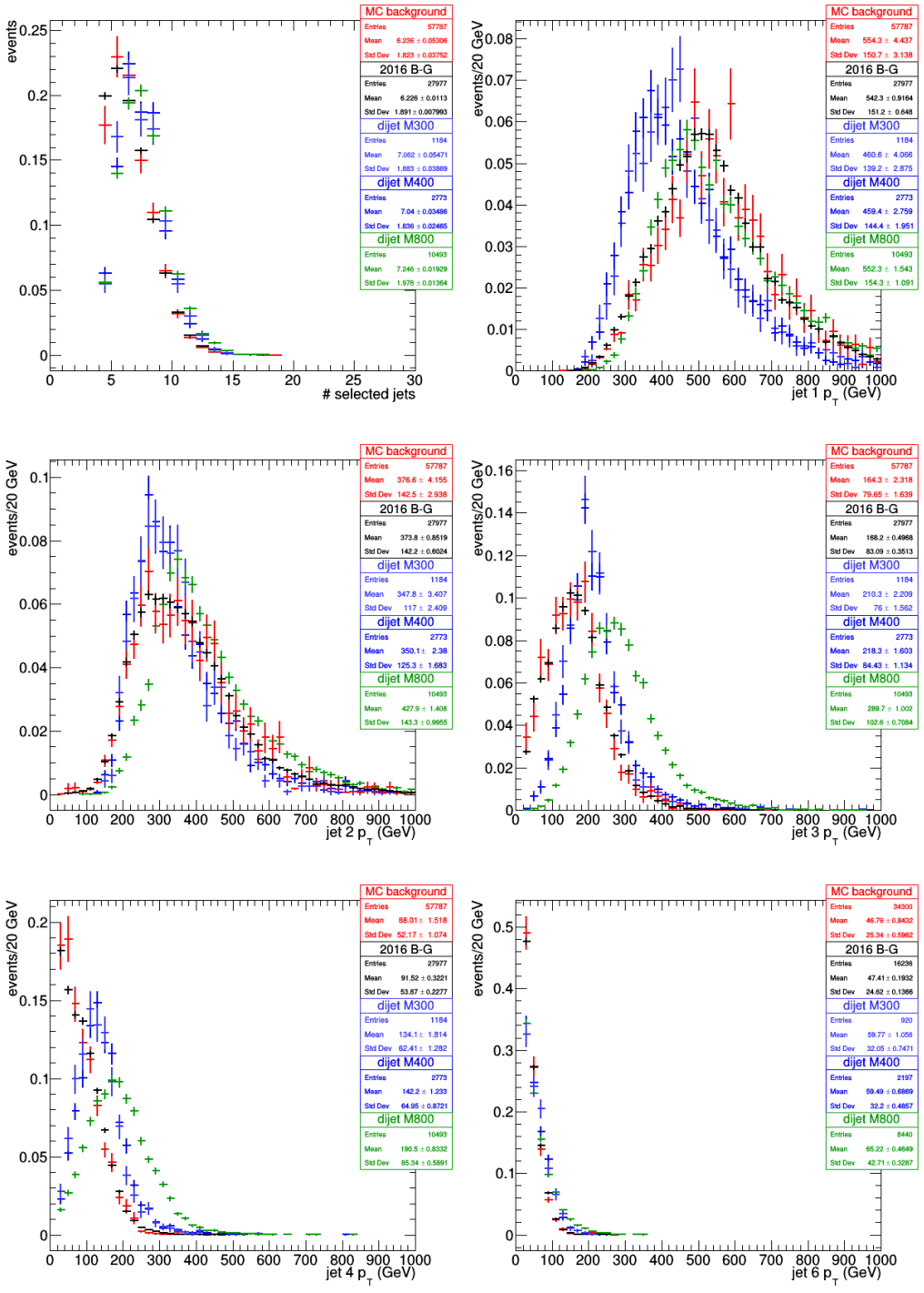

Figure 4.10: Jet multiplicity (upper left) and p_{T} for the first through fourth and sixth jets (upper right through bottom right) in 2016 B–G data, MC simulation, and simulated dijet signal samples with mean proper decay length 1 mm and masses 300, 400, and 800 GeV. Each distribution is normalized to 1.

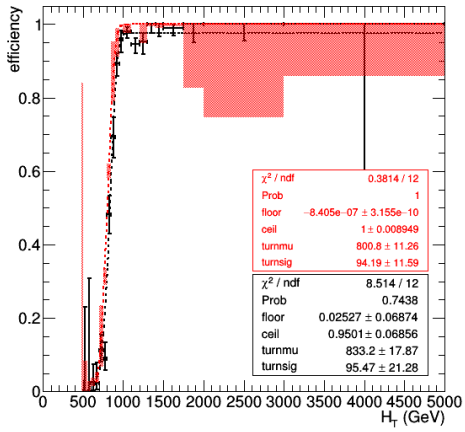

Figure 4.11: In events with at least six jets and with sixth jet $p_{\mathrm{T}} > 75\,\mathrm{GeV}$, `HLT_PFHT900 || HLT_PFJet450 || HLT_AK8PFJet450` efficiency as a function of offline jet H_{T} in muon-triggered events in 2016 H data (black crosses) and simulation (red shaded bands).

curves do not modify the signal lifetime shape, we simply use the luminosity weighted average of the different eras and arrive at an overall scale factor of 0.99, with related systematic uncertainty of 0.01.

4.3 Vertex reconstruction and selection

4.3.1 Track selection

Displaced vertices are reconstructed from tracks in the silicon tracker. These tracks are required to have $p_{\mathrm{T}} > 1\,\mathrm{GeV}$; measurements in at least two layers of the pixel detector, including one in the innermost layer; measurements in at least six layers of the strip detector if $|\eta| < 2$, or in at least seven layers if $|\eta| \geq 2$; and significance of the impact parameter with respect to the beam axis measured in the x-y plane (the magnitude of the impact parameter divided by its uncertainty, referred to as $|d_{xy}|/\sigma_{d_{xy}}$) of at least 4. The first three criteria are track quality requirements,

imposed in order to select tracks with small impact parameter uncertainties. The requirement on track $|d_{xy}|/\sigma_{d_{xy}}$ favors vertices that are displaced from the beam axis.

Figure 4.12 shows the distributions of the variables used for track selection.

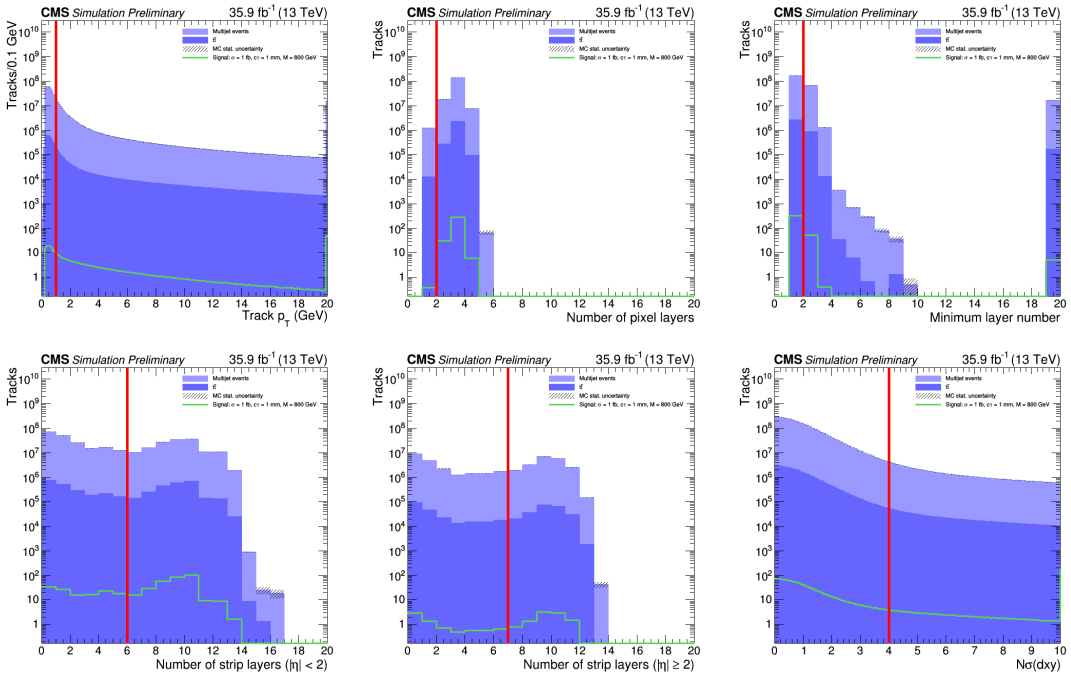

Figure 4.12: Distributions of variables used for track selection. These are "n-1" plots: all event preselection and track selection criteria have been applied, except for the one related to the variable shown. (Top left) The p_{T} of the track is required to be at least 1 GeV. (Top middle) The number of pixel layers is required to be at least 2. (Top right) The minimum layer number is required to be 1. (Bottom left) If $|\eta| < 2$, the number of strip layers is required to be at least 6. (Bottom middle) If $|\eta| \geq 2$, the number of strip layers is required to be at least 7. (Bottom right) The transverse impact parameter significance is required to be at least 4.

We chose the value of the $|d_{xy}|/\sigma_{d_{xy}}$ requirement based on a study of the statistical uncertainty in our predicted background yield in the signal region. As the requirement is tightened, the number of events to be used for the background estimation decreases, until the uncertainty in the predicted yield is approximately equal to the predicted yield itself. Using a toy model of our method for background

estimation from the Run 1 analysis and an estimate of the integrated luminosity for 2015, we found that requiring $|d_{xy}|/\sigma_{d_{xy}} > 4$ resulted in a background yield that was comparable to the statistical uncertainty in its prediction.

We reoptimized the number of strip layers requirement after observing disagreement between data and MC simulation in the distribution for seed tracks, in 10% of the data. The problem was consistent with the HIP effect: there was an excess of tracks with small numbers of strip layers that increased with instantaneous luminosity but decreased after the fix between the 2016 BCDEF and GH eras. These misreconstructed tracks were more likely to be in the η overlap regions. Figure 4.13 shows the distributions of the number of strip layers in seed tracks, and Figure 4.14 shows the distributions of the number of strip layers as a function of track η. Figures 4.15 and 4.16 show the distributions of the number of strip layers in seed tracks with $|\eta| < 2$ and $|\eta| \geq 2$, respectively.

4.3.2 Vertex reconstruction

The vertex reconstruction algorithm forms seed vertices from all pairs of tracks satisfying the track selection criteria, and then merges them iteratively until no track is used more than once. A set of tracks is considered to be a vertex if a fit with the Kalman filter approach [41] has a χ^2 per degree of freedom (χ^2/dof) that is less than 5. Subsequently, for each pair of vertices that shares a track, the vertices are merged if the three-dimensional distance between the vertices is less than 4 times the uncertainty in that distance and the fit has $\chi^2/\text{dof} < 5$. Otherwise, the shared track is assigned to one of the vertices depending on the value of its three-dimensional impact parameter significance with respect to each of the vertices: if both values are less than 1.5, the shared track is assigned to the vertex that has more tracks already; if either value is greater than 5, the shared

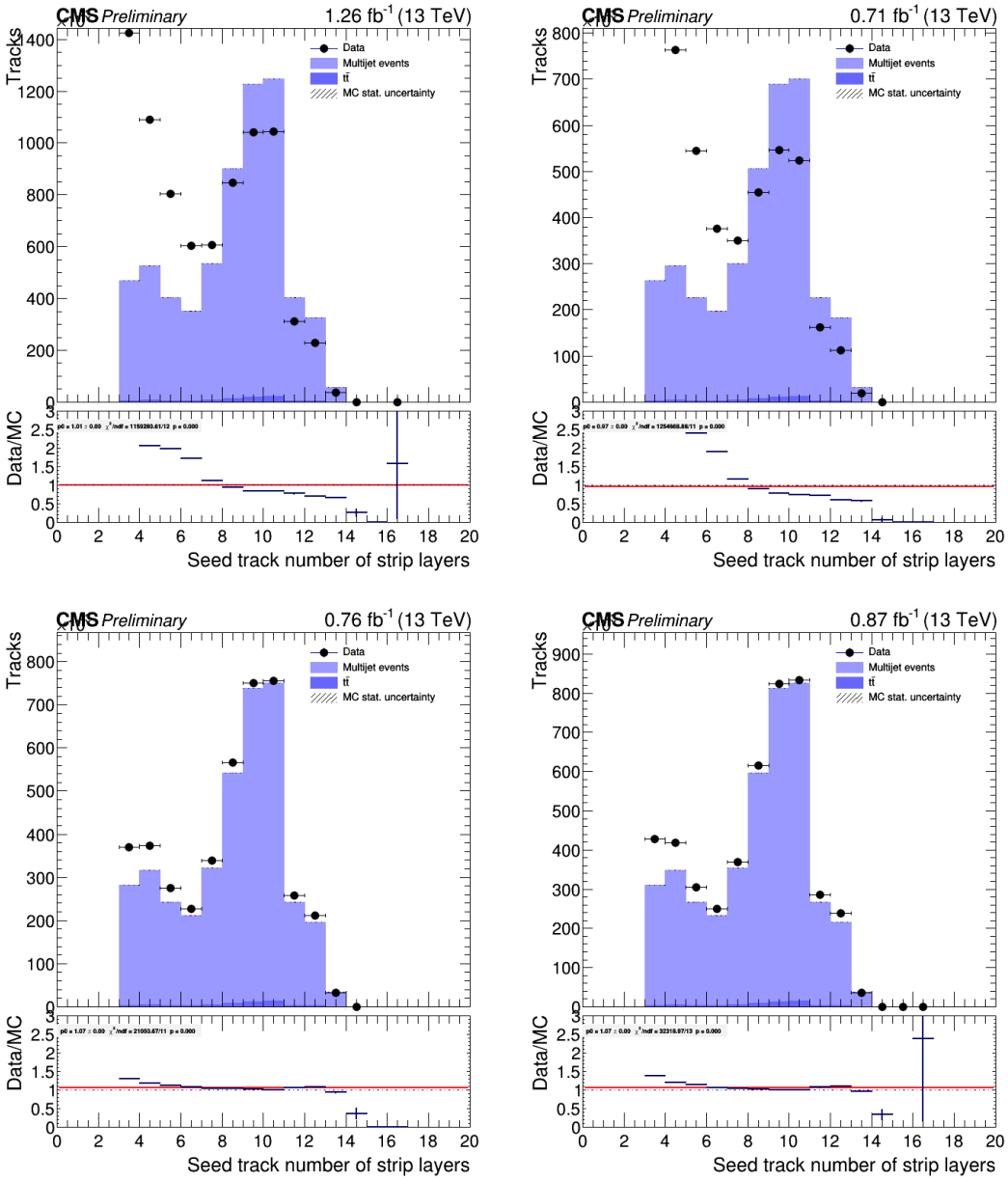

Figure 4.13: Distributions of the number of strip layers in seed tracks, for simulated background compared with 10% of the 2016 data in the BCD (top left), EF (top right), G (bottom left), and H (bottom right) data-taking eras. In these plots, the requirement on the number of strip layers has been relaxed to 3; for the analysis, the tracks are required to have at least 6 strip layers if $|\eta| < 2$ and at least 7 strip layers if $|\eta| \geq 2$.

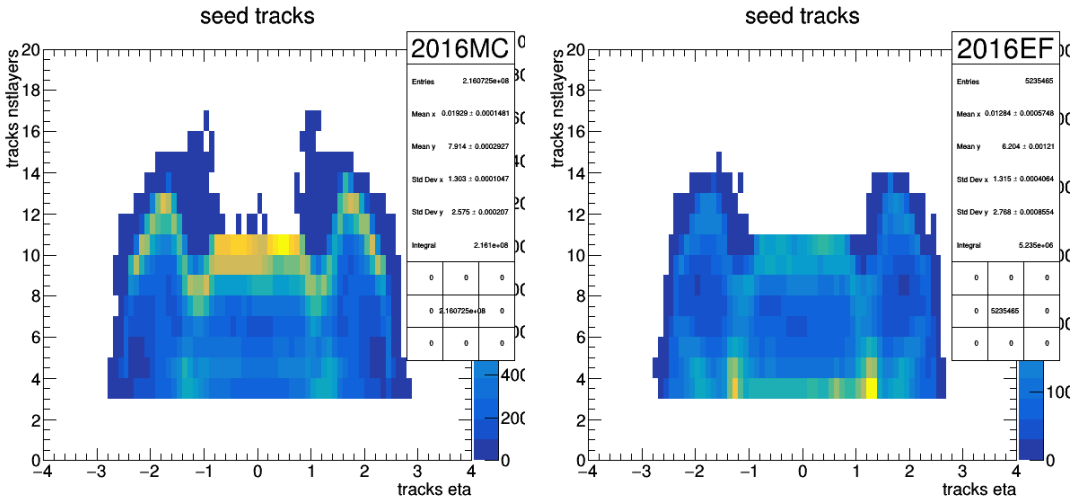

Figure 4.14: Distributions of the number of strip layers in seed tracks as a function of track η, in simulated background (left) and 10% of the 2016 data in the E+F data-taking eras (right). In these plots, the requirement on the number of strip layers has been relaxed to 3; for the analysis, the tracks are required to have at least 6 strip layers if $|\eta| < 2$ and at least 7 strip layers if $|\eta| \geq 2$.

track is dropped from that vertex; otherwise, the shared track is assigned to the vertex with respect to which it has a smaller impact parameter significance. If a track is removed from a vertex, that vertex is refit, and if the fit satisfies the requirement of $\chi^2/\text{dof} < 5$, the old vertex is replaced with the new one; otherwise it is dropped entirely.

4.3.3 Vertex selection

This procedure produces multiple vertices per event, only some of which are signal-like. In order to select vertices with high quality, we impose additional requirements: each vertex is required to have at least five tracks; a distance from the detector origin measured in the x-y plane of less than 20 mm, to avoid vertices from interactions in the beam pipe or detector material; a distance from the beam axis measured in the x-y plane, defined as d_{BV}, of at least 0.1 mm, to suppress displaced primary vertices; and an uncertainty in d_{BV} of less than 25 μm, to select

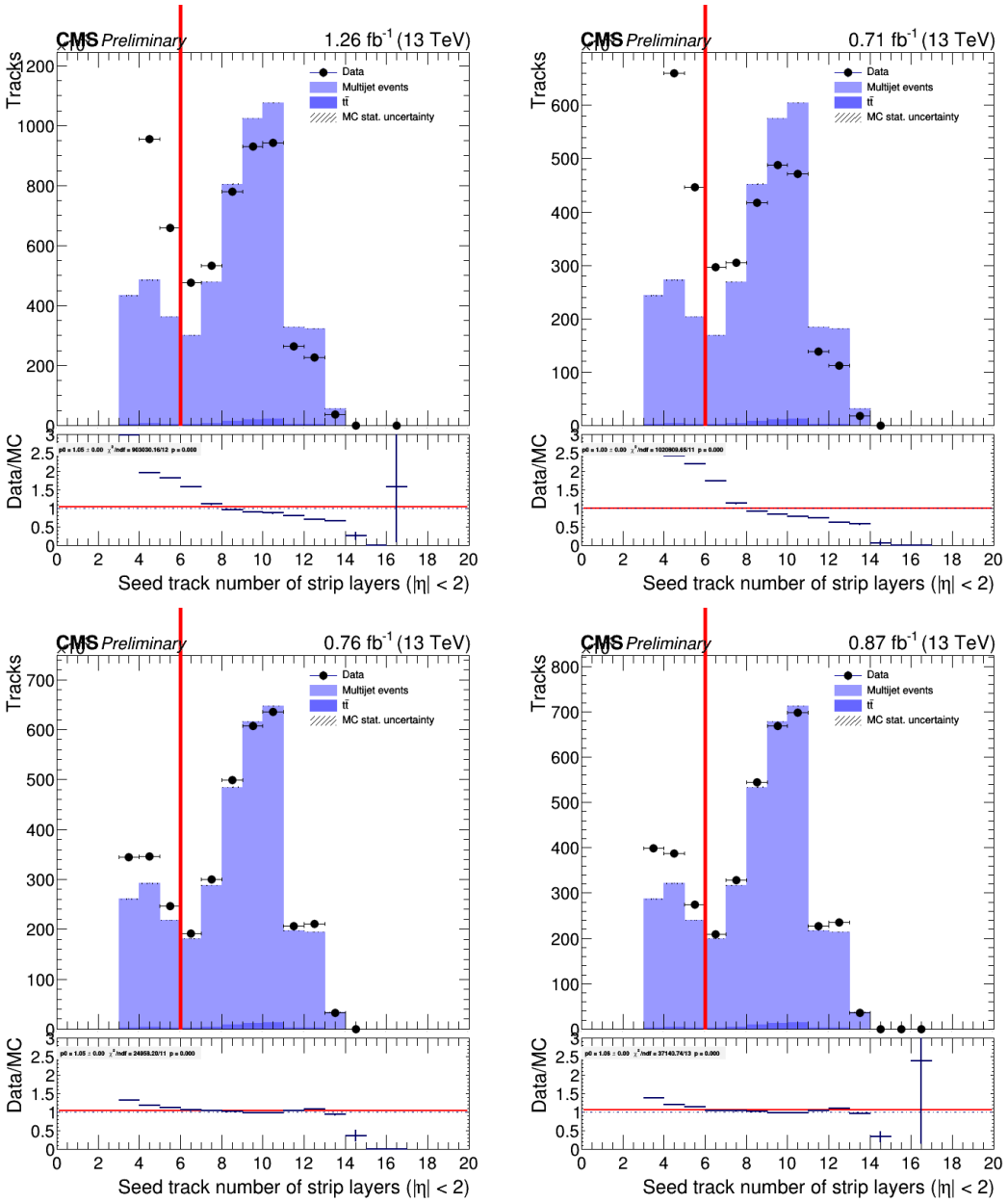

Figure 4.15: Distributions of the number of strip layers in seed tracks with $|\eta| < 2$, for simulated background compared with 10% of the 2016 data in the BCD (top left), EF (top right), G (bottom left), and H (bottom right) data-taking eras. In these plots, the requirement on the number of strip layers has been relaxed to 3; for the analysis, the tracks are required to have at least 6 strip layers if $|\eta| < 2$ and at least 7 strip layers if $|\eta| \geq 2$.

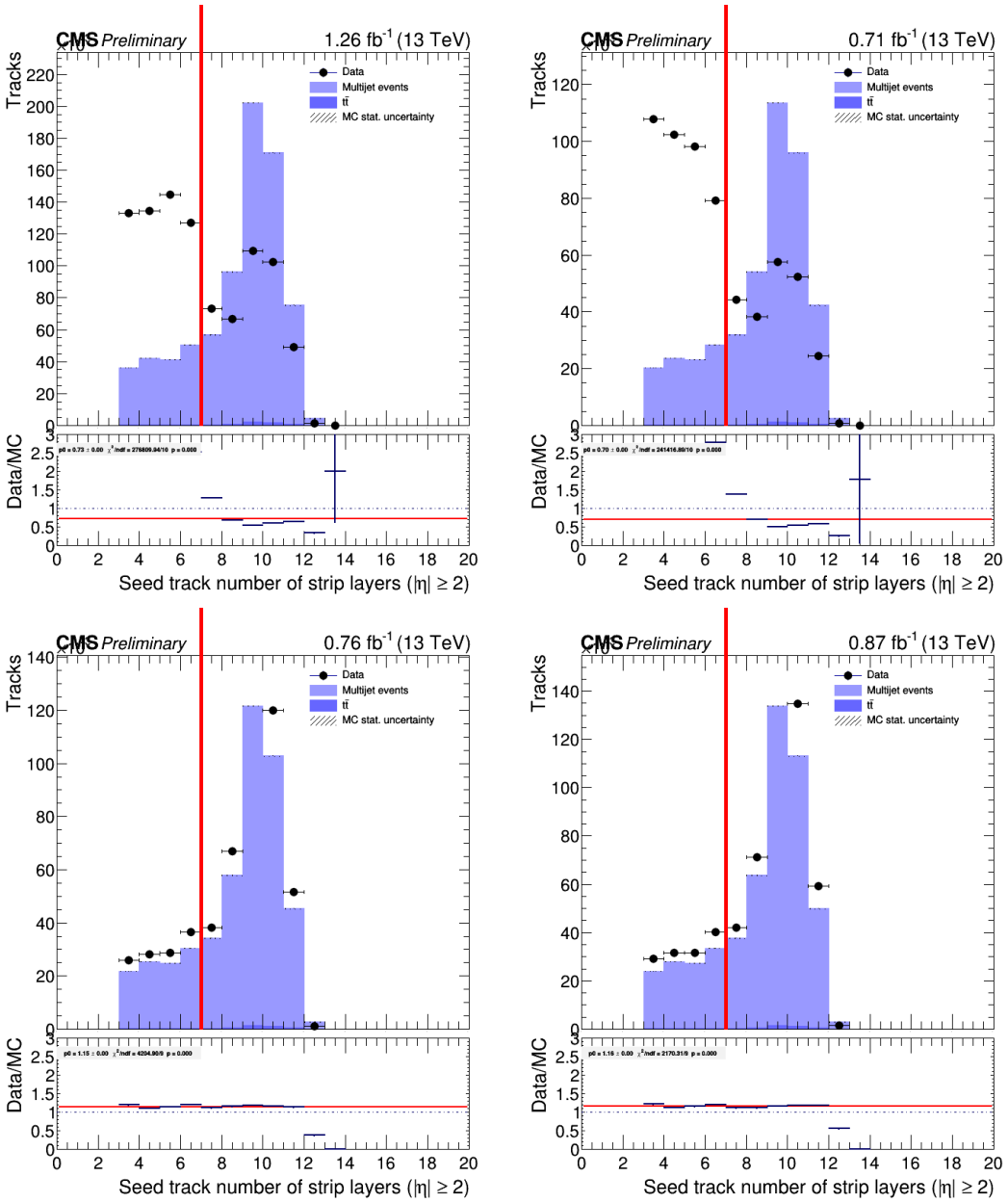

Figure 4.16: Distributions of the number of strip layers in seed tracks with $|\eta| \geq 2$, for simulated background compared with 10% of the 2016 data in the BCD (top left), EF (top right), G (bottom left), and H (bottom right) data-taking eras. In these plots, the requirement on the number of strip layers has been relaxed to 3; for the analysis, the tracks are required to have at least 6 strip layers if $|\eta| < 2$ and at least 7 strip layers if $|\eta| \geq 2$.

only well-reconstructed vertices. The requirement on the uncertainty in d_{BV} also suppresses displaced vertices from single b jets, which are composed of tracks that are mostly aligned with the vertex displacement from the beam axis and have small opening angles between the tracks.

Figure 4.17 shows the distributions of the variables used for vertex selection.

Since signal events contain a pair of long-lived particles, we require events to have two or more vertices satisfying the above requirements. The signal region is composed of these two-vertex events. Simulation predicts there is on the order of 1 background event in the signal region for $38.5\,\mathrm{fb}^{-1}$ of data. However, establishing the possible presence of a signal relies on an accurate determination of the background, and for this we rely on data.

The vertex selection requires each vertex to have five or more tracks, but events with vertices with three or four tracks provide valuable control samples. These control samples, which are used to test the background prediction, have a factor of 10–100 more background events than in the signal region and negligible potential signal contamination. Simulation studies show that events containing 3-track, 4-track, and $\geq$5-track vertices have similar distributions of event variables, such as H_{T}, number of jets, and quark flavor composition, as well as vertex variables, such as d_{BV}, uncertainty in d_{BV}, and angular separation between tracks. Figure 4.18 shows the distributions of d_{BV} and the uncertainty in d_{BV} in 3-track and 4-track one-vertex events.

The events with exactly one vertex are used to estimate the background. Table 4.6 lists the MC yields for the events with 5-or-more-track vertices, and Table 4.7 lists the MC yields for the events with 3-track and 4-track vertices. Figure 4.19 shows the distributions of number of 3-track, 4-track, and 5-or-more-track vertices.

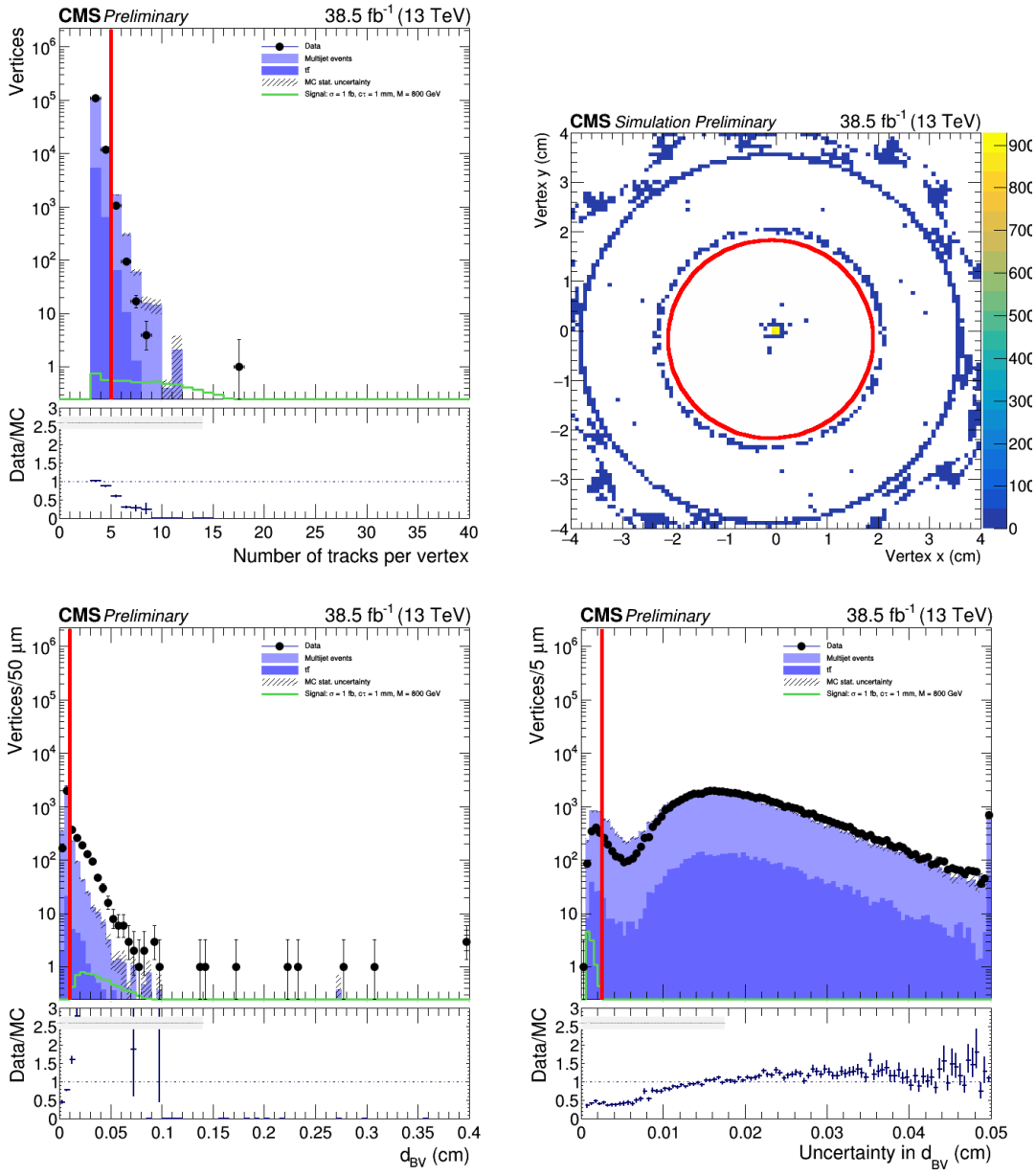

Figure 4.17: Distributions of variables used for vertex selection, in events with exactly one vertex, for the full 2015+2016 dataset compared with simulated background normalized to data. These are "n-1" plots: all event preselection and vertex selection criteria have been applied, except for the one related to the variable shown. (Top left) The number of tracks per vertex is required to be at least five. (Top right) The x-y distance of the vertex from the detector origin is required to be less than 20 mm. (Bottom left) The x-y distance of the vertex from the beam axis, d_{BV}, is required to be at least 100 μm. (Bottom right) The uncertainty in d_{BV} is required to be less than 25 μm.

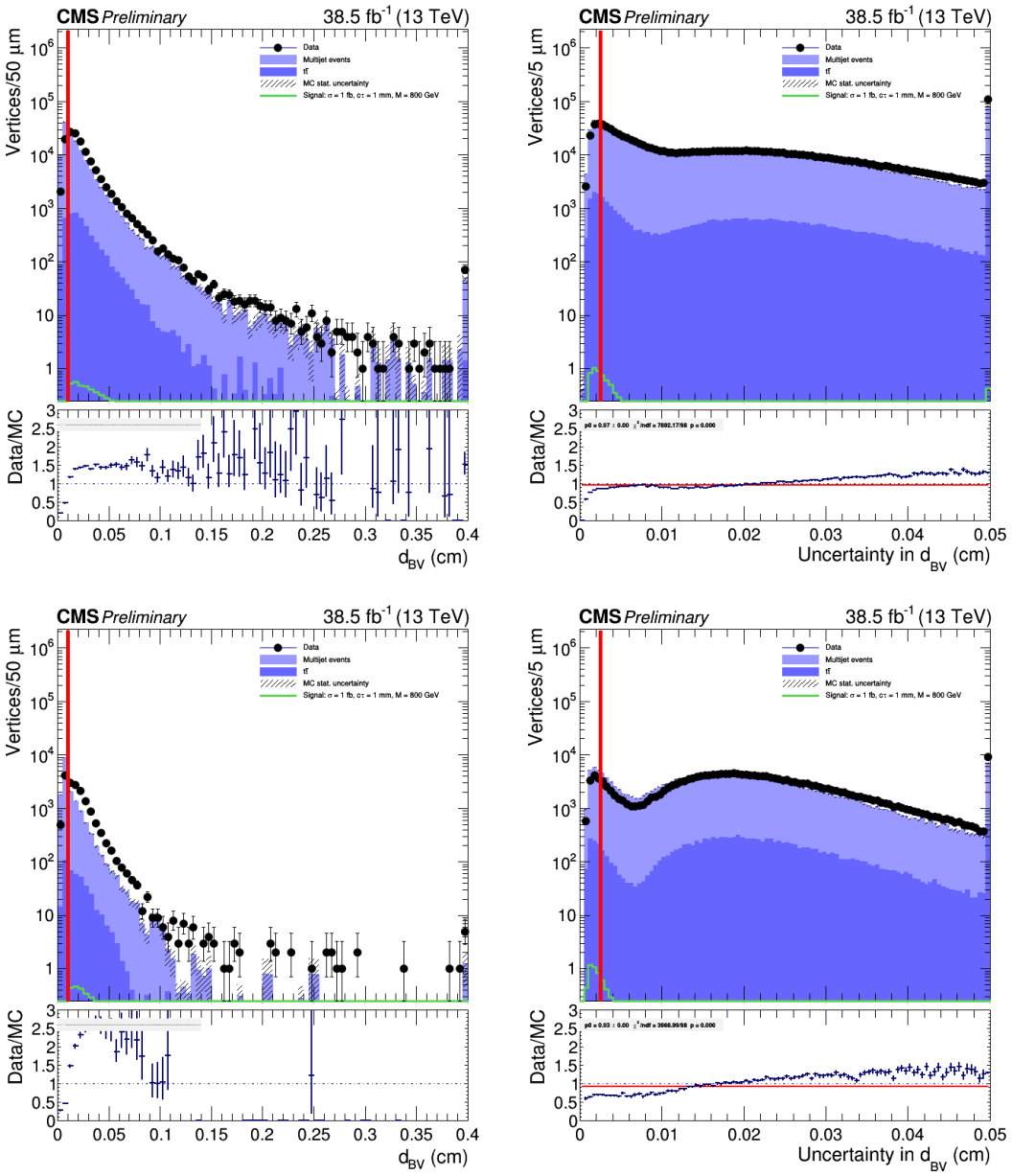

Figure 4.18: Distributions of the x-y distance of the vertex from the beam axis, d_{BV}, (left) and the uncertainty in d_{BV} (right) in 3-track (top) and 4-track (bottom) one-vertex events, for the full 2015+2016 dataset compared with simulated background normalized to data.

Table 4.6: MC yields for 5-or-more-track vertices, representing $38.5\,\text{fb}^{-1}$.

MC sample	one-vertex	two-vertex
QCD, $500 < H_\text{T} < 700\,\text{GeV}$	0	0
QCD, $700 < H_\text{T} < 1000\,\text{GeV}$	417 ± 49	0
QCD, $1000 < H_\text{T} < 1500\,\text{GeV}$	2299 ± 82	0
QCD, $1500 < H_\text{T} < 2000\,\text{GeV}$	581 ± 15	0
QCD, $H_\text{T} > 2000\,\text{GeV}$	208 ± 6	0
$\text{t}\bar{\text{t}}$	132 ± 10	0.7 ± 0.7
Total background	3637 ± 97	0.7 ± 0.7
Multijet signals: $\sigma = 1$ fb		
$c\tau = 100\,\mu\text{m}$, $M = 800\,\text{GeV}$	4.48 ± 0.04	0.46 ± 0.01
$c\tau = 300\,\mu\text{m}$, $M = 800\,\text{GeV}$	12.52 ± 0.07	4.07 ± 0.04
$c\tau = 1\,\text{mm}$, $M = 800\,\text{GeV}$	13.67 ± 0.07	13.64 ± 0.07
$c\tau = 10\,\text{mm}$, $M = 800\,\text{GeV}$	8.15 ± 0.06	24.64 ± 0.10

Table 4.7: MC yields for 3-track and 4-track vertices, representing $38.5\,\text{fb}^{-1}$.

	3-track		4-track × 3-track	4-track	
MC sample	one-vertex	two-vertex	two-vertex	one-vertex	two-vertex
QCD, $500 < H_\text{T} < 700\,\text{GeV}$	291 ± 72	0	0	2 ± 2	0
QCD, $700 < H_\text{T} < 1000\,\text{GeV}$	24232 ± 370	110 ± 25	33 ± 14	2955 ± 129	0
QCD, $1000 < H_\text{T} < 1500\,\text{GeV}$	119050 ± 589	577 ± 41	110 ± 18	14794 ± 208	3 ± 3
QCD, $1500 < H_\text{T} < 2000\,\text{GeV}$	22844 ± 92	136 ± 7	34 ± 4	3183 ± 34	2 ± 1
QCD, $H_\text{T} > 2000\,\text{GeV}$	6251 ± 31	45 ± 3	13 ± 1	988 ± 12	2 ± 1
$\text{t}\bar{\text{t}}$	8986 ± 79	123 ± 9	25 ± 4	1092 ± 27	1 ± 1
Total background	181654 ± 711	991 ± 49	213 ± 23	23015 ± 249	8 ± 3
Multijet signals: $\sigma = 1$ fb					
$c\tau = 100\,\mu\text{m}$, $M = 800\,\text{GeV}$	4.98 ± 0.04	0.51 ± 0.01	0.47 ± 0.01	2.47 ± 0.03	0.13 ± 0.01
$c\tau = 300\,\mu\text{m}$, $M = 800\,\text{GeV}$	6.98 ± 0.05	1.09 ± 0.02	1.22 ± 0.02	4.66 ± 0.04	0.46 ± 0.01
$c\tau = 1\,\text{mm}$, $M = 800\,\text{GeV}$	7.51 ± 0.05	1.32 ± 0.02	1.46 ± 0.02	5.42 ± 0.05	0.55 ± 0.01
$c\tau = 10\,\text{mm}$, $M = 800\,\text{GeV}$	5.93 ± 0.05	0.78 ± 0.02	0.86 ± 0.02	4.15 ± 0.04	0.33 ± 0.01

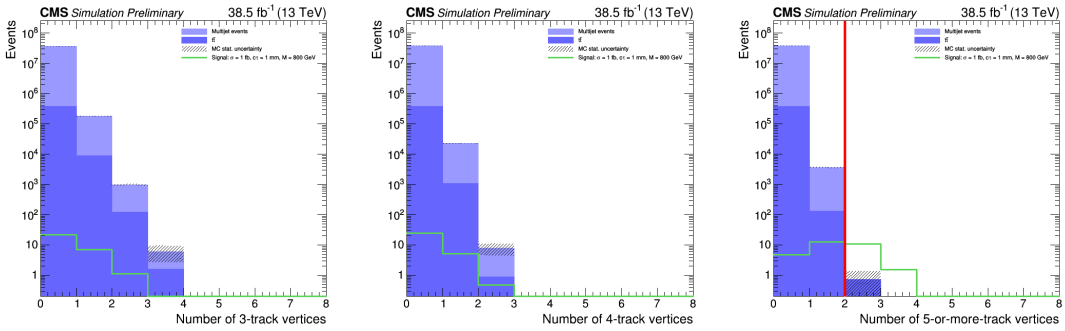

Figure 4.19: Distributions of number of 3-track (left), 4-track (middle), and 5-or-more-track (right) vertices. All event preselection and vertex selection criteria have been applied. The signal region is composed of 5-or-more-track two-vertex events.

4.3.4 Vertex position resolution

We study the vertex position resolution using simulated signal samples, by matching each reconstructed vertex to the closest generated LSP. Figure 4.20 shows the distribution of 3D distances from the vertex to the closest LSP. We want to find the value of 3D distance for which 95% of the vertices are within that distance to an LSP. The background is estimated using the density of events with 3D distance in the range 0.018–0.02 cm, and after subtracting the background we find that 95% of the vertices are within 84 μm of a generated LSP.

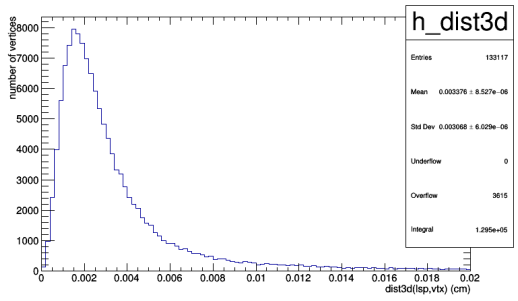

Figure 4.20: Distribution of the 3D distance between reconstructed vertices and the closest generated LSP, in simulated signal events.

4.4 Search strategy

The signal is discriminated from the SM background using the distance between the two vertices measured in the x-y plane, which is defined as d_{VV}. In signal events, the two long-lived particles are emitted approximately back-to-back, leading to large separations. If an event has more than two vertices, the two vertices with the highest number of tracks are selected for the d_{VV} calculation. In the case in which two vertices have the same number of tracks, the vertex with the higher mass is chosen, where the mass is reconstructed using the momenta of the tracks associated with the vertex, assuming that the particles associated with the tracks

have the mass of a charged pion.

We fit the distribution of d_{VV} to extract the signal, using templates to represent the d_{VV} distributions for signal and background. The free parameter in the fit is the relative normalization of the signal and background templates. The signal d_{VV} templates are taken directly from simulation, with a distinct template for each signal mass and lifetime. The background template is constructed from events in data that have exactly one vertex, as described in Section 4.5. Figure 4.21 shows examples of the d_{VV} distribution for simulated multijet signals with $M = 800\,\mathrm{GeV}$ and production cross section 1 fb, with the background template overlaid. The distributions depend primarily on the signal lifetime; those for other signal masses and for the dijet signals are similar. The small peaks at low values of d_{VV} are associated with events for which the two vertices are reconstructed from the same long-lived particle, with the effect being larger for the multijet signals.

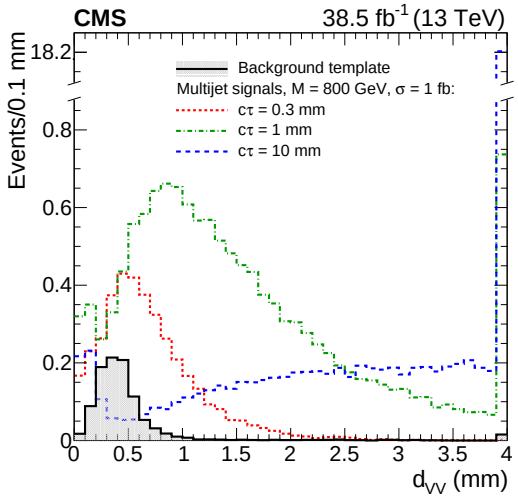

Figure 4.21: Distribution of the distance between vertices in the x-y plane, d_{VV}, for simulated multijet signals with $M = 800\,\mathrm{GeV}$, production cross section 1 fb, and $c\tau = 0.3$, 1, and 10 mm, with the background template overlaid. All vertex and event selection criteria have been applied. The last bin includes the overflow events.

Figure 4.22 shows the distributions of d_{VV} in 3-track, 4-track, and 5-or-more-

track two-vertex events.

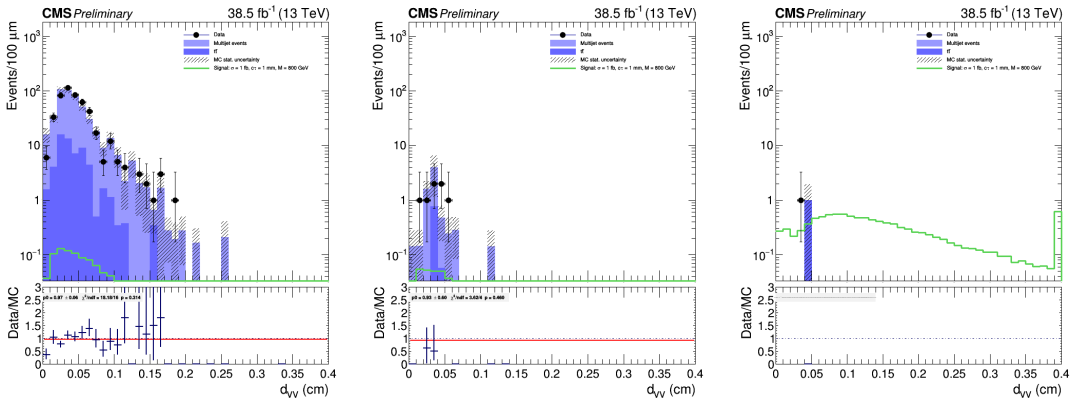

Figure 4.22: Distribution of the x-y distance between vertices, d_{VV}, in 3-track (left), 4-track (middle), and 5-or-more-track (right) two-vertex events, for the full 2015+2016 dataset compared with simulated background normalized to data.

In the signal extraction procedure, the d_{VV} distribution is broken into three bins: 0–0.4 mm, 0.4–0.7 mm, and 0.7–40 mm. The two bins with $d_{\mathrm{VV}} > 0.4$ mm have low background. This division maximizes the signal significance for scenarios with intermediate and long lifetimes.

Figure 4.23 shows the signal efficiency as a function of signal mass and lifetime in the region $d_{\mathrm{VV}} > 0.4$ mm. The signal efficiency increases with increasing mass because the events are more likely to satisfy the H_{T} trigger requirement. As lifetime increases, the signal efficiency initially increases because of better separation from the beam axis, but then starts to decrease when the lifetime is so long that decays occur more often beyond the fiducial limit at the beam pipe. The efficiency is above 10% for $c\tau > 0.4$ mm and $M > 800$ GeV.

4.5 Background template

Displaced vertices in background events arise from one or more misreconstructed tracks overlapping with other tracks. These events are dominated by multijet and

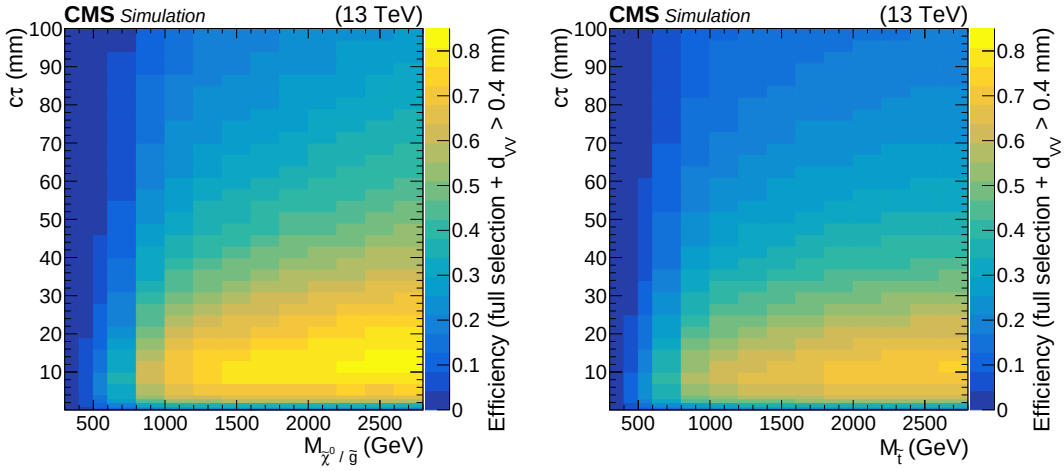

Figure 4.23: Signal efficiency as a function of signal mass and lifetime, for the multijet (left) and dijet (right) signal samples. All vertex and event selection criteria have been applied, as well as the requirement $d_{\mathrm{VV}} > 0.4\,\mathrm{mm}$.

$\mathrm{t\bar{t}}$ processes. Background events with two vertices are primarily random coincidences of independently misreconstructed vertices. Accordingly, we construct the two-vertex background template, denoted by $d_{\mathrm{VV}}^{\mathrm{C}}$, by combining information from events in data that have exactly one vertex. There are approximately 1000 times more events with only one vertex than there are with two or more vertices, consistently for 3-track, 4-track, and ≥5-track vertices. Table 4.8 lists the number of events in each of the event categories.

Table 4.8: Event yields in data. The "one-vertex" events have exactly one vertex with the specified number of tracks, and the "two-vertex" events have two or more vertices each with the specified number of tracks. The control samples are composed of the events with 3-track and 4-track vertices, the background template is constructed using the ≥5-track one-vertex events, and the signal region consists of the ≥5-track two-vertex events.

Event category	3-track	4-track × 3-track	4-track	≥5-track
one-vertex	109090	—	11923	1183
two-vertex	478	99	7	1

Each entry in the $d_{\mathrm{VV}}^{\mathrm{C}}$ template is calculated from two values of d_{BV} and a value of $\Delta\phi_{\mathrm{VV}}$, where d_{BV} is the distance measured in the x-y plane from the beam axis

to one vertex, and $\Delta\phi_{\mathrm{VV}}$ is the azimuthal angle between the two vertices. The template also includes corrections for the merging of nearby vertices in the vertex reconstruction algorithm and for possible correlations between individual vertices in background events with pairs of b quarks. Figure 4.24 shows the inputs to the $d_{\mathrm{VV}}^{\mathrm{C}}$ construction method, as well as the resulting $d_{\mathrm{VV}}^{\mathrm{C}}$ background template, in simulated events. The following subsections describe each of the inputs to the $d_{\mathrm{VV}}^{\mathrm{C}}$ template construction method, and the testing of closure of the method using control samples.

4.5.1 Distribution of vertex distances

The d_{BV} values are sampled from the distribution shown in Fig. 4.25 for the $\geq$5-track one-vertex events in data. The distribution starts at 0.1 mm because of the fiducial requirement to avoid primary vertices, and falls off exponentially. Signal contamination in the one-vertex sample is negligible for values of the signal cross section that have not been excluded by the previous similar analysis [16].

The statistical uncertainty in the $d_{\mathrm{VV}}^{\mathrm{C}}$ template, taken as the root-mean-square of yields in an ensemble of simulated pseudo-data sets, depends on the number of entries in the parent d_{BV} distribution. To ensure sufficient sampling of the tail of this distribution, the number of entries in the $d_{\mathrm{VV}}^{\mathrm{C}}$ template is 20 times the number of one-vertex events. Table 4.9 lists the statistical uncertainties in each $d_{\mathrm{VV}}^{\mathrm{C}}$ bin.

Table 4.9: Fractional statistical uncertainties in background yield in each $d_{\mathrm{VV}}^{\mathrm{C}}$ bin arising from the limited number of one-vertex events, for the full 2015+2016 dataset.

Control sample	0–400 μm	400–700 μm	700–40000 μm
3-track	0.003	0.003	0.008
4-track	0.009	0.010	0.031
5-or-more-track	0.021	0.054	0.175

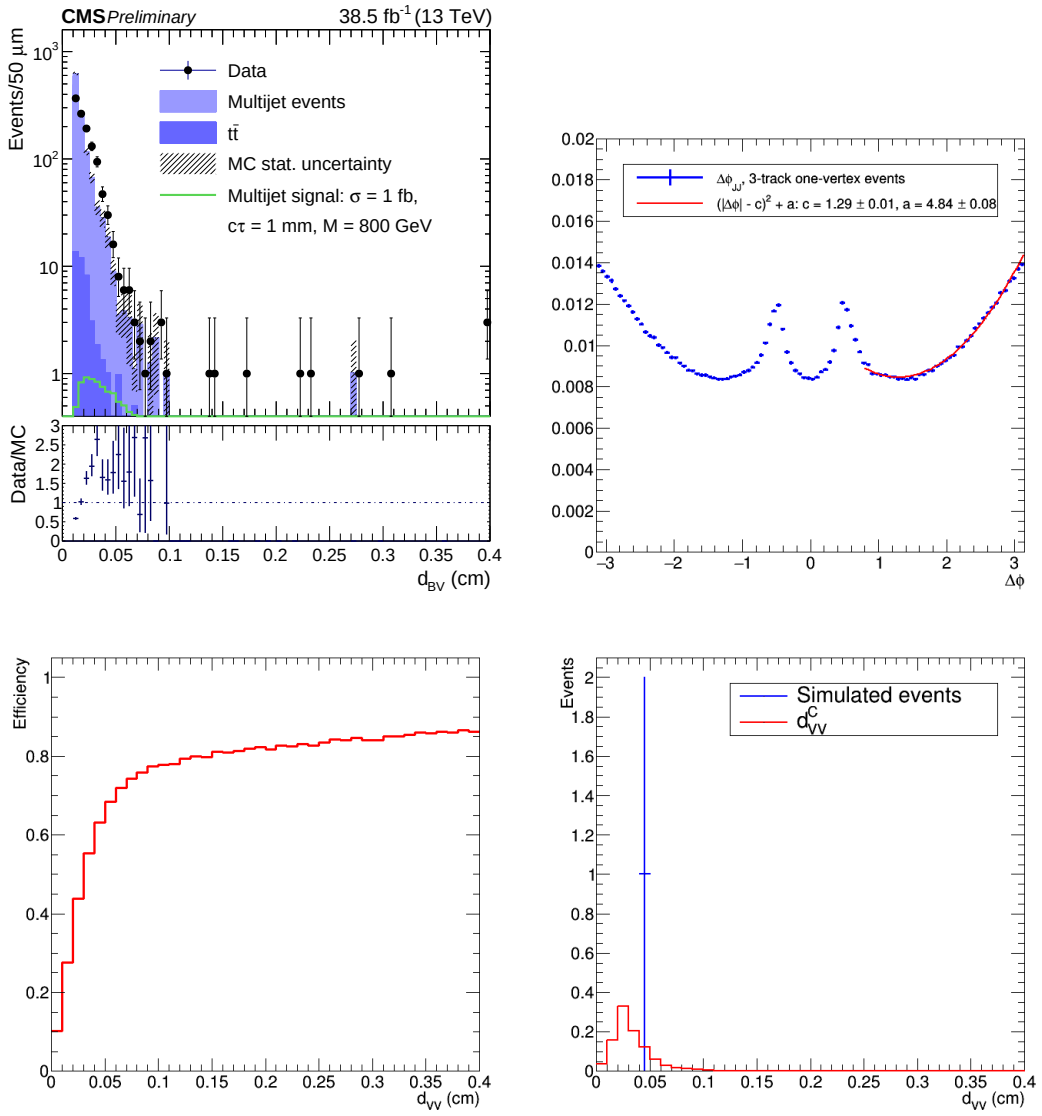

Figure 4.24: Distributions of the inputs and output of the $d_{\mathrm{VV}}^{\mathrm{C}}$ background template construction method. (Top left) 5-or-more-track one-vertex events: distribution of the x-y distance from the beam axis to the vertex, d_{BV}, for data, simulated background normalized to data, and a simulated multijet signal with $c\tau = 1\,\mathrm{mm}$, $M = 800\,\mathrm{GeV}$, and production cross section 1 fb. Event preselection and vertex selection criteria have been applied. The last bin includes the overflow events. (Top right) Distribution of $\Delta\phi$ between pairs of jets in 3-track one-vertex events, for the full 2015+2016 dataset. (Bottom left) Efficiency to keep pairs of vertices as a function of d_{VV}, for the full 2015+2016 dataset. (Bottom right) Background template, $d_{\mathrm{VV}}^{\mathrm{C}}$, constructed from simulated one-vertex events.

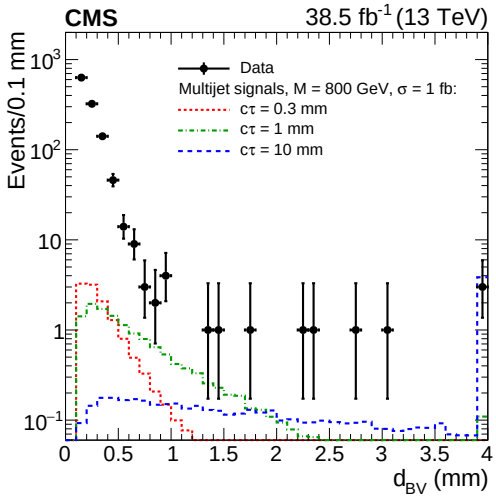

Figure 4.25: Distribution of d_{BV} in $\geq$5-track one-vertex events for data and simulated multijet signals with $M = 800\,\mathrm{GeV}$, production cross section 1 fb, and $c\tau =$ 0.3, 1, and 10 mm. Event preselection and vertex selection criteria have been applied. The last bin includes the overflow events.

4.5.2 Distribution of the angle between vertices

Values of $\Delta\phi_{\mathrm{VV}}$ are approximated by sampling the distribution of jets in data. Since background vertices arise from misreconstructed tracks in jets, their position vectors tend to be correlated with jet momentum vectors. The angle between vertex positions can therefore be modeled using the observed distribution of azimuthal angles between pairs of jets, denoted as $\Delta\phi_{\mathrm{JJ}}$. The $\Delta\phi_{\mathrm{JJ}}$ distribution used for the $d_{\mathrm{VV}}^{\mathrm{C}}$ construction is taken from the 3-track one-vertex sample, which has a greater number of events than the 4-track and $\geq$5-track one-vertex samples. There are no significant differences in the $\Delta\phi_{\mathrm{JJ}}$ distribution among these three samples.

Figure 4.26 shows, for simulated events, the distribution of $\Delta\phi_{\mathrm{JV}}$, the angle between jets and the vertex in one-vertex events, showing that the vertex position vectors are correlated with jet momentum vectors, and the distribution of $\Delta\phi_{\mathrm{JJ}}$, the angle between pairs of jets in one-vertex events, showing that the distributions are similar among the 3-track, 4-track, and 5-or-more-track samples. To obtain a

value of $\Delta\phi_{\mathrm{VV}}$, we fit the distribution of 3-track $\Delta\phi_{\mathrm{JJ}}$ to a parabola, starting the fit at $\Delta\phi_{\mathrm{JJ}} = 0.8$ to avoid the region where $\Delta\phi_{\mathrm{JJ}}$ is suppressed due to the jet cone size, and draw a value from the fitted function.

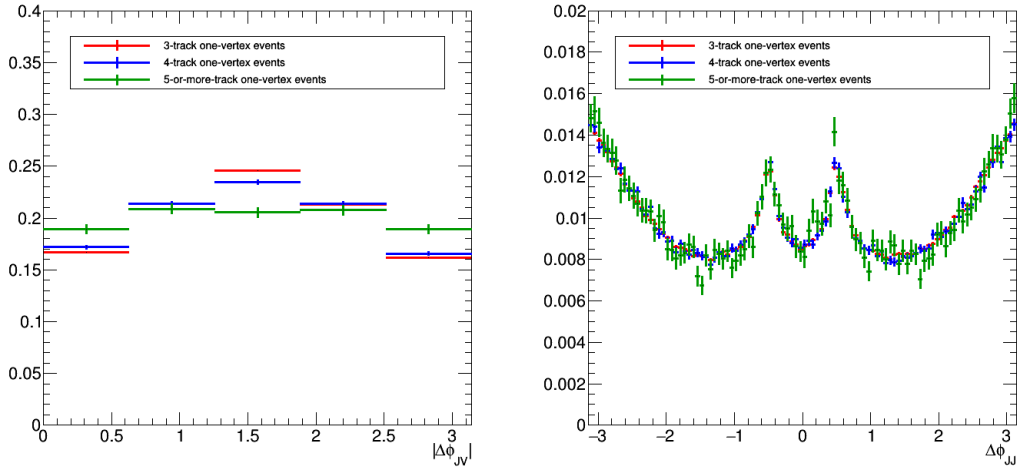

Figure 4.26: Distributions of $\Delta\phi$ in simulated 3-track, 4-track, and 5-or-more-track one-vertex events. (Left) $\Delta\phi$ between jets and the vertex. (Right) $\Delta\phi$ between pairs of jets.

Figure 4.27 compares the distributions of $\Delta\phi_{\mathrm{VV}}$ in simulated two-vertex events and constructed from simulated one-vertex events.

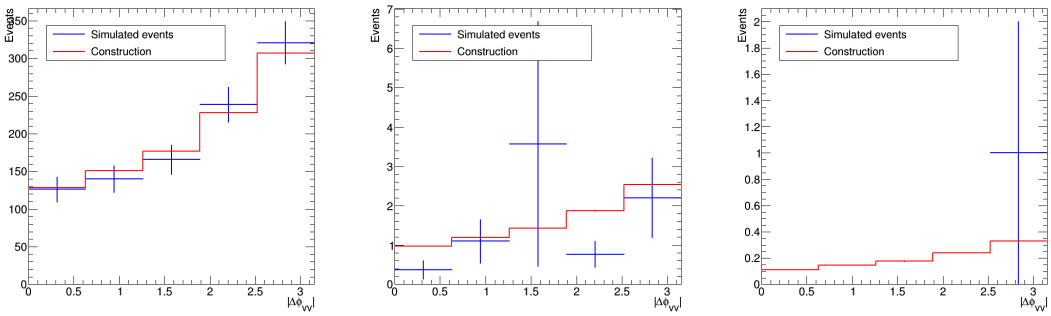

Figure 4.27: Distribution of the angle between vertices, $\Delta\phi_{\mathrm{VV}}$, for simulated two-vertex background events, overlaid on the distribution constructed from simulated one-vertex events, for 3-track (left), 4-track (middle), and 5-or-more-track (right) vertices.

4.5.3 Merging overlapping vertices

To emulate the behavior of the vertex reconstruction algorithm in merging overlapping vertices, the $d_{\mathrm{VV}}^{\mathrm{C}}$ template is corrected by the survival probability of pairs of vertices as a function of d_{VV}. This efficiency is estimated by counting the number of remaining vertex pairs at each iteration of the vertex reconstruction algorithm. The efficiency correction suppresses small $d_{\mathrm{VV}}^{\mathrm{C}}$ values, resulting in a yield in the first $d_{\mathrm{VV}}^{\mathrm{C}}$ bin that is lower by a factor of approximately 2.

We estimate the efficiency separately for 3-track, 4-track, and 5-or-more-track vertices, characterizing each vertex pair by the maximum of the number of tracks in the two vertices. The resulting efficiency curves are similar for the three samples, so we choose to use the 3-track efficiency because it has the most statistics.

Figure 4.28 compares the efficiencies for 3-track, 4-track, and 5-or-more-track vertices, and shows the effect of the efficiency correction on the constructed $d_{\mathrm{VV}}^{\mathrm{C}}$ background template.

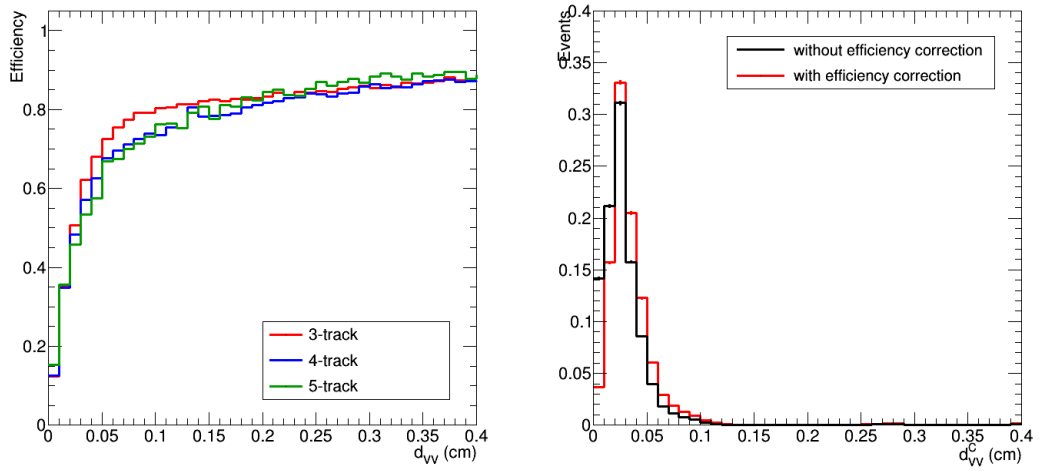

Figure 4.28: (Left) Distributions of the efficiency to keep pairs of vertices as a function of d_{VV}, for 3-track, 4-track, and 5-or-more-track vertices. (Right) Background template, $d_{\mathrm{VV}}^{\mathrm{C}}$, with and without the efficiency correction.

4.5.4 Correlations between vertex distances: b quarks

Pair production of b quarks introduces d_{BV} correlations in two-vertex events that are not accounted for when pairing single vertices at random. This is because the tracks from b quark decays are more likely to satisfy the track $|d_{xy}|/\sigma_{d_{xy}}$ requirement and therefore produce vertices. Figure 4.29 compares the distributions of d_{BV} in one-vertex events with and without b quarks. In simulation, the mean d_{BV} in events with b quarks is higher than in events without b quarks by $47 \pm 1\,\mu$m for 3-track vertices, by $52 \pm 3\,\mu$m for 4-track vertices, and by $50 \pm 6\,\mu$m for $\geq$5-track vertices. The fractions of events with b quarks are consistent across the 3-track, 4-track, and $\geq$5-track vertex samples: approximately 50% in one-vertex events and approximately 78% in two-vertex events.

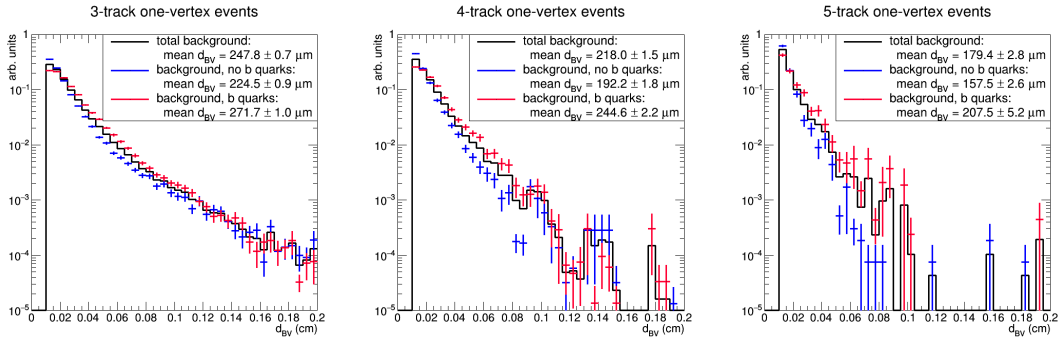

Figure 4.29: Distributions of the x-y distance from the beam axis to the vertex, d_{BV}, in one-vertex events with and without b quarks.

We determine corrections to the $d_{\mathrm{VV}}^{\mathrm{C}}$ template for these d_{BV} correlations by constructing $d_{\mathrm{VV}}^{\mathrm{C}}$ separately for simulated background events with and without generated b quarks, combining the distributions in the ratio of two-vertex events with and without b quarks, and then dividing the resulting distribution by the nominal $d_{\mathrm{VV}}^{\mathrm{C}}$ template. Figure 4.30 compares the $d_{\mathrm{VV}}^{\mathrm{C}}$ distributions obtained with and without this procedure, and shows the ratios of simulated yields in each $d_{\mathrm{VV}}^{\mathrm{C}}$ bin. The b quark correction enhances larger $d_{\mathrm{VV}}^{\mathrm{C}}$ values, resulting in a yield in the

last $d_{\mathrm{VV}}^{\mathrm{C}}$ bin that is higher by a factor of 1.6 ± 0.4.

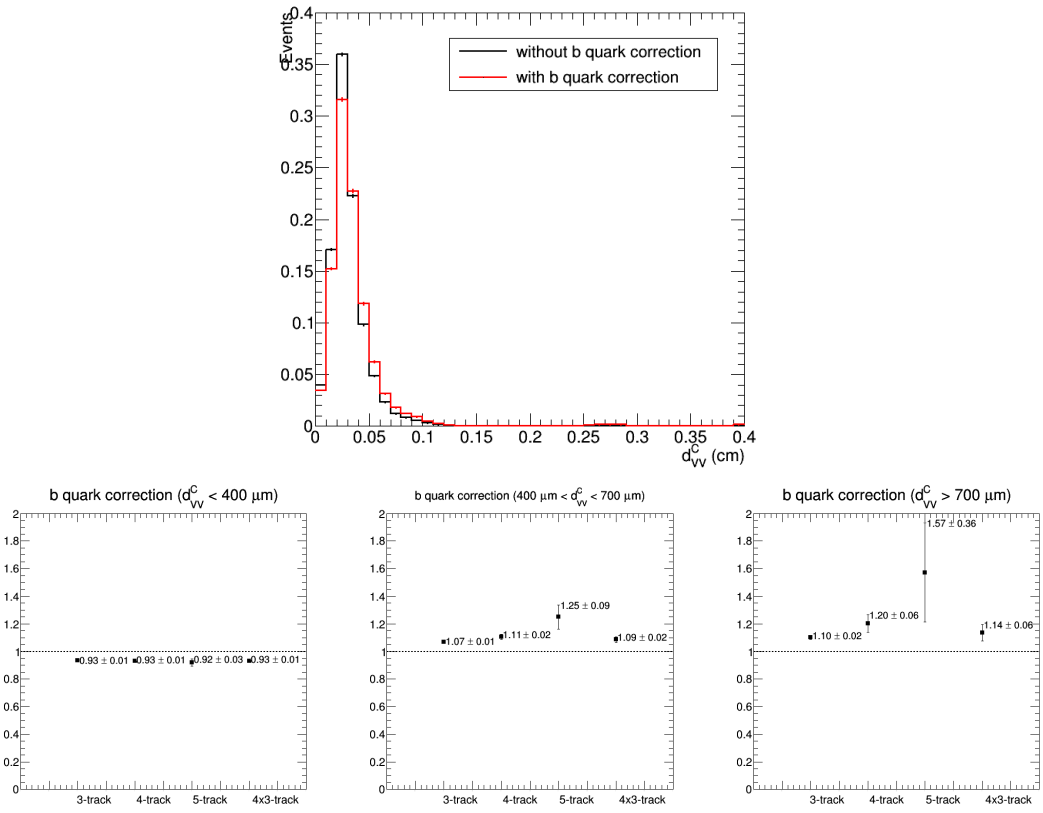

Figure 4.30: (Top) Background template, $d_{\mathrm{VV}}^{\mathrm{C}}$, constructed with and without the b quark correction procedure. (Bottom left) Background template correction in the $d_{\mathrm{VV}}^{\mathrm{C}} < 400\,\mu$m bin. (Bottom middle) Background template correction in the $400 < d_{\mathrm{VV}}^{\mathrm{C}} < 700\,\mu$m bin. (Bottom right) Background template correction in the $d_{\mathrm{VV}}^{\mathrm{C}} > 700\,\mu$m bin.

4.5.5 Testing closure

Evidence that the background template construction method is valid is presented in the upper left, upper right, and lower left plots in Fig. 4.31, where $d_{\mathrm{VV}}^{\mathrm{C}}$ is compared to the observed two-vertex d_{VV} distributions in the low-track-multiplicity control samples in data. There is good agreement between the relative $d_{\mathrm{VV}}^{\mathrm{C}}$ and d_{VV} populations in each of the three bins of the final fit. For example, in the 3-track

control sample, where this agreement is most stringently tested, the ratios $d_{\rm VV}^{\rm C}/d_{\rm VV}$ are 0.93±0.06 in the 0–0.4 mm bin, 0.97±0.07 in the 0.4–0.7 mm bin, and 1.44±0.20 in the 0.7–40 mm bin.

The background template for the signal region is shown in the lower right plot in Fig. 4.31.

Table 4.10 gives the background prediction in each $d_{\rm VV}^{\rm C}$ bin, and Table 4.11 gives the ratios of the background yields predicted using the one-vertex events and from the two-vertex events, for each of the control samples.

Table 4.10: MC background template: predicted fraction of events in each $d_{\rm VV}^{\rm C}$ bin.

MC sample	0–400 μm	400–700 μm	700–40000 μm
3-track × 3-track	0.508 ± 0.001	0.351 ± 0.001	0.140 ± 0.001
4-track × 3-track	0.549 ± 0.003	0.337 ± 0.003	0.114 ± 0.003
4-track × 4-track	0.597 ± 0.004	0.317 ± 0.002	0.086 ± 0.002
5-track × 5-track	0.730 ± 0.009	0.212 ± 0.007	0.058 ± 0.006

Table 4.11: MC closure in control samples, given by the ratio of the background yields predicted using the one-vertex events and from the two-vertex events.

Control sample	0–400 μm	400–700 μm	700–40000 μm
3-track × 3-track	0.97 ± 0.06	1.04 ± 0.09	1.04 ± 0.14
4-track × 3-track	1.07 ± 0.16	0.92 ± 0.16	0.95 ± 0.28
4-track × 4-track	0.71 ± 0.35	2.22 ± 0.95	3.88 ± 3.57

4.5.6 Potential signal contamination

The signal contamination in the 3-track and 4-track control samples (Table 4.7) as well as in the 5-or-more-track one-vertex sample (Table 4.6, Figure 4.25) is expected to be small. To check whether potential signal contamination would affect the background prediction, we injected signal into the simulated one-vertex background events and then constructed $d_{\rm VV}^{\rm C}$. Figure 4.32 compares the constructed $d_{\rm VV}^{\rm C}$ distributions with and without signal injected. In the bin with $d_{\rm VV}^{\rm C} > 700\,\mu$m,

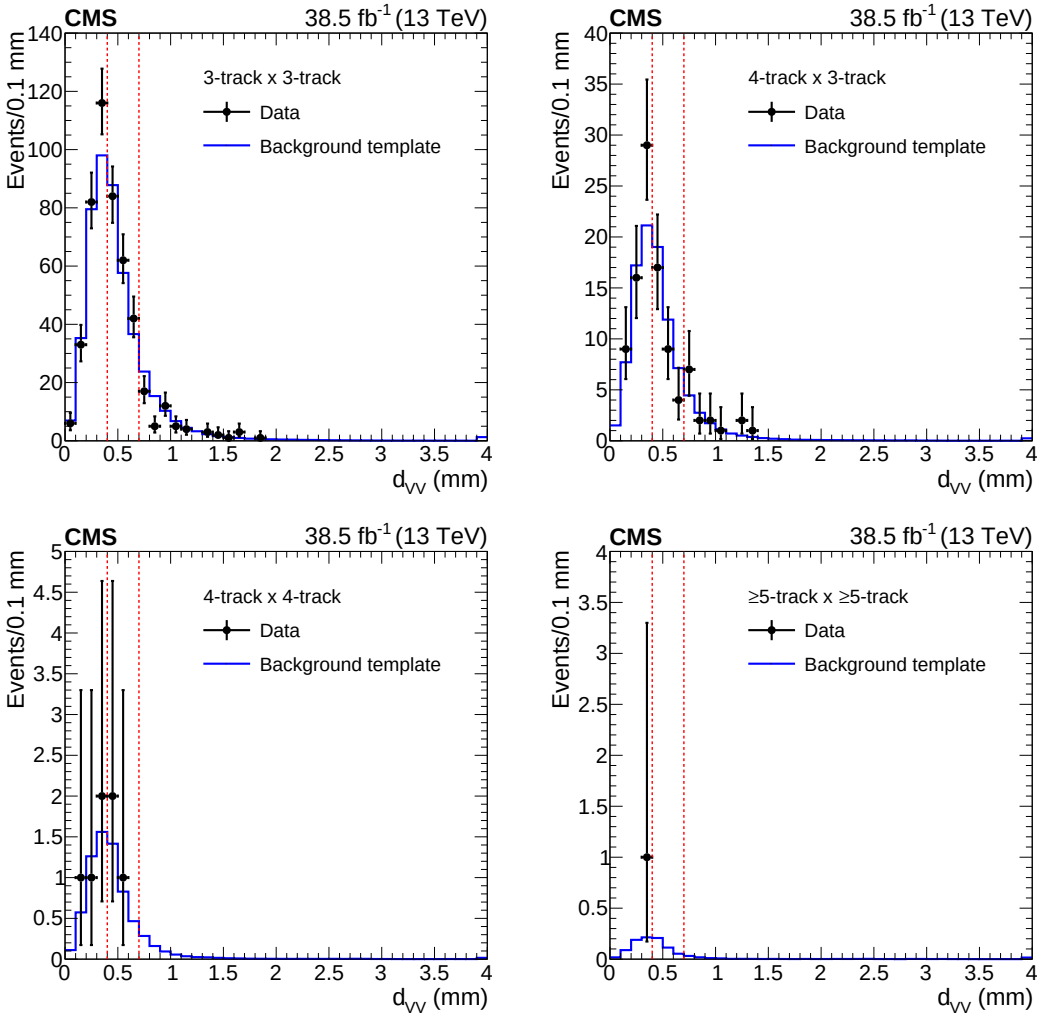

Figure 4.31: Distribution of the distance between vertices in the x-y plane in two-vertex events. The points show the data (d_{VV}), and the solid lines show the background template ($d_{\mathrm{VV}}^{\mathrm{C}}$) normalized to the data, for events with two 3-track vertices (upper left), one 4-track vertex and one 3-track vertex (upper right), two 4-track vertices (lower left), and two $\geq$5-track vertices (lower right). In each plot, the last bin includes the overflow events. The dotted lines indicate the boundaries between the three bins used in the fit.

the size of the change in predicted yield is comparable to the size of the statistical uncertainty: without injected signal, the predicted fraction of events is 0.058 ± 0.006; with a 1 fb 1 mm 800 GeV signal, it is 0.066 ± 0.007; with a 1 fb 10 mm 800 GeV signal it is 0.070 ± 0.007; with a 3 fb 10 mm 300 GeV signal it is 0.064 ± 0.001. This shows that the signal contamination is negligible.

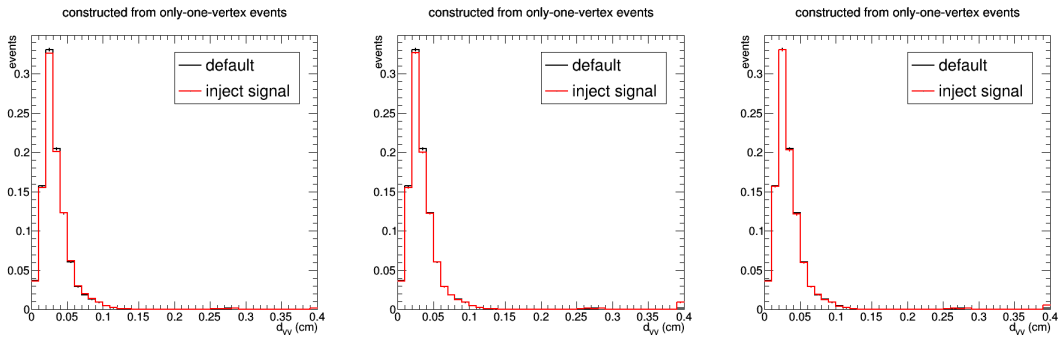

Figure 4.32: Background template, $d_{\mathrm{VV}}^{\mathrm{C}}$, constructed from simulated 5-or-more-track one-vertex background events, with and without signal injected. The injected signals are multijet signal samples with $c\tau = 1\,\mathrm{mm}$, $M = 800\,\mathrm{GeV}$, and production cross section 1 fb (left), $c\tau = 10\,\mathrm{mm}$, $M = 800\,\mathrm{GeV}$, and production cross section 1 fb (middle), and $c\tau = 10\,\mathrm{mm}$, $M = 300\,\mathrm{GeV}$, and production cross section 3 fb (right).

4.6 Systematic uncertainties

The signal yield is extracted from a fit of the signal and background templates to the observed d_{VV} distribution. The free parameters are the normalizations of the signal and background templates, subject to the constraint that their combined yield matches the data. The result of the fit relies on the relative yields in the three bins of the templates, but is insensitive to the fine details of the template distributions. This section describes the systematic uncertainties in the background template. It also addresses the systematic uncertainties in the signal efficiencies and templates.

4.6.1 Systematic uncertainties in signal efficiencies and templates

The signal d_{VV} templates are taken directly from simulation of benchmark models with clearly specified parameters, so the systematic uncertainties arise from biases in the detector simulation and reconstruction. The dominant source of uncertainty is due to the vertex reconstruction efficiency. Smaller effects arise from track resolution, pileup, jet energy scale and resolution, integrated luminosity, and trigger efficiency.

Vertex reconstruction

The effect due to the vertex reconstruction efficiency is evaluated by comparing the efficiency in data and simulation to reconstruct signal-like vertices created by displacing tracks artificially. In events passing the preselection requirements (Section 4.2), we choose some number of light parton and b quark jets that have $p_{\mathrm{T}} > 50\,\mathrm{GeV}$, $|\eta| < 2.5$, and at least four particle-flow candidates. We then artificially displace the tracks associated with those jets as described below.

The magnitude of the displacement vector is sampled from an exponential distribution with scale parameter $c\tau = 10\,\mathrm{mm}$, restricted to values between 0.3 and 20 mm. The direction of the displacement vector is calculated from the vector sum of the momentum of the jets. This direction is smeared to emulate the difference between the vertex displacement direction and jet momentum direction in signal events due to mismeasurements from tracking inefficiency and missing neutral particles.

The track selection requirements (Sec. 4.3.1) and vertex reconstruction algorithm (Sec. 4.3.2) are applied to the resulting set of tracks. We then evaluate the fraction of events in which a vertex satisfying all vertex selection requirements

(Sec. 4.3.3) is reconstructed within 84 μm of the artificial displacement position. (This is the value found in the vertex position resolution study (Sec. 4.3.4) that contains 95% of the vertices reconstructed in signal events.) This fraction is evaluated for different numbers of displaced light parton or b quark jets. Table 4.12 compares the resulting efficiencies between data and background simulation, for the various combinations of (n_l, n_b) and various sets of vertex selection requirements. The efficiency is generally higher in the simulation, by less than 10% for all configurations studied. The largest disagreement between data and simulation gives an 11.5% uncertainty per vertex. For two-vertex events, the uncertainty is 23%. Varying the scale parameter of the exponential distribution or the amount that the direction is smeared within reasonable values has negligible effect on the difference between data and simulation.

The difference in vertex reconstruction efficiency between data and simulation could also depend on the magnitude of the artificial displacement. This dependence is small, and the resulting difference in the signal d_{VV} templates has a negligible effect on the signal yield extracted from the fit (Sec. 4.7).

Figure 4.33 shows the efficiencies as functions of variables relevant to the artificial vertex or the overall event for $n_l = 2$ and $n_b = 1$, with some variation as a function of the event and vertex variables. The relative trends between data and simulation in these variables are the same when varying n_l to 3 and $n_b = 0, 1, 2$, with the overall difference in data and simulation decreasing toward 2% for higher numbers of jets.

Figure 4.34 shows the distributions of vertex track multiplicity, reconstructed displacement d_{BV}, and the related uncertainty for vertices in artificially displaced events in data and simulated background. The mean vertex track multiplicity is lower in data due to lost tracks, and the uncertainty in d_{BV} is larger in the data,

Table 4.12: Comparison of overall efficiencies obtained for artificially displaced vertices between the data and simulation for various combinations of numbers of jets moved and vertex quality cut requirements.

$n_l = 2$, $n_b = 0$			
Quality cuts	Eff. in data	Eff. in sim.	Relative difference
All	0.6273 ± 0.0001	0.7088 ± 0.0001	0.1150 ± 0.0002
None	0.8420 ± 0.0001	0.8868 ± 0.0001	0.0505 ± 0.0002
# tracks ≥ 5	0.8101 ± 0.0001	0.8651 ± 0.0001	0.0636 ± 0.0002
$n_l = 2$, $n_b = 1$			
Quality cuts	Eff. in data	Eff. in sim.	Relative difference
All	0.8044 ± 0.0003	0.8587 ± 0.0002	0.0632 ± 0.0004
None	0.8989 ± 0.0002	0.9282 ± 0.0002	0.0316 ± 0.0003
# tracks ≥ 5	0.8795 ± 0.0002	0.9137 ± 0.0002	0.0374 ± 0.0003
$n_l = 2$, $n_b = 2$			
Quality cuts	Eff. in data	Eff. in sim.	Relative difference
All	0.8584 ± 0.0008	0.8949 ± 0.0008	0.0408 ± 0.0012
None	0.9174 ± 0.0006	0.9364 ± 0.0006	0.0203 ± 0.0009
# tracks ≥ 5	0.9011 ± 0.0007	0.9222 ± 0.0007	0.0229 ± 0.0011
$n_l = 3$, $n_b = 0$			
Quality cuts	Eff. in data	Eff. in sim.	Relative difference
All	0.9071 ± 0.0001	0.9433 ± 0.0001	0.0384 ± 0.0001
None	0.9608 ± 0.0001	0.9764 ± 0.0001	0.0160 ± 0.0001
# tracks ≥ 5	0.9521 ± 0.0001	0.9709 ± 0.0001	0.0194 ± 0.0001
$n_l = 3$, $n_b = 1$			
Quality cuts	Eff. in data	Eff. in sim.	Relative difference
All	0.9386 ± 0.0002	0.9630 ± 0.0002	0.0253 ± 0.0003
None	0.9644 ± 0.0002	0.9779 ± 0.0001	0.0138 ± 0.0002
# tracks ≥ 5	0.9576 ± 0.0002	0.9735 ± 0.0002	0.0163 ± 0.0003
$n_l = 3$, $n_b = 2$			
Quality cuts	Eff. in data	Eff. in sim.	Relative difference
All	0.9468 ± 0.0007	0.9659 ± 0.0007	0.0198 ± 0.0010
None	0.9658 ± 0.0006	0.9786 ± 0.0005	0.0131 ± 0.0008
# tracks ≥ 5	0.9589 ± 0.0006	0.9733 ± 0.0006	0.0148 ± 0.0009

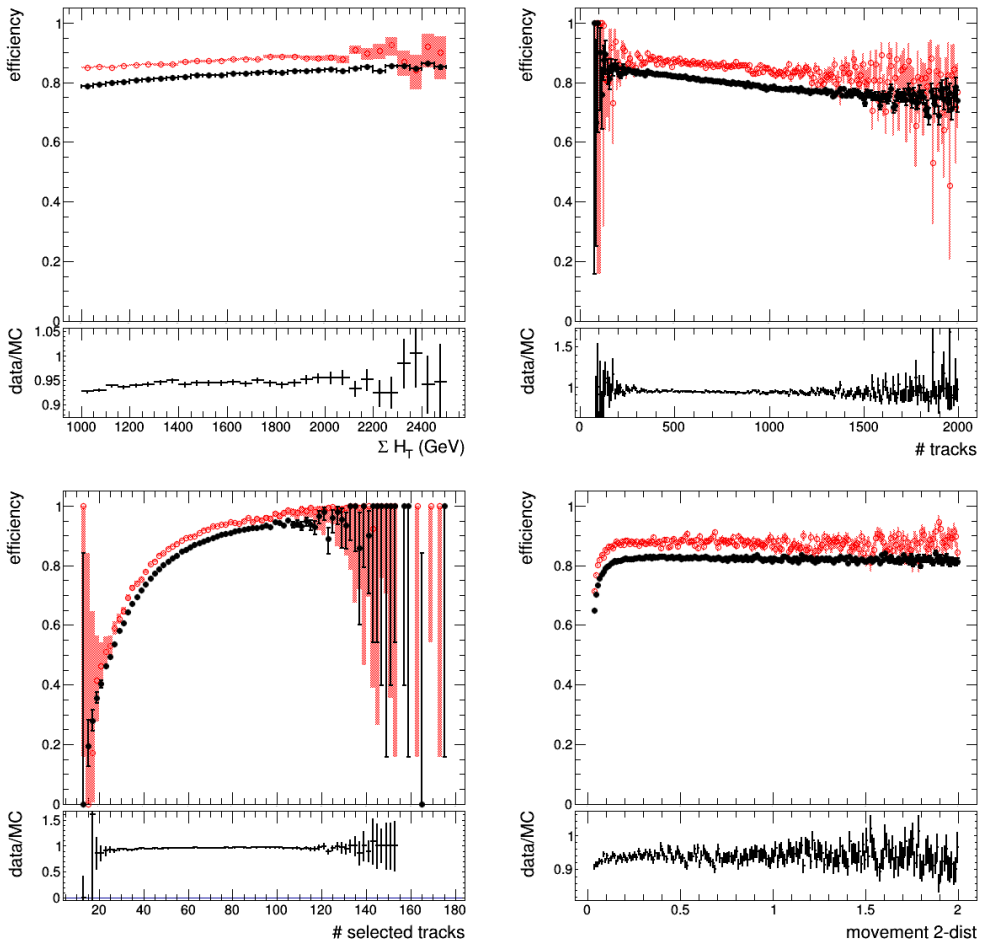

Figure 4.33: For the case where tracks from two light jets and one b-tagged jet are used, efficiencies obtained for artificially displaced vertices in the data (closed black circles) and simulation (open red circles) as a function of analysis-relevant variables: the H_{T} of jets in the event (middle left); the total number of tracks in the event (middle right); the selected number of tracks displaced to the artificial vertex (bottom left); the artificial flight distance in the transverse plane (bottom right).

reflecting tracks with worse position resolution due to fewer hits. Both of these effects separately worsen the vertex selection efficiency.

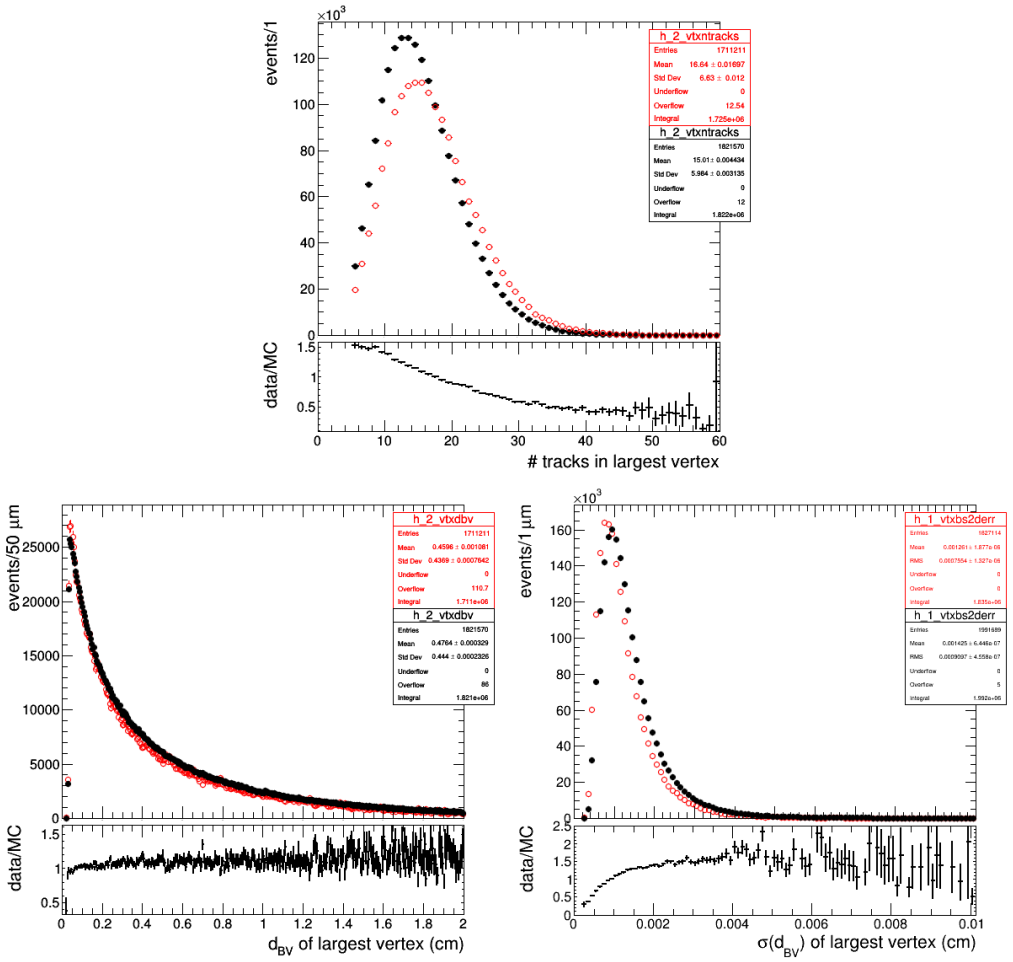

Figure 4.34: For the case where tracks from two light jets and one b-tagged jet are used, the reconstructed vertex track multiplicity (top), x-y distance to the beamspot and related uncertainty (bottom left and right) in the data (closed black circles) and background simulation (open red circles).

The true efficiency of finding a reconstructed vertex within 84 μm of a generated vertex in simulated signal events with mean proper decay length 10 mm is shown in Fig. 4.35, with the efficiency values from the artificial study overlaid. The range in the efficiency for the different numbers of jets (n_l, n_b) studied span the true efficiency values, which is reasonable since the different decay topologies and

masses are better represented by different event configurations.

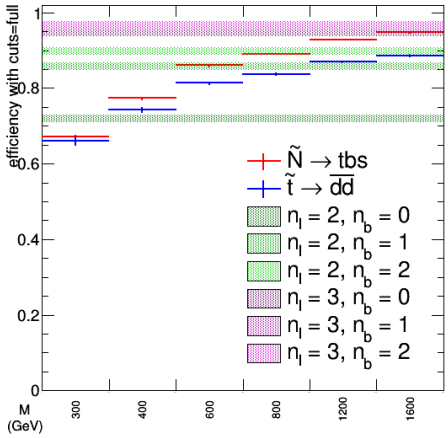

Figure 4.35: The single vertex efficiency in simulated signal events, for multijet (red crosses) and dijet (blue crosses) topologies, for mean proper decay length of 10 mm and different mass points. Overlaid in the green and magenta shaded bands spanning are vertex efficiencies measured using artificially displaced tracks from different numbers of light and b-tagged jets in the background simulation.

For a set of events with fixed n_l and n_b, if the vertex reconstruction efficiency had zero dependence on track/b-jet p_{T} and η, b-tagging scale factors would enter the numerator and denominator in the same way and cancel. To be sure, we explicitly checked what happens when using the scale factors to derive weights in MC events, and found that the MC artificial vertexing efficiency moves down by no more than 1% for most combinations of n_l, n_b, and artificial lifetimes, and at most 1.5% for short lifetimes when $n_b = 2$. The case with the largest difference between data and MC that we use to assign the systematic uncertainty, $n_l = 2$ and $n_b = 0$, has almost zero change when applying the b-tagging scale factors, since in this case we are only vetoing b-tags.

Track resolution

The selection of the tracks used in the vertex reconstruction requires that each track has a value of $|d_{xy}|/\sigma_{d_{xy}}$ of at least 4. The efficiency of this requirement is sensitive to the impact parameter resolution of the tracks. Figure 4.36 compares the distributions of track $\sigma_{d_{xy}}$ in data, simulated background, and an example simulated signal, and shows the means of the distributions for simulated background and for each data-taking era. The distributions are similar between data and simulated background, and also generally similar for signal, allowing the differences between data and simulated background to be applicable to the uncertainty in signal efficiency. The mean impact parameter uncertainty is 2% larger in data than in simulation.

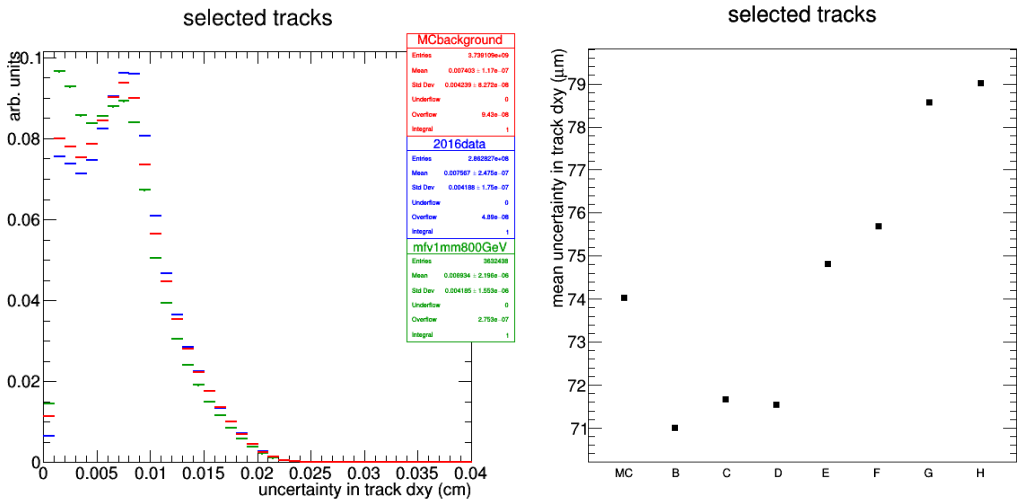

Figure 4.36: (Left) Distribution of the uncertainty in track impact parameter, for simulated background, data, and a simulated multijet signal with LSP $c\tau = 1\,\text{mm}$, $M = 800\,\text{GeV}$. All event preselection and track selection criteria have been applied, except for the cut on transverse impact parameter significance. (Right) Mean uncertainty in track impact parameter, for the 2016 MC background and each of the 2016 data-taking eras.

The magnitude of this effect is quantified by tightening the requirement on the transverse impact parameter significance by 2% and evaluating the change in the

signal efficiency. In assessing this effect, we additionally require that each vertex satisfies $d_{\mathrm{BV}} > 300\,\mu\mathrm{m}$, to be more relevant to the region with $d_{\mathrm{VV}} > 700\,\mu\mathrm{m}$. For the $100\,\mu\mathrm{m}$ signal samples with low efficiencies, we combine the statistics from several mass points to reduce the statistical uncertainty in the effect. Figure 4.37 shows the resulting effect on the signal efficiency as a function of signal mass and lifetime. The maximum effect on the various signal masses and lifetimes, 5%, is taken to be the systematic uncertainty in the signal efficiency. This effect is corrected for in the vertex resolution study discussed earlier.

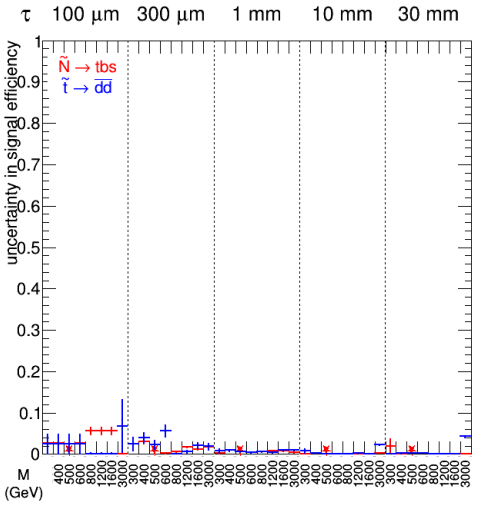

Figure 4.37: Fractional change in signal efficiency due to a variation in the transverse impact parameter significance cut, as a function of signal mass and lifetime.

Displaced tracking efficiency with the HIP effect

As described in Sec. 4.1, in the data from 2015 and 2016 eras B–F there was a dynamic inefficiency in the strip tracker known as the "HIP effect" that scaled with instantaneous luminosity. To study its effect, we generated signal samples with the HIP simulation developed by the tracker DPG turned on, as well as with the HIP mitigation as in the data re-reco turned on. The loss in signal efficiency is not too large: at most ∼10% in any sample with lifetime up to 30 mm. The

signal shape is unaffected as long as the mitigation is turned on. Figure 4.38 shows the distribution of d_{VV} for the simulated signal with LSP $c\tau = 1\,\mathrm{mm}$ and $M = 800\,\mathrm{GeV}$, for the nominal simulation, with the HIP simulation, and with the HIP simulation+mitigation.

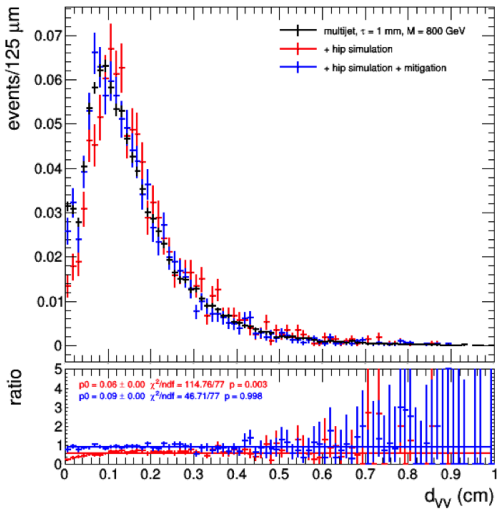

Figure 4.38: Distribution of the x-y distance between vertices, d_{VV}, for a simulated signal with LSP $c\tau = 1\,\mathrm{mm}$ and $M = 800\,\mathrm{GeV}$, for the nominal simulation, with the HIP simulation, and with the HIP simulation+mitigation.

With mitigation enabled, as was done in the 2016 re-reco datasets, there is no observed difference in the d_{VV} shape for any lifetime, and therefore we need to check only the fidelity of the HIP simulation with regard to the signal efficiency. We can then take the signal d_{VV} templates from a luminosity-weighted average of the nominal signal samples and the signal samples with HIP simulation+mitigation. To verify that the simulation of the HIP effect is accurate for displaced tracks, we study tracks from K_S^0 candidates.

K_S^0 candidates are identified by examining the invariant mass of all pairs of tracks that pass our track selection requirements. We vertex all oppositely-charged pairs of selected tracks, requiring $\chi^2/\mathrm{dof} < 5$. The post-fit candidate invariant mass is shown in Figure 4.39. K_S^0 candidates are taken from a mass window

around the nominal K^0_S mass (490–505 MeV), while low-mass (420–460 MeV) and high-mass (540–600 MeV) sidebands are used to estimate the background. In the on-peak mass window, there are 572387 candidates in the 2016 dataset, 80334 (14%) of which are estimated to be background. Figure 4.40 shows the distribution of the vertex distances d_{BV} for the K^0_S candidates, before and after background subtraction.

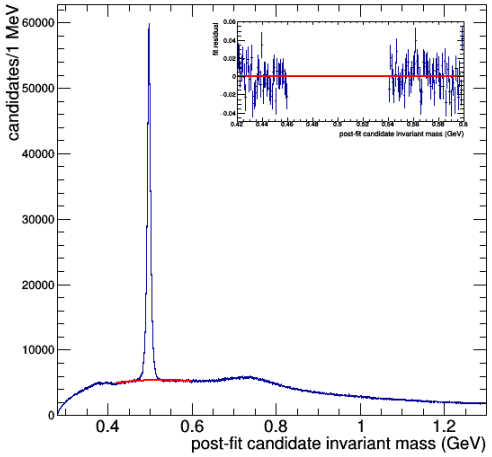

Figure 4.39: Distribution of the post-vertex fit invariant mass of K^0_S candidates in data. The candidates are pairs of tracks that pass our track selection requirements and form a vertex with $\chi^2/\mathrm{dof} < 5$. The candidates in the K^0_S mass window (490–505 MeV) are chosen, and low-mass (420–460 MeV) and high-mass (540–600 MeV) sidebands are fit to estimate the background. The inset shows the fit residuals for the low-mass and high-mass sidebands.

Figure 4.41 shows the distributions of vertex distances d_{BV} for the K^0_S candidates, in the HIP-affected and non-HIP-affected data and simulation, along with the ratios HIP/non-HIP. For the data, the numerator of this ratio is from the HIP-affected data-taking eras 2016 B–F, and the denominator is from the non-HIP-affected data taking eras 2016 G–H. For the simulation, the numerator is from QCD MC samples with HIP simulation+mitigation, and the denominator is from the nominal QCD MC samples.

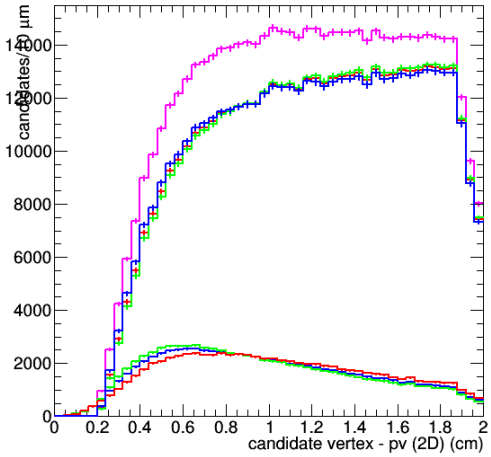

Figure 4.40: Distribution of the vertex distances d_{BV} of K^0_S candidates in data. The pink curve corresponds to all candidates in the on-peak mass window. The lower set of red, green, and blue curves represent the background samples in the low-mass window, the high-mass window, and the weighted average, respectively, while the corresponding upper set of curves represent the background-subtracted distribution.

The ratio HIP/non-HIP of K^0_S vertex distances d_{BV} in data is mostly flat, except with a peak for d_{BV} below approximately 5 mm. This is due to differences in the distributions of the impact parameters of the tracks that compose the K^0_S candidates. Figure 4.42 shows the corresponding ratio HIP/non-HIP of the track impact parameters in the data. There is a peak for small values of the impact parameter, but this peak disappears if the $|d_{xy}|/\sigma_{d_{xy}} > 4$ requirement is removed, which shows that it is an effect of our cut. Figure 4.43 shows the distribution of the uncertainty in the track impact parameter in HIP-affected and non-HIP-affected data, without the requirement on the impact parameter significance. The difference causes the peak in the ratio of the track impact parameters, and the related uncertainty is taken into account in the track resolution study described in the previous subsection. The remaining difference from 1 in the ratio, at around 90–95%, is consistent with the level found in the simulated samples. We therefore proceed to use the signal samples with HIP simulation+mitigation.

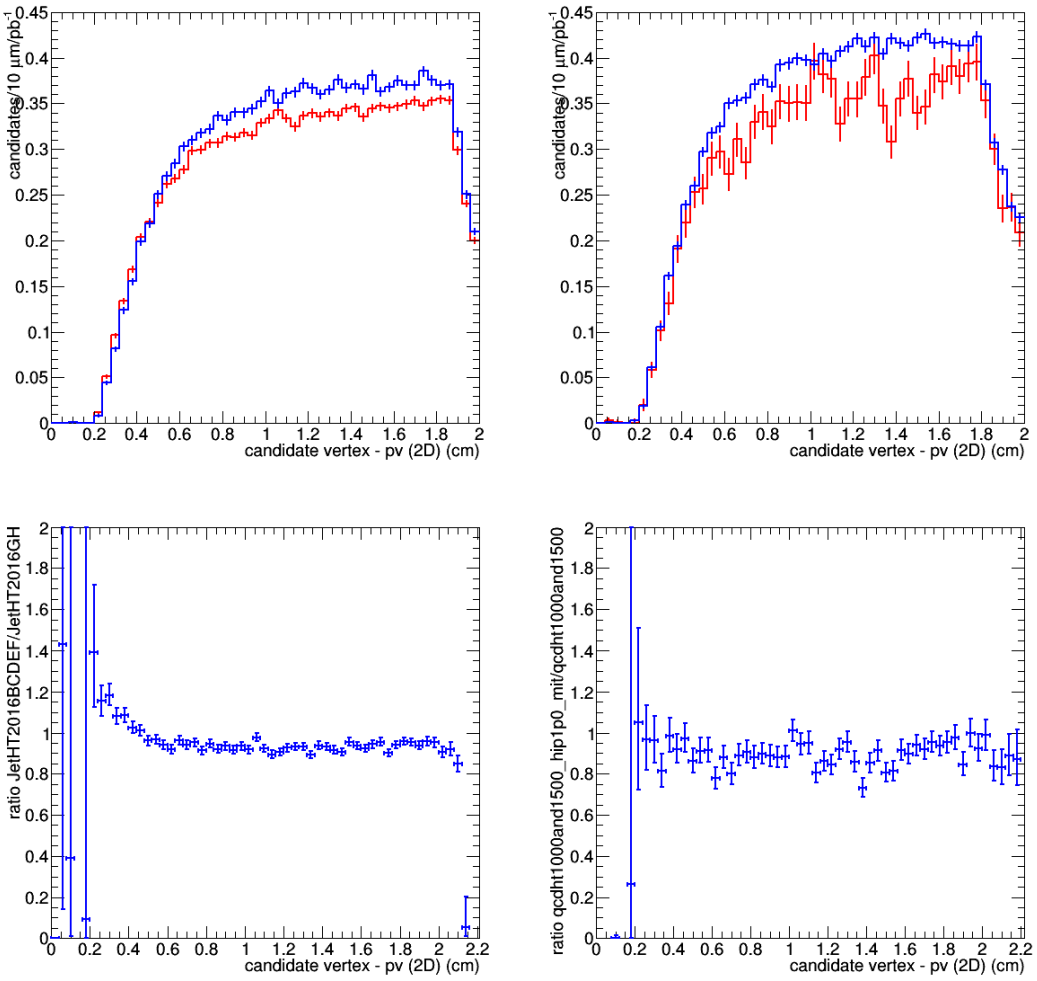

Figure 4.41: (Top left) Distribution of the vertex distances d_{BV} of K_S^0 candidates in data, scaled by integrated luminosity, with the HIP-affected data-taking eras 2016 B–F shown in red, and the non-HIP-affected data-taking eras 2016 G–H shown in blue. (Top right) Distribution of the vertex distances d_{BV} of K_S^0 candidates in simulation, with the HIP+mitigation simulated samples shown in red, and the nominal simulated samples shown in blue. (Bottom) Ratio HIP/non-HIP of the distribution of the vertex distances d_{BV} of K_S^0 candidates, for data (left) and simulation (right).

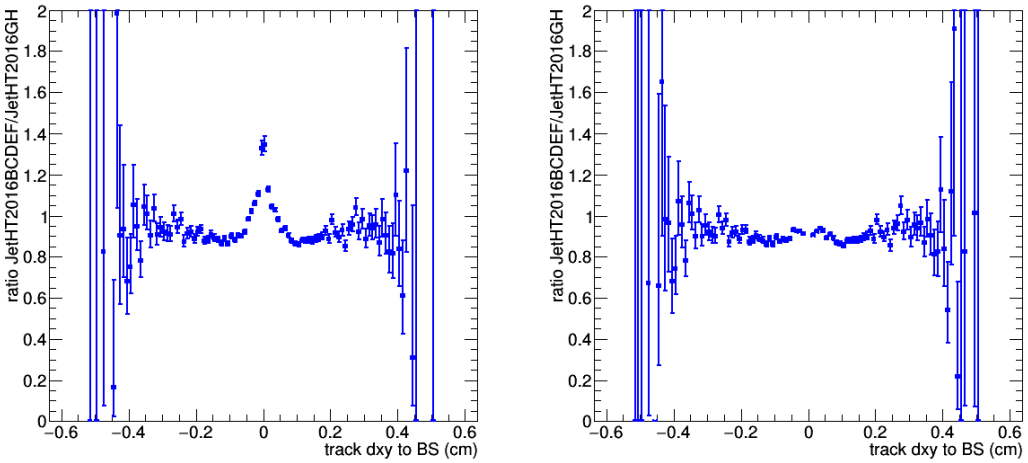

Figure 4.42: Ratio HIP/non-HIP of the distribution of the impact parameter of the tracks that compose the K^0_S candidates, with (left) and without (right) the requirement on the track impact parameter significance.

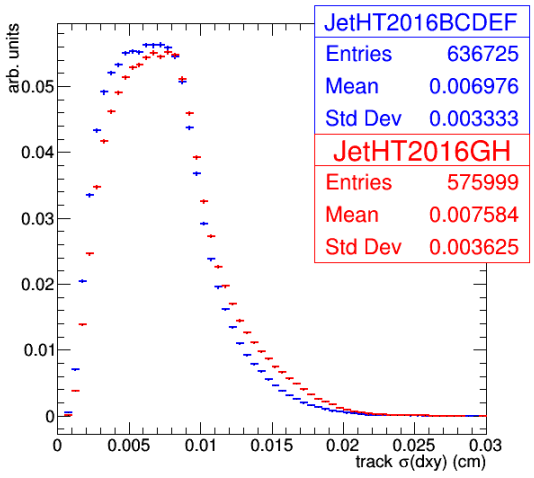

Figure 4.43: Distribution of the uncertainty in impact parameter of the tracks that compose the K^0_S candidates, but without the requirement on the track impact parameter significance.

Jet energy scale/resolution

The uncertainties in the jet energy scale and resolution [33] could affect the total jet energy and change the probability that events satisfy the H_{T} selection. Varying the jet energy scale by one standard deviation results in a change in the signal efficiency of 5% or less for all signal samples, and varying the jet energy resolution by one standard deviation changes the efficiency by 2% or less (Figure 4.44). We therefore assign these as the corresponding systematic uncertainties in the signal efficiency.

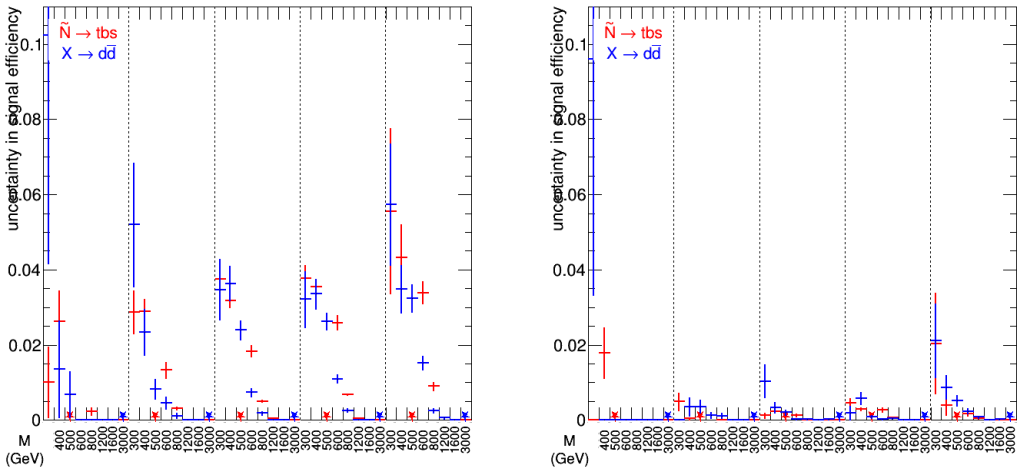

Figure 4.44: Fractional change in signal efficiency due to variations in the jet energy scale (left) and the jet energy resolution (right), as a function of signal mass and lifetime.

Integrated luminosity

The uncertainty in the integrated luminosity is 2.3% for 2015 [2] and 2.5% for 2016 [3].

Pileup

The uncertainty in the signal efficiency due to pileup is 2% (Figure 4.45).

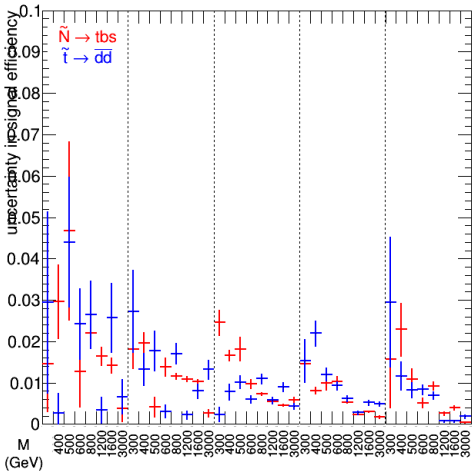

Figure 4.45: Fractional change in signal efficiency due to a variation in the pileup distribution, as a function of signal mass and lifetime.

Trigger efficiency

The uncertainty in the trigger efficiency is 1% (Sec. 4.2.1).

Summary of systematic uncertainties in signal efficiency

Table 4.13 summarizes the systematic uncertainties in the signal efficiency. We assume there are no correlations among them, and add them in quadrature to obtain the overall uncertainty.

Table 4.13: Systematic uncertainties in the signal efficiency. The overall uncertainty is the sum in quadrature of the individual uncertainties, assuming no correlations.

Systematic effect	Uncertainty (%)
Vertex reconstruction	23
Track resolution	5
Jet energy scale/resolution	5
Integrated luminosity	3
Pileup	2
Trigger efficiency	1
Overall	24

4.6.2 Systematic uncertainties in the background template

The $d_{\mathrm{VV}}^{\mathrm{C}}$ background template is constructed from the large sample of events in data with exactly one vertex. Systematic uncertainties in the background template arise from effects that could cause differences between the constructed $d_{\mathrm{VV}}^{\mathrm{C}}$ distribution and the true d_{VV} distribution of two-vertex background events. The 3-track control sample is used to evaluate the scale of these differences. The deviation from unity of the ratio of the predicted yield in each bin of the $d_{\mathrm{VV}}^{\mathrm{C}}$ template to the observed yield in the same bin, which is referred to as the closure, is a measure of the systematic uncertainty. Additional uncertainties arise from effects that could compromise the validity of applying the 3-track control sample to the $\geq$5-track sample.

We check the assumption that closure of the $d_{\mathrm{VV}}^{\mathrm{C}}$ construction method in 3-track vertices implies closure in $\geq$5-track vertices by varying the inputs to the template construction procedure and evaluating the resulting shifts in the $d_{\mathrm{VV}}^{\mathrm{C}}$ template. Constructing $d_{\mathrm{VV}}^{\mathrm{C}}$ involves sampling two values of d_{BV} and an angle between vertices $\Delta\phi_{\mathrm{VV}}$, the efficiency to keep pairs of vertices as a function of d_{VV}, and the b quark correction factors. Therefore, the main effects are related to these distributions. We include additional systematic uncertainties to account for possible differences in $d_{\mathrm{VV}}^{\mathrm{C}}$ predictions due to variations in these distributions from 3-track vertices to $\geq$5-track vertices.

Distribution of the angle between vertices

In background template construction, the $\Delta\phi_{\mathrm{VV}}$ distribution is modeled using the $\Delta\phi_{\mathrm{JJ}}$ distribution in 3-track one-vertex events. The $\Delta\phi_{\mathrm{JJ}}$ distribution in $\geq$5-track one-vertex events is indistinguishable from that in 3-track one-vertex events. Potential bias could arise if the distribution of angles between jets and vertices differ

for 3-track and ≥5-track vertices. Indeed, the correlation between vertex displacement directions and jet directions is smaller for ≥5-track vertices than for 3-track vertices. To probe the impact, we construct $d_{\mathrm{VV}}^{\mathrm{C}}$ using a variation of the $\Delta\phi_{\mathrm{VV}}$ input in which we assume that the displacement directions are uncorrelated with the jet momentum directions and draw $\Delta\phi_{\mathrm{VV}}$ from a uniform distribution. Figure 4.46 compares the constructed $\Delta\phi_{\mathrm{VV}}$ distributions resulting from this method and from the standard one, and shows the ratios of predicted yields in the three $d_{\mathrm{VV}}^{\mathrm{C}}$ bins. We assign the fractional change in the $d_{\mathrm{VV}}^{\mathrm{C}}$ prediction in each bin as the systematic uncertainty.

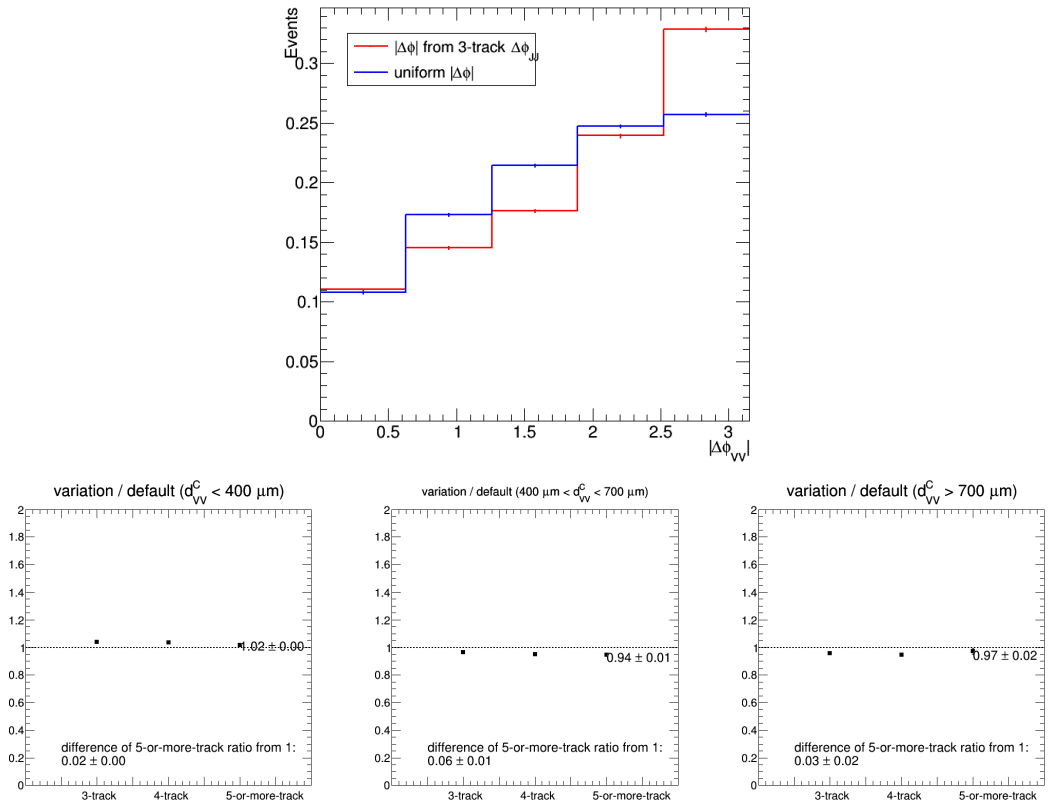

Figure 4.46: (Top) Constructed $\Delta\phi_{\mathrm{VV}}$ distribution using a variation in the $\Delta\phi_{\mathrm{VV}}$ input. (Bottom left) Ratios of simulated yields in the region $d_{\mathrm{VV}}^{\mathrm{C}} < 400\,\mu$m. (Bottom middle) Ratios of simulated yields in the region $400 < d_{\mathrm{VV}}^{\mathrm{C}} < 700\,\mu$m. (Bottom right) Ratios of simulated yields in the region $d_{\mathrm{VV}}^{\mathrm{C}} > 700\,\mu$m.

Efficiency to keep pairs of vertices

The template also depends on the probability that pairs of nearby vertices will both survive the vertex reconstruction algorithm as a function of their separation d_{VV}. The efficiency to merge pairs of vertices is determined from the vertex reconstruction algorithm. To assess the uncertainty due to variations in this efficiency, we use a variation of the algorithm in which the seed vertices are composed of five tracks, rather than the usual two. We then construct a variation of $d_{\mathrm{VV}}^{\mathrm{C}}$ using the resulting efficiency curve and take the fractional change in the $d_{\mathrm{VV}}^{\mathrm{C}}$ prediction in each bin as the systematic uncertainty. Figure 4.47 compares the efficiency distributions from the two methods, and shows the ratios of predicted yields in the three $d_{\mathrm{VV}}^{\mathrm{C}}$ bins.

Modeling of b quark correction

The corrections to the $d_{\mathrm{VV}}^{\mathrm{C}}$ template that account for d_{BV} correlations due to the pair production of b quarks are derived using the fraction of simulated 3-track two-vertex events with b quarks. This fraction could differ for $\geq$5-track two-vertex events. To assess the related systematic uncertainty, we recompute the b quark corrections using the extreme case in which all two-vertex events contain b quarks, and determine the fractional shifts in the $d_{\mathrm{VV}}^{\mathrm{C}}$ yields in each bin. Figure 4.48 shows the b quark corrections resulting from this variation, as well as the ratios of predicted yields in the three $d_{\mathrm{VV}}^{\mathrm{C}}$ bins.

The b quark correction is the only input to the $d_{\mathrm{VV}}^{\mathrm{C}}$ construction method that is taken from the MC simulation. To study the effect due to a possible difference between data and MC in the b quark p_{T} spectrum, we check the dependence of the d_{BV} distributions on b quark p_{T}. Figure 4.49 shows the mean d_{BV} as a function of b quark p_{T} for 3-track, 4-track, and 5-or-more-track one-vertex events. The

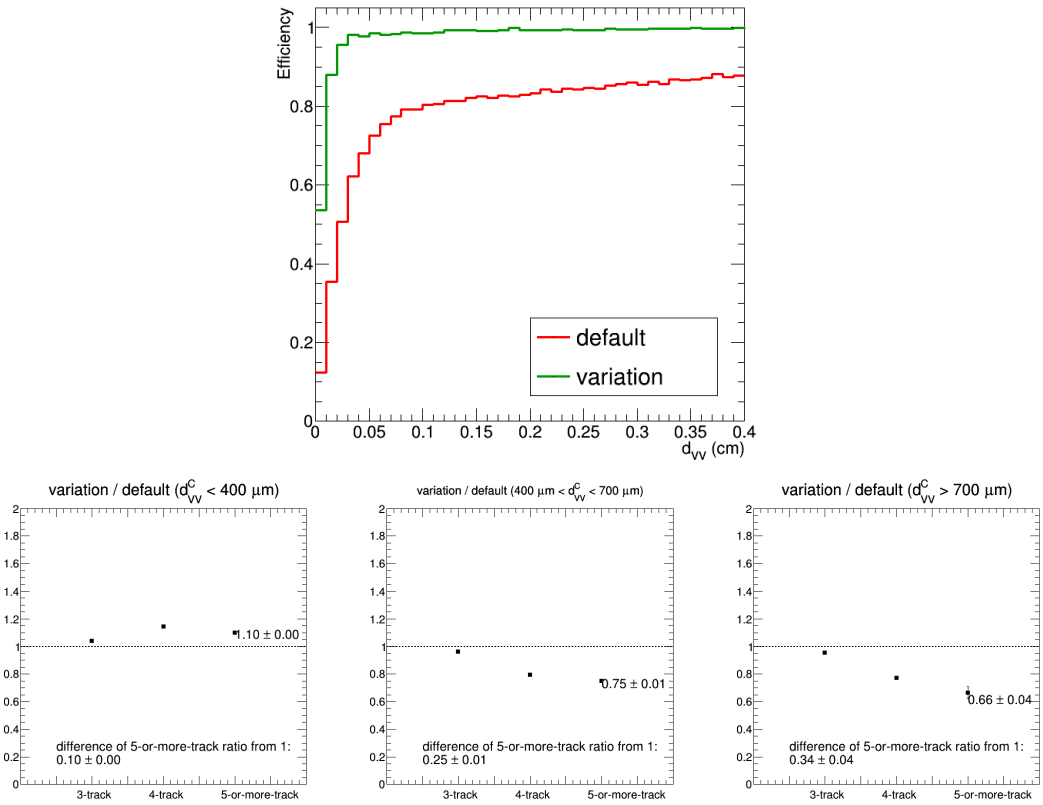

Figure 4.47: (Top) Distributions of the efficiency to keep pairs of vertices as a function of d_{VV}, from two methods. (Bottom left) Ratios of simulated yields in the region $d^{\mathrm{C}}_{\mathrm{VV}} < 400\,\mu$m. (Bottom middle) Ratios of simulated yields in the region $400 < d^{\mathrm{C}}_{\mathrm{VV}} < 700\,\mu$m. (Bottom right) Ratios of simulated yields in the region $d^{\mathrm{C}}_{\mathrm{VV}} > 700\,\mu$m.

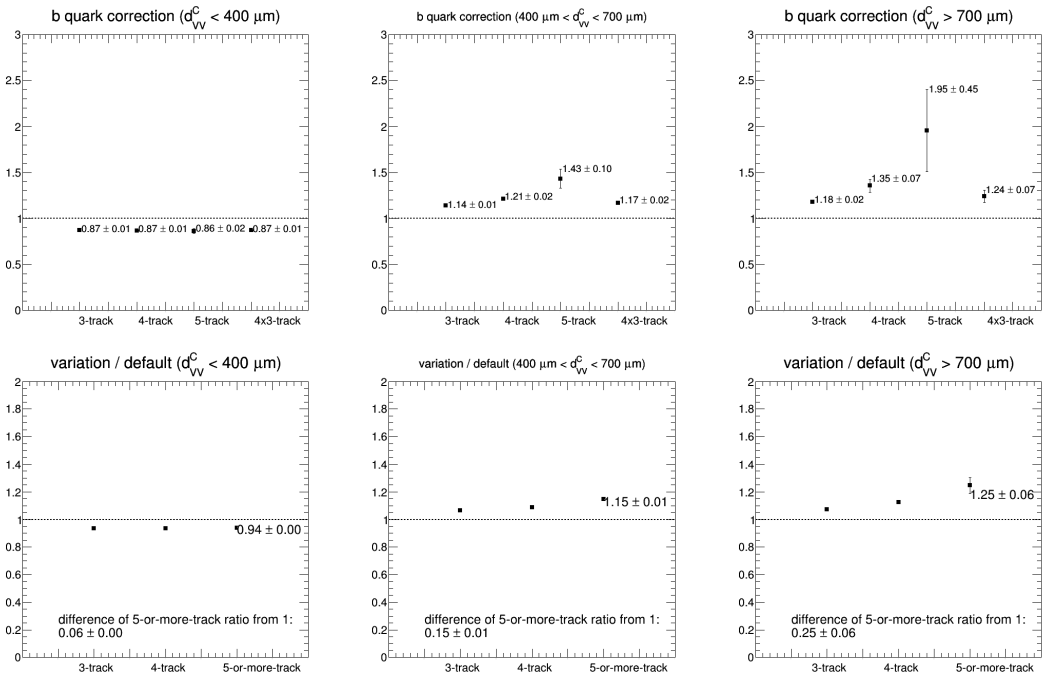

Figure 4.48: (Top) b quark corrections derived using a variation in the method. (Bottom left) Ratios of simulated yields in the region $d^{\mathrm{C}}_{\mathrm{VV}} < 400\,\mu$m. (Bottom middle) Ratios of simulated yields in the region $400 < d^{\mathrm{C}}_{\mathrm{VV}} < 700\,\mu$m. (Bottom right) Ratios of simulated yields in the region $d^{\mathrm{C}}_{\mathrm{VV}} > 700\,\mu$m.

distributions are flat, which shows that d_{BV} does not depend on b quark p_{T}, but only on whether or not the event has a b quark. This means that a possible difference in the b quark p_{T} spectrum between data and MC would not have an effect on the b quark corrections.

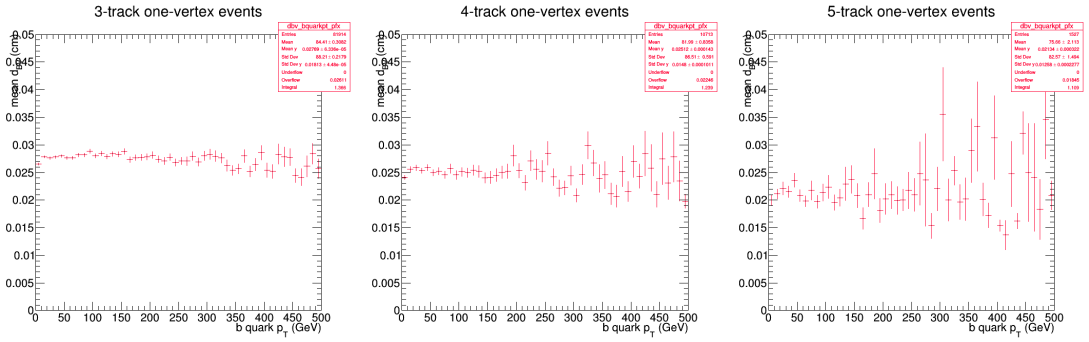

Figure 4.49: Mean d_{BV} as a function of b quark p_{T}, for 3-track (left), 4-track (middle), and 5-or-more-track (right) one-vertex events.

The statistical uncertainties in the b quark corrections are also taken as systematic uncertainties in the template.

Pileup

The background template is constructed from data, so its dependence on pileup is taken into account in the construction procedure. Here we check the effect of mixing one-vertex events with different pileup distributions, as is done in our default method, by sorting the simulated one-vertex events into bins of the true number of pileup interactions, constructing the $d_{\mathrm{VV}}^{\mathrm{C}}$ distributions for each, and then combining. Figure 4.50 shows the $d_{\mathrm{VV}}^{\mathrm{C}}$ distributions obtained with this procedure, compared with the default method. The differences in predicted yields in each $d_{\mathrm{VV}}^{\mathrm{C}}$ bin are less than 1%, so we take the effect to be negligible.

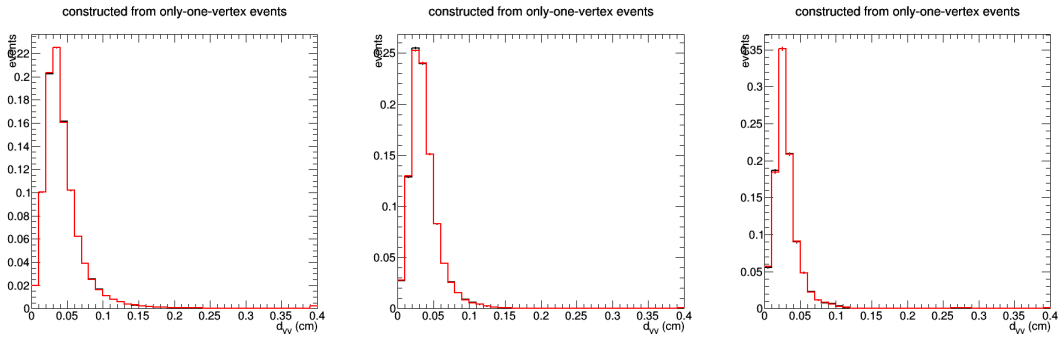

Figure 4.50: Background template, $d_{\mathrm{VV}}^{\mathrm{C}}$, constructed using the default method (black) and sorting by the true number of pileup interactions (red), for 3-track (left), 4-track (middle), and 5-or-more-track (right) vertices.

Combining datasets

We checked whether it is possible to combine the datasets with and without the HIP effect. Figure 4.51 compares the $d_{\mathrm{VV}}^{\mathrm{C}}$ distributions constructed from the 3-track one-vertex events in 10% of the 2016 data, using the BCDEFGH samples combined vs. using the BCDEF and GH samples separately then adding the $d_{\mathrm{VV}}^{\mathrm{C}}$ distributions weighted by integrated luminosity. The distributions are very similar: the changes in the normalized background predictions in each $d_{\mathrm{VV}}^{\mathrm{C}}$ bin are less than 1%. We choose to combine the datasets in our background template construction.

Summary of systematic uncertainties in the background template

The systematic uncertainty in the background template, $d_{\mathrm{VV}}^{\mathrm{C}}$, is estimated using a combination of the closure of the construction method in the control sample of 3-track vertices and the difference in effects from 3-track vertices to $\geq$5-track vertices. Table 4.14 lists the shifts arising from these components for each of the three d_{VV} bins, along with their statistical uncertainties. The statistical uncertainties in the shifts take into account the correlation between the default template and the variation. In assessing the overall systematic uncertainty in the background template, we add in quadrature the shifts and their uncertainties, assuming no

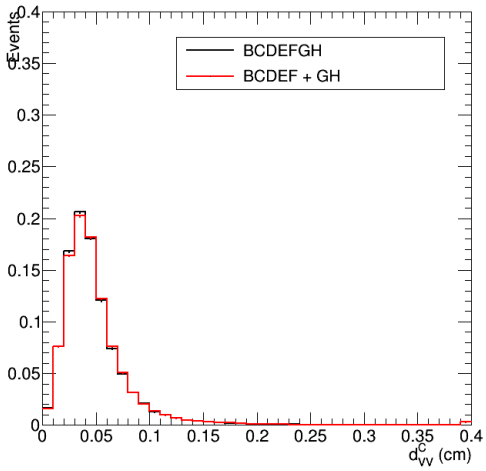

Figure 4.51: Background template, $d_{\mathrm{VV}}^{\mathrm{C}}$, constructed from 3-track one-vertex events in 10% of the 2016 data, using the BCDEFGH samples combined vs. using the BCDEF and GH samples separately then adding the $d_{\mathrm{VV}}^{\mathrm{C}}$ distributions weighted by integrated luminosity.

correlations.

Table 4.14: Systematic shifts in the background prediction in each $d_{\mathrm{VV}}^{\mathrm{C}}$ bin arising from varying the construction of the $d_{\mathrm{VV}}^{\mathrm{C}}$ template. The overall systematic uncertainty is the sum in quadrature of the shifts and their statistical uncertainties, assuming no correlations among the sources.

	Shift (%)		
Systematic effect	0–0.4 mm	0.4–0.7 mm	0.7–40 mm
Closure in 3-track control sample	-7 ± 6	-3 ± 7	$+44 \pm 20$
Difference from 3-track to $\geq$5-track vertices:			
Modeling of $\Delta\phi_{\mathrm{VV}}$	$+4 \pm 0$	-5 ± 1	-2 ± 3
Modeling of vertex survival efficiency	$+20 \pm 1$	-19 ± 2	-26 ± 7
Modeling of b quark correction	-11 ± 1	$+9 \pm 2$	$+18 \pm 9$
b quark correction statistical uncertainty	± 3	± 9	± 36
Overall systematic uncertainty	25	25	69

4.7 Signal extraction and statistical interpretation

In our analysis, we use simulation to obtain the signal templates and to derive the b quark corrections used in the background template construction. We also used

simulation to optimize the cut selection and to develop the background estimation procedure, but the final background template and systematic uncertainties come from data, so discrepancies do not affect the results.

We unblinded the data in steps, starting with 10% of the data evenly spread among the data-taking eras in 2015 and 2016. With 10% of data, first we looked at the 3-track one-vertex control sample. Initially there was a disagreement between data and simulation that was consistent with the HIP effect, so we tightened the requirement on the number of strip layers to eliminate bad short tracks and found that the data/MC agreement for vertex variables improved. From that time on, there were no further changes in the event selection and background template construction procedure. Then we proceeded to look at the 3-track two-vertex control sample in 10% of the data, tested closure of the $d_{\mathrm{VV}}^{\mathrm{C}}$ construction method, and found that the ratios of predicted yields to observed yields in each d_{VV} bin were consistent with unity. We also confirmed that combining the events from the different data-taking eras introduced negligible bias in the background template construction. In multiple steps, we then looked at the rest of the control regions, first in 10% of the data, and then in the full dataset. At each step there were no surprises, and with preapproval of the analysis, we unblinded the signal region.

We search for a signal in events with two vertices with at least five tracks each. In the full 2015+2016 dataset, we observe one 5-or-more-track two-vertex event. Table 4.15 gives the values of the event and vertex variables for this event, and Figure 4.52 shows an event display.

To determine the signal yield, we perform binned shape fits of the signal and background templates to the d_{VV} distribution using an extended likelihood method [42].

The background template is constructed from the one-vertex events in data,

Table 4.15: Run 283820, luminosity block 634, event 1114081375.

Variable	Vertex 0	Vertex 1
H_{T}	1106 GeV	
number of jets	5	
number of tracks	5	5
d_{BV}, xy distance from beamspot	217 μm	182 μm
uncertainty in d_{BV}	15 μm	14 μm
d_{VV}, xy distance between vertices	396 μm	

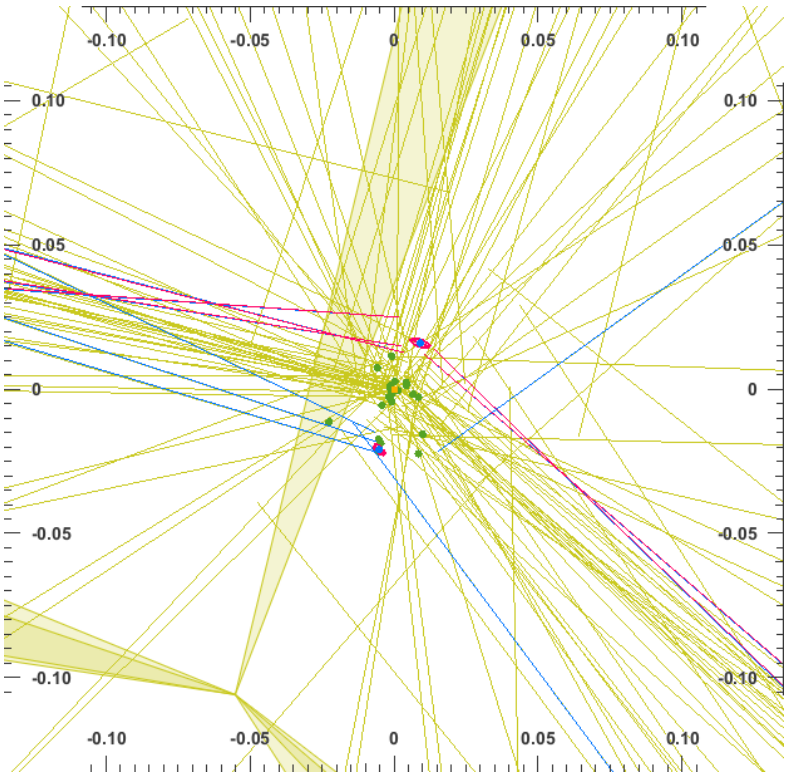

Figure 4.52: Run 283820, luminosity block 634, event 1114081375. The orange square is the beamspot, green points are primary vertices, yellow lines are tracks, and yellow cones are jets (drawn from the detector origin). The two displaced vertices are indicated as blue points, with the uncertainty as a pink ellipse. The associated tracks are blue lines for one vertex and pink lines for the other vertex.

while the signal templates are produced directly using the d_{VV} distributions from simulation. There is one signal template for each signal model, mass, and lifetime.

The lower right plot in Fig. 4.31 compares the $d_{\mathrm{VV}}^{\mathrm{C}}$ and d_{VV} distributions in the signal region. The observed number of events in each bin, along with the predictions from the background-only fit and from example signal models, are listed in Table 4.16. The background-only fit normalizes the prediction from the $d_{\mathrm{VV}}^{\mathrm{C}}$ background template to the observed number of two-vertex events. For the signal-plus-background fits, the signal yield is constrained to be nonnegative. Since there is only one two-vertex event in the data, falling in the 0–0.4 mm d_{VV} bin, the fits to the observed distribution prefer zero signal yield.

Table 4.16: For each d_{VV} bin in $\geq$5-track two-vertex events: the predicted background yield from the background-only fit, the observed yield, and the predicted signal yields for simulated multijet signals with $M = 2000\,\mathrm{GeV}$, production cross section 1 fb, and $c\tau = 0.3$, 1, and 10 mm. The systematic uncertainties in the predicted background yields reflect the fractional systematic uncertainties given in Table 4.14, and the uncertainties in the predicted signal yields reflect the fractional systematic uncertainty given in Table 4.13.

			Predicted multijet signal yields		
d_{VV} range	Fitted background yield	Observed	0.3 mm	1 mm	10 mm
0–0.4 mm	$0.51 \pm 0.01\,(\mathrm{stat}) \pm 0.13\,(\mathrm{syst})$	1	2.8 ± 0.7	3.5 ± 0.8	1.0 ± 0.2
0.4–0.7 mm	$0.37 \pm 0.02\,(\mathrm{stat}) \pm 0.09\,(\mathrm{syst})$	0	2.0 ± 0.5	3.7 ± 0.9	0.5 ± 0.1
0.7–40 mm	$0.12 \pm 0.02\,(\mathrm{stat}) \pm 0.08\,(\mathrm{syst})$	0	1.1 ± 0.3	11 ± 3	31 ± 7

Upper limits on the signal cross section are set using a Bayesian technique [43]. A uniform prior is taken for positive values of the signal cross section. The signal efficiency is constrained by a log-normal prior with a width of 24%, reflecting the overall uncertainty in the signal efficiency (Table 4.13). The only assumed uncertainty in the shape of the signal templates is that due to the finite number of events in the simulation; this uncertainty can be as large as 20% for the lower lifetime and mass samples that have small efficiencies. For the uncertainty in the background, log-normal priors are taken for the yield in each bin, with widths

given by the fractional uncertainties listed in Table 4.14.

Figure 4.53 shows, as a function of lifetime and mass, the observed 95% confidence level (CL) upper limits on the product of the signal pair production cross section and the square of the branching fraction for its decay ($\sigma\mathcal{B}^2$) for both the multijet and dijet signals. The expected limits are similar. Exclusion curves are overlaid, assuming gluino and top squark pair production cross sections [44] and 100% branching fraction, for both the observed and expected 95% CL upper limits. The upper limits reflect the signal efficiencies shown in Fig. 4.23, initially improving as lifetime increases, but worsening at approximately 40 mm due to the fiducial limit at the beam pipe. As an example, for a neutralino with mass of 800 GeV and $c\tau = 1$ mm, the observed 95% CL upper limit on $\sigma\mathcal{B}^2$ is 0.3 fb. For mean proper decay lengths between 0.6 and 80 mm, gluino masses are excluded below 2200 GeV, and top squark masses are excluded below 1400 GeV. Figure 4.54 shows the upper limits as a function of mass for several values of $c\tau$, and Fig. 4.55 shows the upper limits as a function of $c\tau$ for several values of the mass.

In Fig. 4.55, the narrowing of the expected limit bands above $c\tau = 2$ mm is due to the correlation between the signal lifetime and the relative signal yields in the three d_{VV} bins. The low background yield causes the discrete nature of the Poisson distribution to have an effect: the pseudo-data sets used to calculate the distribution of expected limits have a limited number of combinations of yields in each bin. For example, for a simulated multijet signal with $M = 1600$ GeV and $c\tau = 4$ mm, the signal is concentrated almost entirely (>90%) in the last bin. The majority of pseudo-data sets that are different in only the first two bins then have nearly the same expected limit value. The bands widen above $c\tau = 20$ mm with the reappearance of signal in the first bin due to the effect described in Section 4.4 in which two vertices are reconstructed from the same long-lived particle, an effect

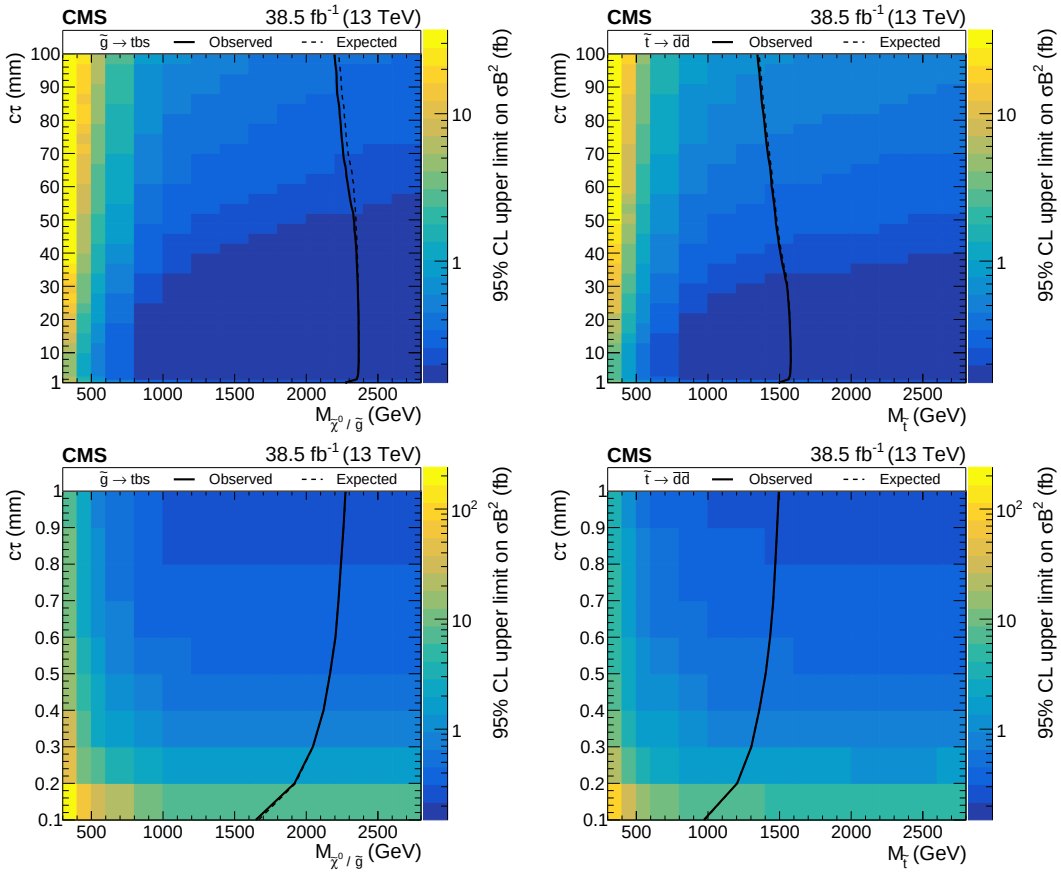

Figure 4.53: Observed 95% CL upper limits on $\sigma\mathcal{B}^2$ for the multijet (left) and dijet (right) signals as a function of mass and mean proper decay length. The upper plots span $c\tau$ from 1 to 100 mm, and the lower plots span $c\tau$ from 0.1 to 1 mm. The overlaid mass exclusion curves assume gluino pair production cross sections for the multijet signals and top squark pair production cross sections for the dijet signals, and 100% branching fraction.

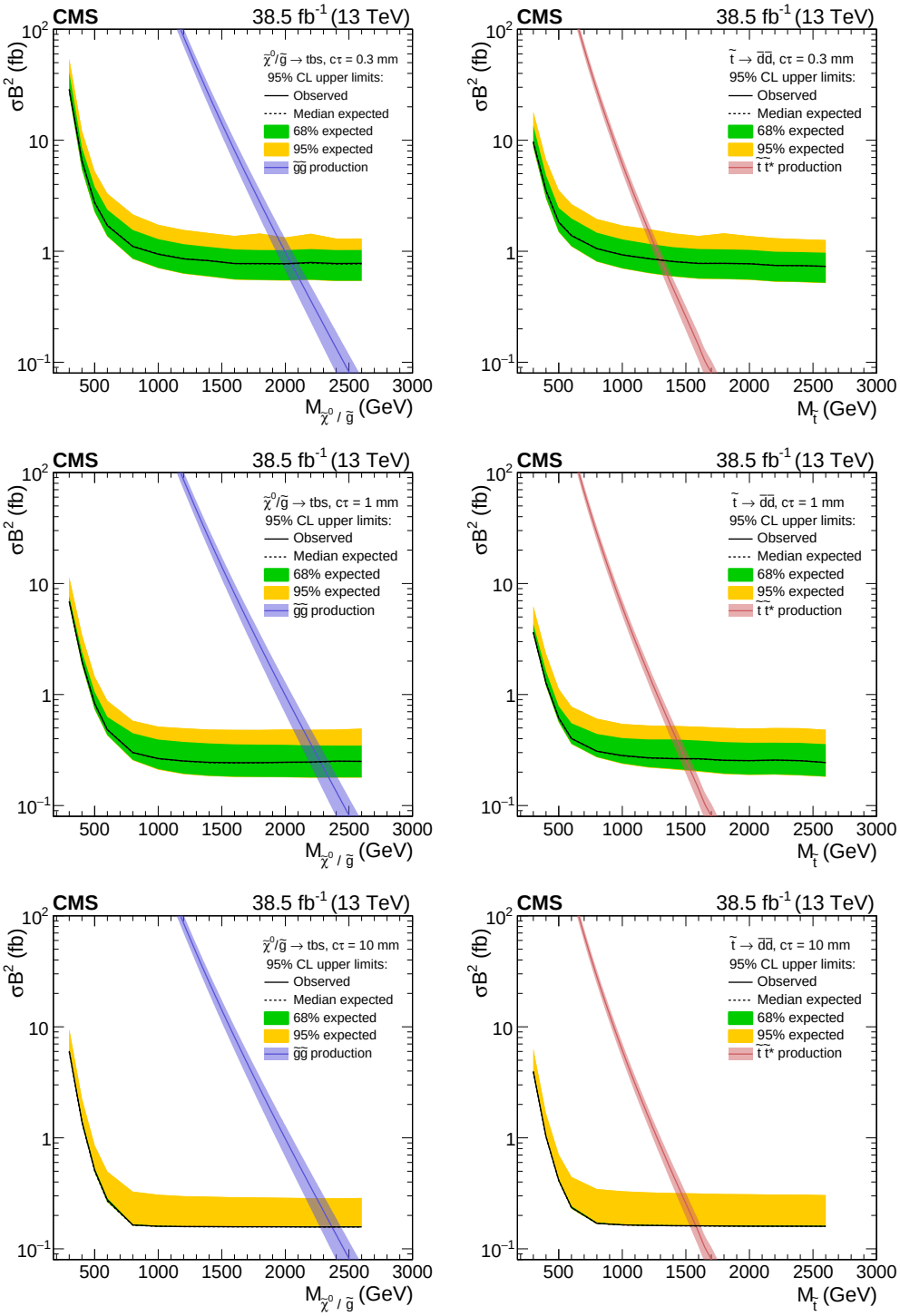

Figure 4.54: Observed and expected 95% CL upper limits on $\sigma\mathcal{B}^2$ for the multijet (left) and dijet (right) signals, as a function of mass for a fixed $c\tau$ of 0.3 mm (upper), 1 mm (middle), and 10 mm (lower). The gluino pair production cross section is overlaid for the multijet signals, and the top squark pair production cross section is overlaid for the dijet signals.

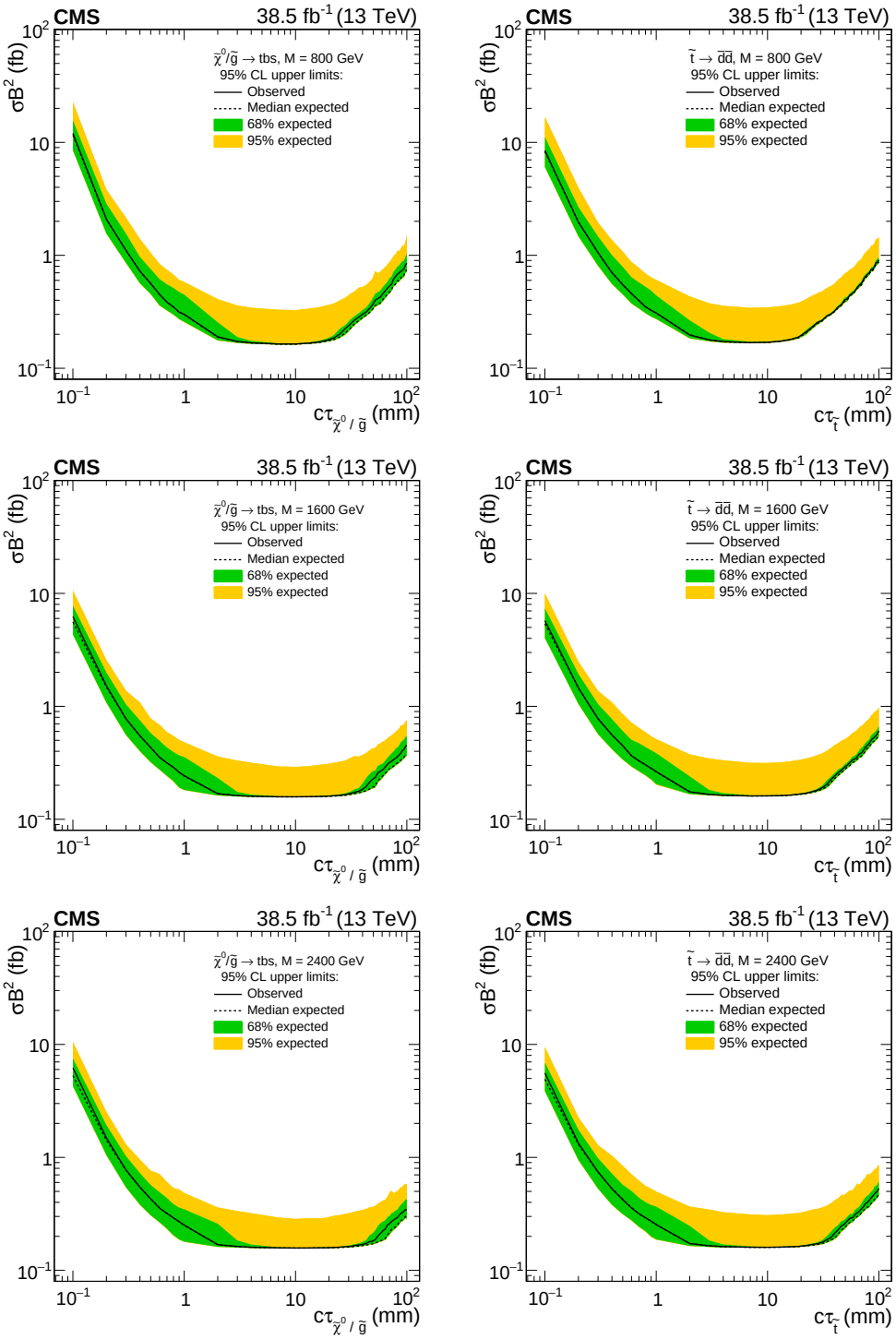

Figure 4.55: Observed and expected 95% CL upper limits on $\sigma\mathcal{B}^2$ for the multijet (left) and dijet (right) signals, as a function of $c\tau$ for a fixed mass of 800 GeV (upper), 1600 GeV (middle), and 2400 GeV (lower).

that is larger for the multijet signals.

Figure 4.56 shows examples of the distribution of expected limits in toy datasets for multijet signals with $M = 1600\,\text{GeV}$ and $c\tau$ of 1 mm and 4 mm.

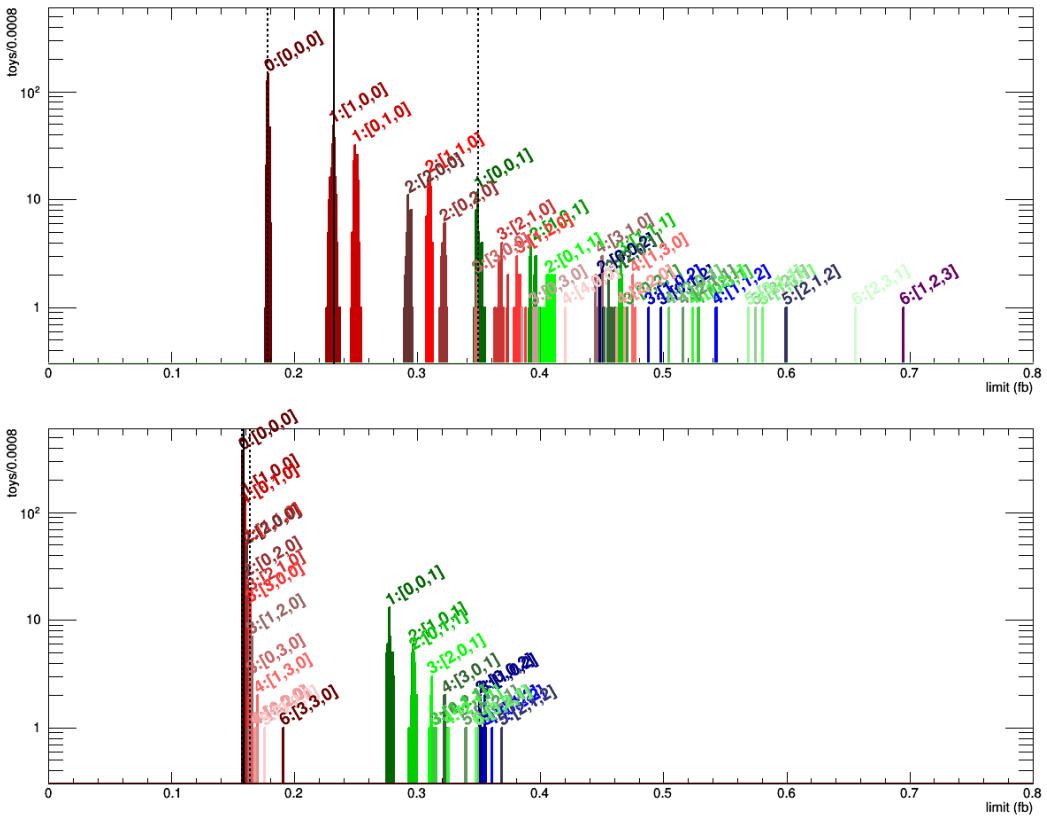

Figure 4.56: The distribution of expected limits in 1000 toy datasets for the multijet signal model with mass 1600 GeV, for lifetimes $\tau = 1\,\text{mm}$ (top) and $\tau = 4\,\text{mm}$ (bottom). Different colors represent the different discrete toy results, grouped in color by the number of events in the last d_{VV} bin (e.g. red means zero events in the last bin, green one event, etc.). The text labels describe the distribution of events in the toys, e.g., "3:[2,1,0]" represents the set of toys in which there were three total events, with two events in the first bin, one in the second bin, and zero in the last bin. The superimposed vertical lines correspond to the quantiles: the solid line is the median expected limit, and the two dashed lines are the $\pm 1\sigma$ bands.

4.8 Extending the search to other signal models

This search for displaced vertices applies to other types of long-lived particles decaying to multiple jets. Here we present a generator-level selection that can be used to reinterpret the results of our analysis. For signal models in which there are two long-lived particles, this generator-level selection approximately replicates the reconstruction-level efficiency. The selection is based on the number and momenta of generated jets in the event, the displacements of the long-lived particles, and the momenta of their daughter particles. The generated jets are those clustered from all final-state particles except neutrinos, using the anti-k_{T} algorithm with a distance parameter of 0.4, but are rejected if the fraction of energy from electrons is greater than 0.9 or if the fraction of energy from muons is greater than 0.8. The daughter particles are the u, d, s, c, and b quarks, electrons, muons, and tau leptons from the decay of the long-lived particle, and we consider those with an impact parameter with respect to the origin measured in the x-y plane of at least 0.1 mm. The generated jets and daughter particles are required to satisfy $p_{\mathrm{T}} > 20\,\mathrm{GeV}$ and $|\eta| < 2.5$.

The criteria of the generator-level selection are as follows: at least four generated jets; $H_{\mathrm{T}} > 1000\,\mathrm{GeV}$, where H_{T} is the scalar sum of the p_{T} of generated jets with $p_{\mathrm{T}} > 40\,\mathrm{GeV}$; for each long-lived particle, a distance of the decay point from the origin measured in the x-y plane of between 0.1 and 20 mm, and a value of Σp_{T} of the daughter particles of at least 350 GeV; and a distance between the decay points of the long-lived particles measured in the x-y plane of at least 0.4 mm. In calculating the Σp_{T} of the daughter particles, we multiply the p_{T} of b quark daughter particles by a factor of 0.65. This accounts for the lower reconstruction-level efficiency due to the lifetime of heavy flavor particles, which can impede the association of their decay products with the reconstructed vertices.

This generator-level selection replicates the reconstruction-level efficiency with a typical accuracy of 20% for a variety of models for which the signal efficiency is high (>10%). In the region with $d_{\mathrm{VV}} > 0.4\,\mathrm{mm}$, there are no observed events.

Table 4.17 summarizes the generator-level equivalents for each of our reconstructed-level selection criteria, and Figure 4.57 shows a plot of the generator-level efficiency vs. the reconstructed-level efficiency for a variety of signal models. The plot shows that the analysis is sensitive to a wide range of models in which pair-produced long-lived particles each decay into final states with at least two jets. Therefore, signal pair production cross section limits similar to the results of this analysis apply to other related models.

Table 4.17: Generator-level equivalents for each of our reconstructed-level event and vertex selection criteria. Generated jets are required to have $p_{\mathrm{T}} > 20\,\mathrm{GeV}$, $|\eta| < 2.5$, electron energy fraction less than 0.9, and muon energy fraction less than 0.8. "accepted" means $p_{\mathrm{T}} > 20\,\mathrm{GeV}$ and $|\eta| < 2.5$; "displaced" means $|d_{xy}| > 100\,\mu\mathrm{m}$; "daughter particles" means u, d, s, c, and b quarks, electrons, muons, and tau leptons. In calculating the Σp_{T} of the daughter particles, we multiply the p_{T} of b quark daughter particles by a factor of 0.65. This accounts for the lower reconstruction-level efficiency due to the b quark lifetime, which can impede the association of its decay products with the reconstructed vertices.

Reconstructed-level selection	Generator-level selection
at least four jets	at least four generated jets
`HLT_PFHT800` or `HLT_PFHT900` trigger	
H_{T} (jets with $p_{\mathrm{T}} > 40\,\mathrm{GeV}$) $> 1000\,\mathrm{GeV}$	H_{T} (generated jets with $p_{\mathrm{T}} > 40\,\mathrm{GeV}$) $> 1000\,\mathrm{GeV}$
two vertices	
for each vertex:	for each vertex:
$d_{\mathrm{BV}} > 100\,\mu\mathrm{m}$	generated $d_{\mathrm{BV}} > 100\,\mu\mathrm{m}$
xy distance from detector origin $< 20\,\mathrm{mm}$	generated $d_{\mathrm{BV}} < 20\,\mathrm{mm}$
at least five tracks	
uncertainty in $d_{\mathrm{BV}} < 25\,\mu\mathrm{m}$	$\sum p_{\mathrm{T}}$ of accepted displaced daughter particles $> 350\,\mathrm{GeV}$
$d_{\mathrm{VV}} > 400\,\mu\mathrm{m}$	generated $d_{\mathrm{VV}} > 400\,\mu\mathrm{m}$

This chapter described a search for long-lived particles with displaced vertices. The next chapter describes related searches for physics beyond the SM performed by the ATLAS and CMS Collaborations at the LHC.

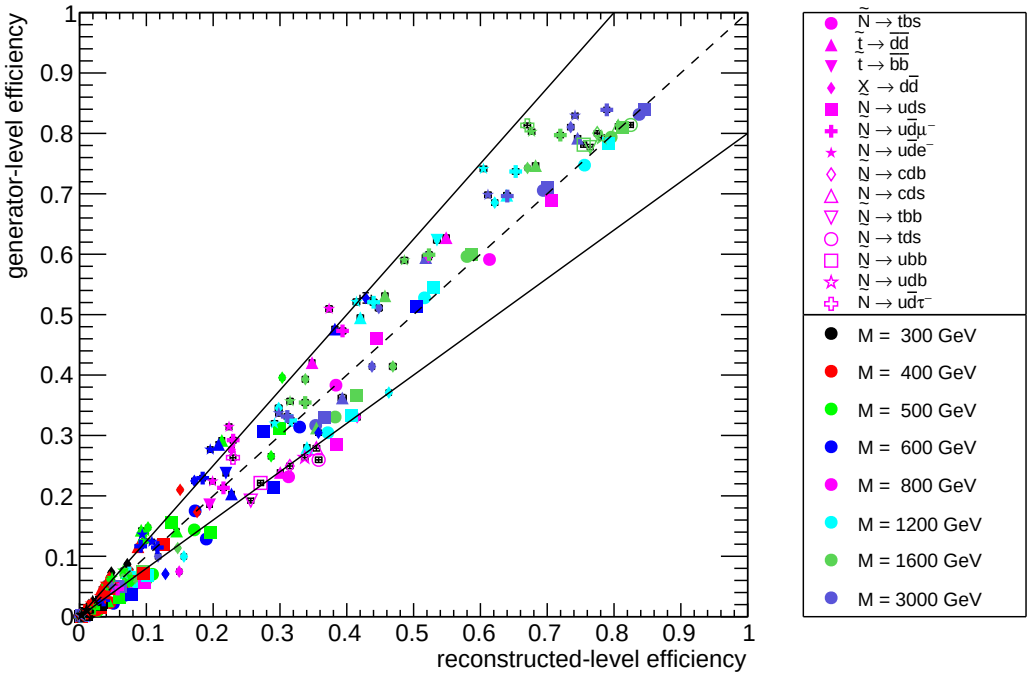

Figure 4.57: Generator-level efficiency vs. reconstructed-level efficiency for various signal models.

CHAPTER 5

RELATED SEARCHES AT THE LHC

This chapter discusses analyses of the 13 TeV LHC data that search for similar models of new physics as those used in the CMS displaced vertex search presented in this dissertation. These include a search for displaced vertices performed by the ATLAS Collaboration [11], as well as a search for displaced jets performed by the CMS Collaboration [17]. This chapter also describes analyses of the 8 TeV or 13 TeV LHC data that search for new physics in complementary regions of parameter space, which include long-lived particles decaying to other final states, as well as RPV SUSY with LSPs that decay promptly to multijet final states.

5.1 ATLAS search for displaced vertices

The ATLAS Collaboration searched for long-lived particles with displaced vertices in events with missing transverse momentum in pp collisions at $\sqrt{s} = 13\,\text{TeV}$ [11]. The analysis builds on a similar search for displaced vertices using pp collisions at $\sqrt{s} = 8\,\text{TeV}$ [45]. It is sensitive to longer lifetimes than the CMS displaced vertex search, because a material map is used to suppress background from hadronic interactions, allowing the selection of displaced vertices with distances from the detector origin up to 300 mm. The material map is visualized in Fig. 5.1. Furthermore, the displaced vertices are composed of tracks that are reconstructed from both the standard ATLAS tracking algorithm and an additional large-radius tracking algorithm used to recover displaced tracks. In the signal region, events are required to have one displaced vertex with at least five tracks and a reconstructed invariant mass of at least 10 GeV. The requirement of only one vertex increases the signal sensitivity at longer lifetimes as compared to the CMS displaced vertex search, which requires two displaced vertices, but decreases the sensitivity at

shorter lifetimes because of the larger SM background closer to the beam axis. The sources of background are hadronic interactions, merged vertices, and accidental crossing of vertices and tracks; the total predicted background yield is $0.02^{+0.02}_{-0.01}$ events. No events are observed, and in a model of split supersymmetry the gluino mass exclusions are up to 2370 GeV for mean proper decay lengths in the range 6–3000 mm.

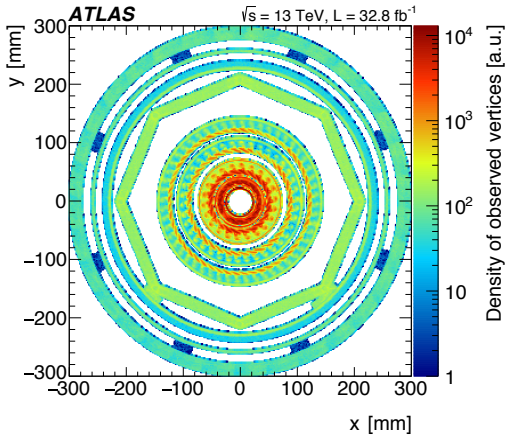

Figure 5.1: Density of observed vertices in regions vetoed by the material map. Figure taken from Ref. [11].

5.2 CMS search for inclusive displaced jets

The CMS Collaboration searched for long-lived particles decaying to displaced jets in pp collisions at $\sqrt{s} = 13\,\text{TeV}$ [17]. This analysis selects events using two customized trigger algorithms, and searches in the distribution of number of displaced jets. One trigger algorithm requires $H_\text{T} > 500\,\text{GeV}$ and at least two jets with $p_\text{T} > 40\,\text{GeV}$, $|\eta| < 2$, and no more than two associated tracks with $|d_{xy}| < 1\,\text{mm}$; the other algorithm relaxes the H_T requirement to 350 GeV but additionally requires each of the two jets to have at least one associated track with $|d_{xy}|/\sigma_{d_{xy}} > 5$. The displaced jets are identified using a dedicated tagging algorithm with three

variables that quantify how likely it is that the jet originates from a primary vertex, the significance of the measured transverse displacement of the jet, and the angular difference between the jet momentum direction and the parent particle flight direction. The signal region requires at least two displaced jets, and the background is estimated by measuring the misidentification rate in a control sample with at most one displaced jet. No evidence for a signal is observed, and upper limits are set on the production cross sections for long-lived resonances each decaying to two jets or a lepton and a b quark. In the model with lepton and b quark final states, cross sections above 2.5 fb are excluded for mean proper decay lengths of 70–100 mm, and R-parity violating top squarks with masses below 550–1130 GeV are excluded, depending on the mean proper decay length.

Figure 5.2 compares a selection of the results from the CMS displaced vertex search, the ATLAS displaced vertex search, and the CMS inclusive displaced jets search. While the details of the benchmark signal models used in each analysis are different, in all cases the long-lived particles are pair produced and each decays into a final state with two quarks. This plot shows that searches for displaced jets are probing signal cross sections below 1 fb for a wide range of signal lifetimes.

5.3 Other searches for long-lived particles

Searches for long-lived particles have also been performed in a variety of other final states. These searches probe a wide range of lifetimes, spanning more than 16 orders of magnitude from 100 μm to beyond 10^{12} m. Figure 5.3 shows the range of lifetime exclusions from CMS searches for long-lived particles in pp collisions at $\sqrt{s} = 8$ TeV. The following subsections describe a selection of searches for long-lived particles performed by the CMS and ATLAS Collaborations.

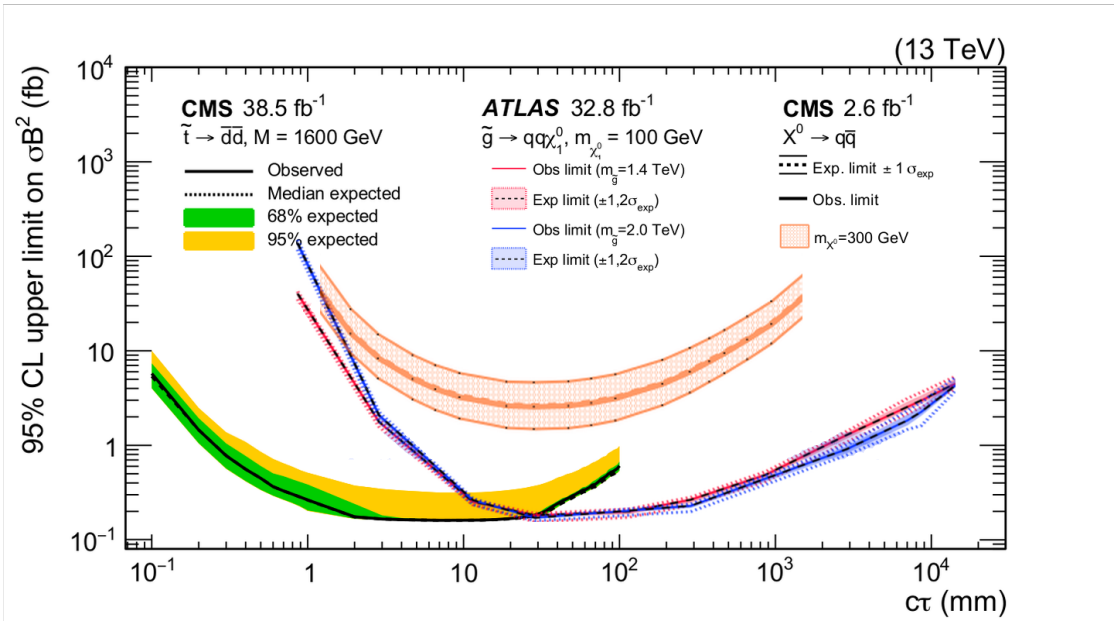

Figure 5.2: Comparison of results from CMS displaced vertex search, ATLAS displaced vertex search, and CMS inclusive displaced jets search. The exclusion curves chosen for comparison use benchmark signal models in which long-lived particles are pair produced and each decays into a final state with two quarks.

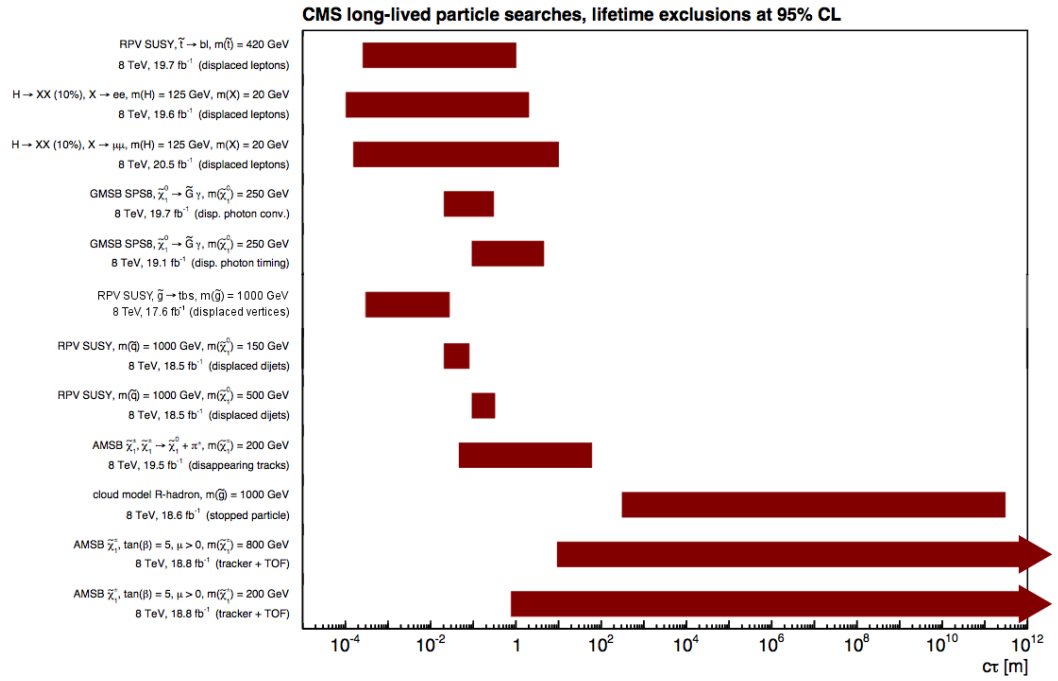

Figure 5.3: Lifetime exclusions from CMS searches for long-lived particles in pp collisions at $\sqrt{s} = 8\,\text{TeV}$.

5.3.1 Displaced jets

The CMS Collaboration searched for long-lived neutral particles decaying to quark-antiquark pairs in pp collisions at $\sqrt{s} = 8\,\text{TeV}$ [18]. The experimental signature is a pair of jets originating from a secondary vertex. The data were collected using a dedicated displaced-jet trigger that required $H_\text{T} > 300\,\text{GeV}$ and at least two jets that have no more than two associated tracks with three-dimensional impact parameter less than $300\,\mu\text{m}$, and no more than 15% of the total jet energy carried by associated tracks with $|d_{xy}| < 500\,\mu\text{m}$. Long-lived particle candidates are formed from all possible pairs of jets, and the set of tracks associated with the jets that have $|d_{xy}| > 500\,\mu\text{m}$ are fitted to a secondary vertex using an adaptive vertex fitter. The secondary vertex is required to have a distance in the transverse plane from the primary vertex that is at least eight times larger than its uncertainty, at least one track from each of the two jets, an invariant mass greater than 4 GeV, the magnitude of the vector sum of the p_T of the tracks greater than 8 GeV, and the average number of missing measurements per track less than 2. In addition, a cluster of at least two of the tracks in the secondary vertex must be reconstructed within 15% of its distance from the primary vertex. The secondary vertex with the highest track multiplicity is selected as the dijet candidate. The signal region is composed of events with a dijet candidate that satisfies three additional selection criteria, and the background yield is predicted by extrapolating from the numbers of events in regions defined by inverting various combinations of the three selection criteria, which were chosen to be independent. No significant excess above standard model expectations is observed. For long-lived neutral particles decaying into quark-antiquark pairs, the upper limits on the production cross section are 0.5–200 fb for mean proper decay lengths of 4–2000 mm. For an RPV model with long-lived neutralinos decaying into a quark-antiquark pair and a muon, the upper

limits are 0.5–3 fb for mean proper decay lengths of 20–400 mm.

The ATLAS Collaboration searched for long-lived particles decaying to jets in the ATLAS hadronic calorimeter in pp collisions at $\sqrt{s} = 8\,\text{TeV}$ [19]. The benchmark signal model is a hidden valley model in which a scalar boson decays to a pair of long-lived particles which each decay to a pair of SM fermions. Each SM fermion pair is reconstructed as a single calorimeter jet with a narrow radius, no tracks from charged particles matched to the jets, and little or no energy deposited in the electromagnetic calorimeter. A dedicated trigger is used to collect events with narrow jets with a high fraction of energy in the hadronic calorimeter and no associated tracks, and events are required to have exactly two jets. The dominant background arises from SM multijet events, and the contribution is estimated from the data by deriving the probability that jets pass the trigger and analysis selection. The probabilities are determined as a function of jet transverse energy and η, and are measured separately for the first jet and the second jet, with a correction applied to account for correlations between the two jets. No significant excess of events over the background estimate is observed. If the scalar boson is the SM Higgs decaying to long-lived particles with a 30% branching fraction, mean proper decay lengths are excluded between 0.10 and 18.50 m.

The ATLAS Collaboration also searched for long-lived particles decaying to jets in the ATLAS inner tracking detector or muon spectrometer in pp collisions at $\sqrt{s} = 8\,\text{TeV}$ [20]. The analysis searches for events with two displaced vertices, each of which is in either the ATLAS inner tracking detector or the ATLAS muon spectrometer. Two triggers are used to select events: the Muon RoI Cluster trigger, which looks for displaced decays in the muon spectrometer, and a jet plus missing transverse energy trigger, which is also sensitive to displaced decays in the inner tracking detector. The analysis also uses two vertex reconstruction algorithms, one

for the inner tracking detector and one for the muon spectrometer. No significant excess of events over the expected background is observed, and limits are placed on several theoretical models with long-lived particles decaying to jets.

5.3.2 Displaced leptons

The CMS Collaboration searched for displaced supersymmetry in events with an electron and a muon with large impact parameters in pp collisions at $\sqrt{s} = 8\,\text{TeV}$ [21]. The electron and muon are required to have opposite charges, and have transverse impact parameter values between 0.2 and 20 mm. In the benchmark signal model, pair-produced top squarks each decay to a bottom quark and a lepton through an R-parity-violating coupling. For a top squark mean proper decay length of 20 mm, the analysis excludes masses below 790 GeV at 95% confidence level.

The CMS Collaboration also searched for long-lived particles that decay into final states containing two electrons or two muons in pp collisions at $\sqrt{s} = 8\,\text{TeV}$ [22]. The experimental signature is a pair of electrons or a pair of muons originating from a displaced secondary vertex. The tracks that are associated with the electrons or muons are required to have a transverse impact parameter significance with respect to the primary vertex of at least 12. The two tracks are fitted to a vertex, and the vertex is required to satisfy a set of selection requirements. The signal region requires that the angle between the direction of the vertex momentum and the direction from the primary vertex to the secondary vertex is less than $\pi/2$, and the background is estimated from a control region with this angle greater than $\pi/2$. No events are found in the signal or control regions in either the electron or muon channel. For an R-parity violating model in which pair-produced squarks each decay to a quark and a long-lived neutralino that subsequently decays to two

leptons and a neutrino, the upper limits on the cross section are in the range 0.2–5 fb for squark masses above 350 GeV and neutralino mean proper decay lengths between 1 and 1000 mm.

5.3.3 Displaced photons

The ATLAS Collaboration searched for nonpointing and delayed photons in the diphoton and missing transverse momentum final state in pp collisions at $\sqrt{s} = 8$ TeV [23]. The benchmark signal model is a gauge-mediated supersymmetry breaking model in which the LSP is the gravitino, and the next-to-lightest supersymmetric particle is a long-lived neutralino which decays into the LSP and a photon. If the SUSY particles are pair-produced, then the final state consists of a pair of photons, and missing transverse energy from the gravitinos. The analysis requires a pair of photons and large missing transverse energy, and searches for non-pointing photons (which do not point back to the primary vertex) and delayed photons (which have late arrival times at the calorimeter). The related variables are measured by the ATLAS electromagnetic calorimeter, which has finely segmented electromagnetic showers that are used the calculate the flight direction of the photons, and time resolution which is used to calculate the time of flight of the photons. No excess over the SM background is observed, and limits are set for long-lived neutralino lifetimes corresponding to mean proper decay lengths between 75 and 30000 mm.

5.3.4 Displaced lepton jets

The ATLAS Collaboration searched for long-lived neutral particles decaying into lepton jets in pp collisions at $\sqrt{s} = 8$ TeV [24]. A lepton jet is a collimated jet of light leptons and hadrons, and can include electron pairs, muon pairs and pion

pairs. The lepton jets are classified according to the final state, which can consist of only muons, muons and jets, or only jets; the muons are measured in the muon spectrometer, while the electrons and pions are measured in the calorimeters. The lepton jets are selected to be distinguished from the SM background and cosmic rays. The data are consistent with the total expected background, and limits are set on models with non-SM Higgs bosons decaying to two long-lived lepton jets with mean proper decay lengths in the range 14–140 mm.

5.3.5 HSCP, disappearing tracks, stopped particles

Searches have also been performed for heavy stable charged particles [46, 47], disappearing tracks [48, 49], and stopped long-lived particles [50, 51].

The searches for heavy stable charged particles (HSCPs) look for particles with speed significantly smaller than the speed of light or charge not equal to the elementary charge. The experimental signatures are a higher rate of energy loss via ionization ($\mathrm{d}E/\mathrm{d}x$) and a longer time of flight. The distribution of $\mathrm{d}E/\mathrm{d}x$ for SM particles is approximately uniform around 3 MeV/cm, while for the HSCP signals it has greater values and is a function of momentum. The data are consistent with the SM background, and upper limits are set on the cross section for a variety of models for physics beyond the SM.

The searches for disappearing tracks look for isolated tracks with missing hits in the outer layers of the silicon tracker, little or no energy in the associated calorimeter deposits, and no associated hits in the muon detectors. These analyses search for long-lived charged particles, but with shorter lifetimes than the searches for HSCPs. The tracks are required to have missing hits in the tracker layers beyond those containing hits on the track, and a small value of energy in the part of the calorimeter near the trajectory of the track. The data are consistent with the

SM background, and for a model of anomaly-mediated supersymmetry breaking with chargino mass of 505 GeV, chargino mean proper decay lengths are excluded between 150 and 18000 mm.

The searches for stopped long-lived particles look for decays of particles that come to rest in the CMS detector. This analysis consists of two separate searches for hadronic decays in the calorimeter and decays into muons in detected in the muon chambers. Dedicated triggers are used to collect proton-proton collision data that is at least two bunch crossings away from any proton bunches, and a control sample of cosmic run data is used to extrapolate instrumental noise. The search is sensitive to lifetimes between 100 ns and 10 days, which is a similar range of lifetimes as the search for HSCPs.

5.4 Searches for prompt RPV SUSY

Many searches for R-parity violating SUSY have been performed at collider experiments. Most of these searches look for products of supersymmetric particle decays via R-parity violating interactions into specific final states. These searches can set experimental constraints on the mass scale of the supersymmetric particle, depending on the allowed decay modes.

The CMS Collaboration searched for prompt RPV SUSY in pp collisions at $\sqrt{s} = 13\,\text{TeV}$ [52]. This search uses the same benchmark signal model that is used for the "multijet signals" for the analysis described in this dissertation, which is the MFV model of RPV SUSY with pair-produced gluinos that each decay into top, bottom, and strange quarks. However, in this search it is assumed that the gluinos decay promptly, and that one of the resulting top quarks decays leptonically while the other decays hadronically. The events are required to have exactly one electron or muon. The analysis searches for an excess of events in distributions of

the number of bottom quark jets, in regions defined by the number of jets and the sum of masses of large-radius jets (M_J). Signal events are expected to have high jet multiplicity due to the final state, and high M_J due to the high-mass gluinos. The data are consistent with the background-only hypothesis, and gluino masses are excluded below 1610 GeV.

The CMS Collaboration also performed a variety of searches for RPV SUSY decaying promptly to multijet final states in pp collisions at $\sqrt{s} = 8$ TeV. These include searches for the multijet MFV model [53], top squarks decaying to two jets [54], gluinos decaying to three jets [55], top squarks decaying to three jets and a lepton [56], and gluinos decaying to five jets [57].

The ATLAS Collaboration searched for RPV SUSY in multijet final states in pp collisions at $\sqrt{s} = 13$ TeV, in events with no requirements on a lepton [58], at least one lepton [59], and two same-sign or three leptons [60]. These analyses use similar kinematic variables to discriminate signal from background as the CMS search for RPV SUSY at 13 TeV: the number of jets, the number of bottom quark jets, and the sum of masses of large-radius jets. The analysis described in Ref. [58] searches in the distribution of the sum of masses of large-radius jets in regions defined by the number of jets and the number of bottom quark jets. For the model in which the gluino directly decays into three quarks, 95% confidence level upper limits are placed on the cross section between 0.80 and 0.011 fb, for gluino masses of 900 and 1800 GeV, respectively. These results are a significant improvement over the similar 8 TeV analysis [61]. The analysis described in Ref. [59] searches in the distribution of the number of bottom quark jets in regions defined by the number of jets. For the model with gluinos decaying into top, bottom, and strange quarks, gluino masses are excluded up to 1650 GeV. The analysis described in Ref. [60] defines signal regions based on the number leptons, the number of bottom quark

jets, the number of jets with p_{T} above a certain threshold, and the effective mass which is the scalar sum of the p_{T} of the leptons, jets, and missing transverse energy. For the RPV models with gluino pair production, gluino masses are excluded below 1300 GeV, which extends the limits from the similar 8 TeV analysis [62].

The ATLAS Collaboration also searched for the pair production of RPV SUSY particles that each decay into two jets in pp collisions at $\sqrt{s} = 13\,\mathrm{TeV}$ [63]. The analysis searches for a peak in the distribution of the average mass of two resonances each reconstructed from two jets. Counting experiments are performed in windows around the average mass, for each of many signal mass hypotheses. The analysis excludes top squark masses between 100 and 410 GeV, which extend the constraints from the similar 8 TeV analysis [64].

CHAPTER 6

CONCLUSION

The field of particle physics is at an exciting stage, with the recent discovery of the Higgs boson, together with cutting-edge technology poised to discover physics beyond the SM. Although many of the most natural theories of physics beyond the SM have since been excluded, more exotic possibilities still remain and have the potential for deeper explanations of the interactions and properties of the fundamental particles. Searches for long-lived particles significantly expand the parameter space of physics beyond the SM probed by the experiments at the LHC.

Many theories for physics beyond the SM predict the pair production of long-lived particles decaying to final states with two or more jets. One example is R-parity violating supersymmetry, which has specific models that predict pair-produced long-lived neutralinos or gluinos decaying into multijet final states, or pair-produced long-lived top squarks decaying into dijet final states. These models are used as benchmark signals for the analysis described in this dissertation, but the search more generally probes any model of new physics that predicts a signature of displaced vertices.

The CMS detector provides precise measurements of the charged-particle trajectories used to reconstruct the displaced vertices produced by long-lived exotic particles. The detector is composed of a silicon pixel and strip tracker, a lead tungstate electromagnetic calorimeter, a brass and scintillator hadron calorimeter, and muon tracking chambers, together with a superconducting solenoid which provides a magnetic field of 3.8 T. This allows for muons, electrons, photons, charged hadrons, and neutral hadrons to be individually identified and precisely reconstructed.

A search for long-lived particles decaying into multijet final states has been

performed using proton-proton collision events collected with the CMS detector at a center-of-mass-energy of 13 TeV in 2015 and 2016. The data sample corresponds to an integrated luminosity of 38.5 fb^{-1}. No excess yield above the prediction from standard model processes is observed. At 95% confidence level, upper limits are placed for models of R-parity violating supersymmetry in which the long-lived particles are neutralinos or gluinos decaying solely into multijet final states or top squarks decaying solely into dijet final states. The data exclude cross sections above approximately 0.3 fb for particles with masses between 800 and 2600 GeV and mean proper decay lengths between 1 and 40 mm. For mean proper decay lengths between 0.6 and 80 mm, gluino masses below 2200 GeV and top squark masses below 1400 GeV are excluded. While the search specifically addresses two models of R-parity violating supersymmetry, the results are relevant to other models in which long-lived particles decay to final states with multiple tracks, and a method to extend the search to other signal models is provided. For the models considered, the results provide the most restrictive bounds to date on the production and decay of pairs of long-lived particles with mean proper decay lengths between 0.1 and 100 mm.

The analysis presented in this dissertation is sensitive to particles with intermediate lifetimes. Other searches such as the ATLAS displaced vertex search and the CMS inclusive displaced jets search probe similar models of new physics but are more sensitive to signals with longer lifetimes. Searches for new physics such as long-lived particles decaying to other final states and RPV SUSY decaying promptly to multijet final states probe complementary regions of parameter space. Searches for long-lived particles are probing cross sections below 1 fb for a wide range of signal lifetimes, and are an important and exciting new direction at the LHC.

BIBLIOGRAPHY

[1] Particle Data Group, C. Patrignani, *et al.*, "Review of particle physics," *Chin. Phys. C*, vol. 40, p. 100001, 2016.

[2] CMS Collaboration, "CMS luminosity measurement for the 2015 data-taking period," CMS Physics Analysis Summary CMS-PAS-LUM-15-001, 2017.

[3] CMS Collaboration, "CMS luminosity measurements for the 2016 data-taking period," CMS Physics Analysis Summary CMS-PAS-LUM-17-001, 2017.

[4] C. Csáki, Y. Grossman, and B. Heidenreich, "Minimal flavor violation supersymmetry: a natural theory for R-parity violation," *Phys. Rev. D*, vol. 85, p. 095009, 2012.

[5] C. Csáki, E. Kuflik, S. Lombardo, O. Slone, and T. Volansky, "Phenomenology of a long-lived LSP with R-parity violation," *JHEP*, vol. 08, p. 016, 2015.

[6] J. L. Hewett, B. Lillie, M. Masip, and T. G. Rizzo, "Signatures of long-lived gluinos in split supersymmetry," *JHEP*, vol. 09, p. 070, 2004.

[7] M. J. Strassler and K. M. Zurek, "Echoes of a hidden valley at hadron colliders," *Phys. Lett. B*, vol. 651, p. 374, 2007.

[8] R. Barbier, C. Bérat, M. Besançon, M. Chemtob, A. Deandrea, E. Dudas, P. Fayet, S. Lavignac, G. Moreau, E. Perez, and Y. Sirois, "R-parity violating supersymmetry," *Phys. Rept.*, vol. 420, p. 1, 2005.

[9] CMS Collaboration, "Description and performance of track and primary-vertex reconstruction with the CMS tracker," *JINST*, vol. 9, p. P10009, 2014.

[10] CMS Collaboration, "Particle-flow reconstruction and global event description with the CMS detector," *JINST*, vol. 12, p. P10003, 2017.

[11] ATLAS Collaboration, "Search for long-lived, massive particles in events with displaced vertices and missing transverse momentum in $\sqrt{s} = 13\,\text{TeV}$ pp collisions with the ATLAS detector," *Phys. Rev. D*, vol. 97, p. 052012, 2018.

[12] H. P. Nilles, "Supersymmetry, supergravity and particle physics," *Phys. Rept.*, vol. 110, p. 1, 1984.

[13] H. E. Haber and G. L. Kane, "The search for supersymmetry: probing physics beyond the standard model," *Phys. Rept.*, vol. 117, p. 75, 1985.

[14] Y. Cui and B. Shuve, "Probing baryogenesis with displaced vertices at the LHC," *JHEP*, vol. 02, p. 049, 2015.

[15] CMS Collaboration, "Identification of b-quark jets with the CMS experiment," *JINST*, vol. 8, p. P04013, 2013.

[16] CMS Collaboration, "Search for R-parity violating supersymmetry with displaced vertices in proton-proton collisions at $\sqrt{s} = 8\,\text{TeV}$," *Phys. Rev. D*, vol. 95, p. 012009, 2017.

[17] CMS Collaboration, "Search for new long-lived particles at $\sqrt{s} = 13\,\text{TeV}$," *Phys. Lett. B*, vol. 780, p. 432, 2018.

[18] CMS Collaboration, "Search for long-lived neutral particles decaying to quark-antiquark pairs in proton-proton collisions at $\sqrt{s} = 8\,\text{TeV}$," *Phys. Rev. D*, vol. 91, p. 012007, 2015.

[19] ATLAS Collaboration, "Search for pair-produced long-lived neutral particles decaying in the ATLAS hadronic calorimeter in pp collisions at $\sqrt{s} = 8\,\text{TeV}$," *Phys. Lett. B*, vol. 743, p. 15, 2015.

[20] ATLAS Collaboration, "Search for long-lived, weakly interacting particles that decay to displaced hadronic jets in proton-proton collisions at $\sqrt{s} = 8\,\text{TeV}$ with the ATLAS detector," *Phys. Rev. D*, vol. 92, p. 012010, 2015.

[21] CMS Collaboration, "Search for displaced supersymmetry in events with an electron and a muon with large impact parameters," *Phys. Rev. Lett.*, vol. 114, p. 061801, 2015.

[22] CMS Collaboration, "Search for long-lived particles that decay into final states containing two electrons or two muons in proton-proton collisions at $\sqrt{s} = 8\,\text{TeV}$," *Phys. Rev. D*, vol. 91, p. 052012, 2015.

[23] ATLAS Collaboration, "Search for nonpointing and delayed photons in the diphoton and missing transverse momentum final state in 8 TeV pp collisions at the LHC using the ATLAS detector," *Phys. Rev. D*, vol. 90, p. 112005, 2014.

[24] ATLAS Collaboration, "Search for long-lived neutral particles decaying into lepton jets in proton-proton collisions at $\sqrt{s} = 8\,\text{TeV}$ with the ATLAS detector," *JHEP*, vol. 11, p. 088, 2014.

[25] S. P. Martin, "A supersymmetry primer," *Adv. Ser. Direct. High Energy Phys.*, vol. 18, p. 1, 1998.

[26] G. R. Farrar and P. Fayet, "Phenomenology of the production, decay, and detection of new hadronic states associated with supersymmetry," *Phys. Lett. B*, vol. 76, p. 575, 1978.

[27] S. Weinberg, "Supersymmetry at ordinary energies. masses and conservation laws," *Phys. Rev. D*, vol. 26, p. 287, 1982.

[28] E. Nikolidakis and C. Smith, "Minimal flavor violation, seesaw mechanism, and R-parity," *Phys. Rev. D*, vol. 77, p. 015021, 2008.

[29] CMS Collaboration, "The CMS experiment at the CERN LHC," *JINST*, vol. 3, p. S08004, 2008.

[30] CMS Collaboration, "The CMS trigger system," *JINST*, vol. 12, p. P01020, 2017.

[31] M. Cacciari, G. P. Salam, and G. Soyez, "The anti-k_t jet clustering algorithm," *JHEP*, vol. 04, p. 063, 2008.

[32] M. Cacciari, G. P. Salam, and G. Soyez, "FastJet user manual," *Eur. Phys. J. C*, vol. 72, p. 1896, 2012.

[33] CMS Collaboration, "Jet energy scale and resolution in the CMS experiment in pp collisions at 8 TeV," *JINST*, vol. 12, p. P02014, 2017.

[34] T. Sjöstrand, S. Ask, J. R. Christiansen, R. Corke, N. Desai, P. Ilten, S. Mrenna, S. Prestel, C. O. Rasmussen, and P. Z. Skands, "An introduction to PYTHIA 8.2," *Comput. Phys. Commun.*, vol. 191, p. 159, 2015.

[35] R. D. Ball, V. Bertone, S. Carrazza, L. Del Debbio, S. Forte, A. Guffanti, N. P. Hartland, and J. Rojo, "Parton distributions with QED corrections," *Nucl. Phys. B*, vol. 877, p. 290, 2013.

[36] J. Alwall, R. Frederix, S. Frixione, V. Hirschi, F. Maltoni, O. Mattelaer, H.-S. Shao, T. Stelzer, P. Torrielli, and M. Zaro, "The automated computation of tree-level and next-to-leading order differential cross sections, and their matching to parton shower simulations," *JHEP*, vol. 07, p. 079, 2014.

[37] R. D. Ball *et al.*, "Parton distributions for the LHC Run II," *JHEP*, vol. 04, p. 040, 2015.

[38] CMS Collaboration, "Event generator tunes obtained from underlying event and multiparton scattering measurements," *Eur. Phys. J. C*, vol. 76, p. 155, 2016.

[39] CMS Collaboration, "Investigations of the impact of the parton shower tuning in Pythia 8 in the modelling of $\mathrm{t\bar{t}}$ at $\sqrt{s} = 8$ and 13 TeV," CMS Physics Analysis Summary CMS-PAS-TOP-16-021, 2016.

[40] S. Agostinelli *et al.*, "GEANT4—a simulation toolkit," *Nucl. Instrum. Meth. A*, vol. 506, p. 250, 2003.

[41] R. Frühwirth, "Application of Kalman filtering to track and vertex fitting," *Nucl. Instrum. Meth. A*, vol. 262, p. 444, 1987.

[42] R. J. Barlow, "Extended maximum likelihood," *Nucl. Instrum. Meth. A*, vol. 297, p. 496, 1990.

[43] G. Cowan, "Statistics", Ch. 39 in Particle Data Group, C. Patrignani, *et al.*, "Review of particle physics," *Chin. Phys. C*, vol. 40, p. 100001, 2016.

[44] C. Borschensky, M. Krämer, A. Kulesza, M. Mangano, S. Padhi, T. Plehn, and X. Portell, "Squark and gluino production cross sections in pp collisions at $\sqrt{s} = 13$, 14, 33 and 100 TeV," *Eur. Phys. J. C*, vol. 74, p. 3174, 2014.

[45] ATLAS Collaboration, "Search for massive, long-lived particles using multi-track displaced vertices or displaced lepton pairs in pp collisions at $\sqrt{s} = 8$ TeV with the ATLAS detector," *Phys. Rev. D*, vol. 92, p. 072004, 2015.

[46] CMS Collaboration, "Search for long-lived charged particles in proton-proton collisions at $\sqrt{s} = 13$ TeV," *Phys. Rev. D*, vol. 94, p. 112004, 2016.

[47] CMS Collaboration, "Searches for long-lived charged particles in pp collisions at $\sqrt{s} = 7$ and 8 TeV," *JHEP*, vol. 07, p. 122, 2013.

[48] CMS Collaboration, "Search for disappearing tracks as a signature of new long-lived particles in proton-proton collisions at $\sqrt{s} = 13$ TeV," 2018.

[49] CMS Collaboration, "Search for disappearing tracks in proton-proton collisions at $\sqrt{s} = 8$ TeV," *JHEP*, vol. 01, p. 096, 2015.

[50] CMS Collaboration, "Search for decays of stopped exotic long-lived particles produced in proton-proton collisions at $\sqrt{s} = 13\,\text{TeV}$," *JHEP*, vol. 05, p. 127, 2018.

[51] CMS Collaboration, "Search for decays of stopped long-lived particles produced in proton-proton collisions at $\sqrt{s} = 8\,\text{TeV}$," *Eur. Phys. J. C*, vol. 75, p. 151, 2015.

[52] CMS Collaboration, "Search for R-parity violating supersymmetry in pp collisions at $\sqrt{s} = 13\,\text{TeV}$ using b jets in a final state with a single lepton, many jets, and high sum of large-radius jet masses," *Phys. Lett. B*, vol. 783, p. 114, 2018.

[53] CMS Collaboration, "Searches for R-parity violating supersymmetry in pp collisions at $\sqrt{s} = 8\,\text{TeV}$ in final states with 0–4 leptons," *Phys. Rev. D*, vol. 94, p. 112009, 2016.

[54] CMS Collaboration, "Search for pair-produced resonances decaying to jet pairs in proton-proton collisions at $\sqrt{s} = 8\,\text{TeV}$," *Phys. Lett. B*, vol. 747, p. 98, 2015.

[55] CMS Collaboration, "Searches for light- and heavy-flavour three-jet resonances in pp collisions at $\sqrt{s} = 8\,\text{TeV}$," *Phys. Lett. B*, vol. 730, p. 193, 2014.

[56] CMS Collaboration, "Search for R-parity violating decays of a top squark in proton-proton collisions at $\sqrt{s} = 8\,\text{TeV}$," *Phys. Lett. B*, vol. 760, p. 178, 2016.

[57] CMS Collaboration, "Search for new phenomena in events with high jet multiplicity and low missing transverse momentum in proton-proton collisions at $\sqrt{s} = 8\,\text{TeV}$," *Phys. Lett. B*, vol. 770, p. 257, 2017.

[58] ATLAS Collaboration, "Search for R-parity-violating supersymmetric particles in multi-jet final states produced in pp collisions at $\sqrt{s} = 13\,\text{TeV}$ using the ATLAS detector at the LHC," 2018.

[59] ATLAS Collaboration, "Search for new phenomena in a lepton plus high jet multiplicity final state with the ATLAS experiment using $\sqrt{s} = 13\,\text{TeV}$ proton-proton collision data," *JHEP*, vol. 09, p. 088, 2017.

[60] ATLAS Collaboration, "Search for supersymmetry in final states with two same-sign or three leptons and jets using 36 fb^{-1} of $\sqrt{s} = 13\,\text{TeV}$ pp collision data with the ATLAS detector," *JHEP*, vol. 09, p. 084, 2017.

[61] ATLAS Collaboration, "Search for massive supersymmetric particles decaying to many jets using the ATLAS detector in pp collisions at $\sqrt{s} = 8\,\text{TeV}$," *Phys. Rev. D*, vol. 91, p. 112016, 2015.

[62] ATLAS Collaboration, "Search for supersymmetry at $\sqrt{s} = 8\,\text{TeV}$ in final states with jets and two same-sign leptons or three leptons with the ATLAS detector," *JHEP*, vol. 06, p. 035, 2014.

[63] ATLAS Collaboration, "A search for pair-produced resonances in four-jet final states at $\sqrt{s} = 13\,\text{TeV}$ with the ATLAS detector," *Eur. Phys. J. C*, vol. 78, p. 250, 2018.

[64] ATLAS Collaboration, "A search for top squarks with R-parity violating decays to all-hadronic final states with the ATLAS detector in $\sqrt{s} = 8\,\text{TeV}$ proton-proton collisions," *JHEP*, vol. 06, p. 067, 2016.